THE UNIVERSITY OF MICHIGAN
COLLEGE OF ENGINEERING
Department of Nuclear Engineering

Technical Report

MEASUREMENT OF THE PHONON FREQUENCY DISTRIBUTION FOR POLYETHYLENE BY NEUTRON SCATTERING

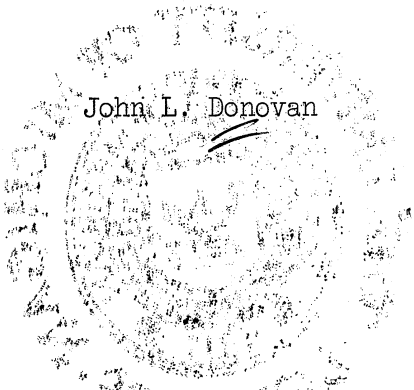

John L. Donovan

ORA Project 05783

supported by:

NATIONAL SCIENCE FOUNDATION
GRANT NO. GP-1032
WASHINGTON, D. C.

administered through:

OFFICE OF RESEARCH ADMINISTRATION ANN ARBOR

November 1964

This report was also a dissertation submitted in partial fulfillment of the requirements for the degree of Doctor of Philosophy in The University of Michigan, 1964.

ABSTRACT

Neutron inelastic scattering experiments have been used to investigate low frequency (0-800 cm^{-1}) vibrational motions in highly crystalline polyethylene. "Warm" neutrons (0.025-0.15 ev) have been downscattered from polyethylene targets at 298, 125, and 90°K. Phonon excitation corresponding to neutron energy loss is determined. The experiments were undertaken to verify and extend the "cold" neutron (0.005 ev) inelastic scattering experiments of Danner, Safford, Boutin, and Berger (1) using a different scattering technique, and to demonstrate that a triple axis crystal spectrometer can be used successfully with a "warm" neutron source for incoherent, inelastic scattering experiments.

The measured inelastic cross section data have been analyzed using the one phonon incoherent approximation to determine the phonon frequency distribution. The corrections to the observed data necessary to obtain the cross section are discussed. The design features of the spectrometer which provide sufficient intensity for inelastic scattering experiments with a two megawatt reactor source are presented. These features include the use of a large size beam (4.7 inches by 5 inches at the target), vertical focusing of the beam, multiple analyzer systems at a 90° scattering angle, and use of three inch diameter BF_3 detectors. The best compromise between spectrometer resolution and intensity is shown to depend on a good match between collimator and crystal characteristics.

The four low frequencies seen in the previous neutron experiments at 100°K (60, 130, 190, and 340 cm^{-1}), are confirmed but some additional frequencies were observed as shown in Table 1. These frequency values are compared with models (18,33) that attempt to account for intermolecular effects in the crystalline molecular structure. These results are shown in Table 2, together with a far infrared measurement (6). The temperature dependence of the calculated frequency values is not well known.

TABLE 1

FREQUENCIES OBSERVED IN MARLEX 6050 POLYETHYLENE AT 90, 125, AND 298°K (E_f=0.027 ev)

Temp., °K	Frequency, cm^{-1}										
298	--	60	95	140	---	190	240	280	---	370	500
125	45	65	95	135	165	190	---	280	---	390	490-540
90	--	65	90	137	165	192	---	270	330	390	500-540

TABLE 2

MEASURED AND CALCULATED LOW FREQUENCIES (CM^{-1}) FOR POLYETHYLENE

"Warm" Neutron Results, 90°K	Tasumi (18) Calculations, 290°K	Miyazawa (33) Calculations, 290°K	Infrared (6) Measurement, 300°K
45	--	--	--
65	57	--	--
90	74	80	72.5
--	104	100	--
137	133	--	--
165	169	--	--

Frequency spectra at 90° are reported for two target thicknesses (29.5 and 16.1 mils). The spectra indicate that multiple scattering effects are small. Good agreement between these spectra and the "cold" neutron spectrum at 100°K is found for the frequency range below 200 cm^{-1}. Above 330 cm^{-1} the agreement is poor; both sets of experiments are less reliable above about 450 cm^{-1} because of poorer intensity and resolution, and in the case of the "warm" experiments,the proximity of the second order peak. Both the "cold" and "warm" spectra show much larger amplitude in the frequency region 250-450 cm^{-1} than the spectrum calculated by Wunderlich (8) using specific heat data. The effect of multiphonon interference on the measured scattering data apparently does not produce a major difference between the "cold" and "warm" neutron techniques for low temperature polyethylene. Hence, it is concluded that with proper choice of targets and target temperature, this interference need not be a fundamental drawback of the method. An important intensity advantage occurs with low temperature targets which makes the "warm" neutron downscatter method attractive.

ACKNOWLEDGMENTS

The author is indebted to Professor John S. King, chairman of the doctoral committee, for continuous helpful guidance during this investigation. The valuable advice of other committee members is also gratefully acknowledged. Special mention should be made of the assistance provided by Dr. George Summerfield, who, through his intense interest in the problem, provided theoretical discussions and calculations on the interpretation of the experimental results.

Valuable aid has also been provided by other members of the triple axis crystal spectrometer group: Mr. William Myers, Mr. Edward Straker and Mr. Kent Carpenter. The work of Mr. Myers in developing the electronics for the spectrometer was especially important.

Use of the facilities of The University of Michigan Computing Center is hereby acknowledged. The computer programs used were compiled by Mr. Jon Erickson, whose interest and assistance is appreciated. The theoretical work undertaken by Mr. Erickson on the Debye-Waller factor for polyethylene, and on the frequency distribution based on the two phonon cross section, served to provide valuable assistance in the interpretation of the experimental data.

The financial support provided by a Fellowship from the Atomic Energy Commission during the years 1959-1962 made

graduate study possible. An Owens-Corning Fiberglas Phoenix Fellowship, 1962-1964, provided support while this research was completed. To the Phoenix Project and its acting director, Professor William Kerr, I am very thankful.

Funds for the construction and use of the triple axis spectrometer were provided by a grant from the National Science Foundation. This contract also provided funds for a part-time salary; this financial aid is also appreciated.

The aid provided by the staff of The University of Michigan Ford Nuclear Reactor was helpful in many ways. The contribution of Mr. James Miller, Shift Supervisor, was especially important.

Much of the experimental equipment was made in the Instrument Shop of the Phoenix Memorial Laboratory. The help of Mr. Robert White, Mr. Mike Nickolas, and especially Mr. Iwan Pacholok is recognized as an important contribution to the success of this work.

It is difficult to acknowledge properly the help of the two people most responsible for constant inspiration and encouragement. Dr. John King, my chairman, provided continuous interest, suggestions, guidance and thoughtful attention; my wife, Eunice, graciously carried a heavier burden while enriching our family life. For her inspiration, sacrifices, and invaluable encouragement I am humbly grateful.

TABLE OF CONTENTS

LIST OF TABLES

LIST OF FIGURES

Figure Page

CHAPTER I

INTRODUCTION

Statement of the problem

The polyethylene molecule has been the subject of very extensive scientific investigation because of its commercial importance and, relative to other high polymers, its simple structure. The molecule is composed of CH_2 groups arranged in a long planar zig-zag chain:

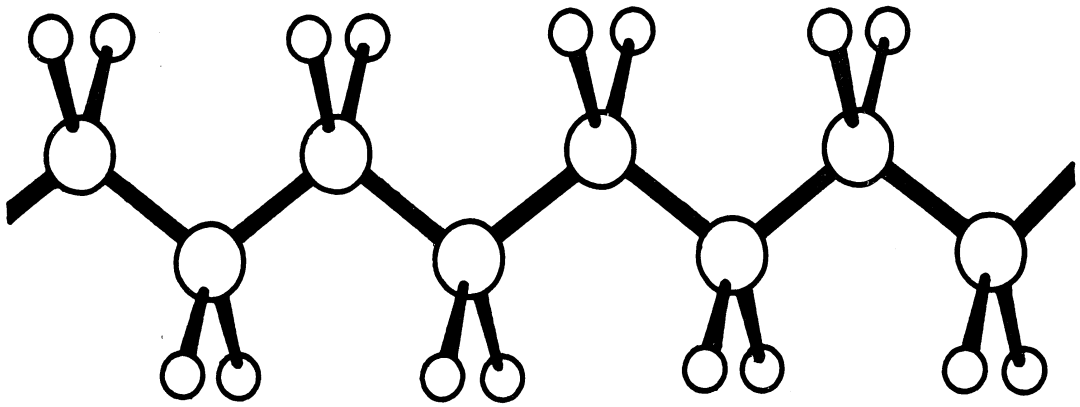

Figure 1. Polyethylene molecule.

The chains may or may not be oriented in a three dimensional lattice and are not always infinitely long. To understand the molecular structure and its motion, many theoretical analyses and experimental measurements have been made to determine the

vibrational frequencies of the molecule. Infrared and Raman spectroscopy, nuclear magnetic resonance, specific heat and neutron inelastic scattering are experimental techniques which have been used. The molecular motions have been investigated theoretically by treating the molecule both as an extended single chain and in a three dimensional crystalline structure.

The optical vibrational frequencies have been well identified, particularly by infrared measurements. However, little electromagnetic data exists for the low frequency region (0 - 700 cm^{-1}). This frequency region is of prime importance for an understanding of the specific heat properties of polyethylene, and for determining the Debye-Waller factor for this material. The theory for the extended single chain model predicts that only two acoustic normal modes of vibration exist in this frequency region. The lower frequency mode, with a limit near 200 cm^{-1}, corresponds to a skeletal torsional vibration of the polyethylene chain; the other mode, with a limit near 500 cm^{-1}, is a combination of the skeletal stretching and bending normal modes. The single chain model leads to the prediction that these two acoustic modes are optically inactive because of zero frequency intercepts for phase differences of 0° or 180° (the phase difference is between adjacent elements of the chain). However, in the crystalline model, the frequency-phase difference curves (dispersion curves) are split and shifted, so that some non-zero intercepts result. Consequently

the modes may then be optically active, and observation by electro-magnetic interaction is possible.

Neutron inelastic scattering is not limited by selection rules or symmetry considerations; this type of measurement may also offer an intensity advantage. An interaction between a neutron and a polyethylene molecule is primarily with one of the hydrogen atoms because of the large incoherent cross section of hydrogen. Consequently the inelastic scattering measurements will contain information about all the molecular motions in which the hydrogen atoms participate. Neutron inelastic scattering experiments are relatively new; the results are not as definitive as infrared measurements. However, when infrared results are not available because of selection rules, neutron inelastic scattering can be used to provide information on the optically inactive molecular vibrations.

The energy distribution of inelastically scattered "cold" neutrons (0.005 ev) scattered from polyethylene has been measured by Danner, Safford, Boutin and Berger (1) to study the phonon frequency region 30 - 800 cm^{-1}. The molecular motions in highly crystalline polyethylene were investigated as a function of temperature. In these experiments it is the energy gained by the low energy "cold" neutrons by phonon absorption that is measured.

This thesis reports further results of neutron inelastic scattering experiments on highly crystalline polyethylene as a function of temperature. "Warm" neutrons, 0.027 to 0.12 ev are

down-scattered from the target and the energy loss corresponding to phonon excitation is determined. This experiment was undertaken for three primary reasons: first, to verify and extend the results of Danner et. al (1) by use of a different scattering technique; second, to determine the importance of multi-phonon events in neutron scattering on polyethylene at low temperature; third, to demonstrate that a triple axis crystal spectrometer can be used successfully for incoherent, inelastic scattering with a "warm" neutron source. A particular advantage of this experimental technique is the increase in scattering intensity for down-scatter experiments (neutron energy loss) as compared to up-scatter experiments (neutron energy gain) for targets at low temperature. This investigation of the low frequency motions in polyethylene is the first attempt to use a triple axis crystal spectrometer to measure incoherent, inelastic scattering.

Previous experimental work

Infrared absorption and Raman scattering

An infrared spectrum of oriented polyethylene has been reported by Krimm (2). The spectrum extends from 3200 cm^{-1} to 100 cm^{-1}. The specimen studied was of moderate crystallinity and had a fairly high CH_3 group content. The band positions of the vibrational spectrum below 1000 cm^{-1} are shown in Table 1. This table reveals that in the frequency region below the very

strong absorption band at 720 cm^{-1}, the observed bands have only weak or very weak intensities. It is nevertheless significant that the weak bands at 540-560 cm^{-1} and 200 cm^{-1}, are near the acoustic limits predicted by a linear chain theory. (No assignment was made for the very very weak band observed near 430 cm^{-1}, or the weak band near 600 cm^{-1}.) The strong band at 720 cm^{-1} is the lowest frequency optical mode.

TABLE 1

MEASURED INFRARED VIBRATIONAL SPECTRUM OF POLYETHYLENE (2)

Frequency, cm^{-1}	Relative Intensity
200	VW
430	VVW
540-560	W
573	W
600	W
720	VS
731	VS
888	VW
890	VVW
908	M
964	VVW
990	W

V = very,
S = strong,
W = weak,
M = medium

Another infrared spectrum measurement has been reported by Nielsen and Holland (4). The polyethylene studied was Marlex

6050, a high crystallinity polyethylene. The observed bands in the frequency region 0 - 800 cm^{-1} are shown in Table 2, together with intensity descriptions. Only very, very, very weak bands were reported below the very strong band at 720 cm^{-1}. No frequencies were reported below 539 cm^{-1}.

TABLE 2

MEASURED INFRARED SPECTRUM OF SOLID MARLEX 6050 POLYETHYLENE (4)

Frequency, cm^{-1}	Relative Intensity
539	VVVW
550	VVVW
573	VVVW
617	VVVW
622	VVVW
720	VS
731	VS

V = very,
S = strong,
W = weak

Nielsen and Woollett (3) reported Raman scattering measurements on polyethylene. The lowest frequency identified in their spectra was at 720 cm^{-1}. Spectra were obtained on polyethylene samples ranging in crystallinity from 50% to 95% (Marlex 50). Because no distinguishable bands were seen below the absorption band at 720 cm^{-1}, the authors suggested Marlex 50 as a window material for Raman experiments in the low frequency region.

Very little electromagnetic experimental work has been reported which is directed specifically at the acoustic frequency region. However, two recent far infrared measurements have been reported. Willis, Miller, Adams and Gebbie (5) investigated the frequency region between 40 cm^{-1} and 450 cm^{-1}. Spectra of thick (1/4 or 1/2 inch) layers of many synthetic polymers were observed in a search for a suitable spectrometer window material for use in the far infrared. Four samples of commercial polyethylene were observed; three were of high density (high crystallinity). The results are shown in Figure 2. The spectra of the three high density samples show a sharp absorption band near 75 cm^{-1}; this band is much weaker in the low density spectrum. A much weaker absorption band appears near 140 cm^{-1} for all four samples. Bands at 190 cm^{-1} and 280 cm^{-1} show clearly in two of the three high density samples and the low density material. The authors point out that the observed bands might not be due to the base polymer, but to additives used in the commercial preparation of the polyethylene. There is a band observed at 380 cm^{-1} which the authors believe is due to the beam splitter in the interferometer, constructed from polyethylene terephthalate film, which has an absorption band at 380 cm^{-1}. From Figure 2, the authors conclude that polyethylenes prepared with the use of Ziegler type catalysts are not suitable for infrared windows because of the relatively strong absorption bands (see curves 3 and 4 in Figure 2). The

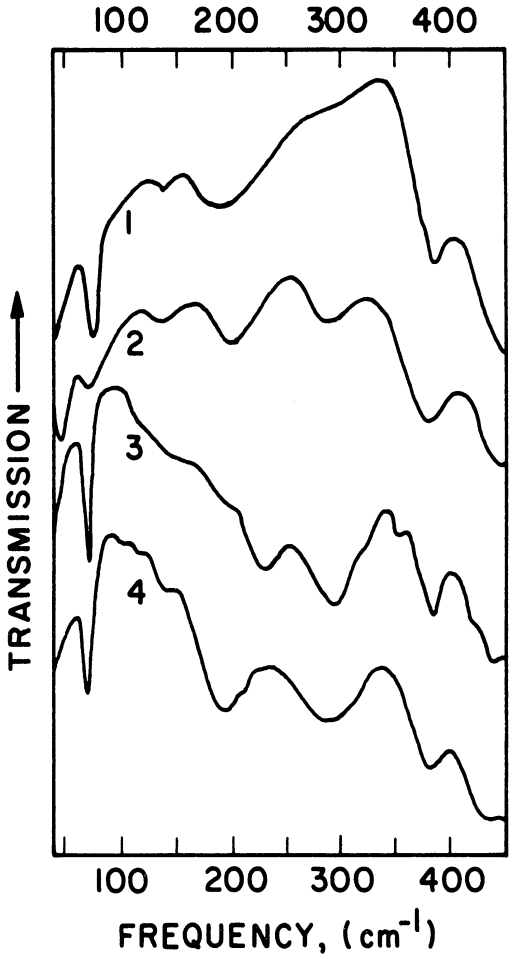

Figure 2. Infrared spectra of commercial polyethylene. (1) "Rigidex 35" (high density) 1/2 inch thickness. (2) "Alkathene XRM 40" (low density) 1/2 inch thickness. (3) "Hostalen GF 5740" (high density) 1/4 inch thickness. (4) "Shell Carlona 200" (high density) 1/4 inch thickness. (5)

third high density polyethylene, Rigidex (curve 1 in Figure 2), is made by a high pressure process. It was the most transparent material found.

Bertie and Whalley (6) examined polyethylene in the far infrared also, using a 2.5 mm thick sample of high density at 100°, 190° and 300°K. The spectra show a sharp band near 75 cm^{-1} whose maximum intensity increases as the temperature is lowered, and whose frequency changes from 72.5 cm^{-1} at 300°K to 79 cm^{-1} at 100°K. This band was more intense in high density (high crystallinity) samples. It has been suggested that the change in the frequency as a function of temperature may be explained simply by the change in force constants due to volume changes (7).

Neutron inelastic scattering

The vibrational spectrum of polyethylene was examined by Danner, Safford, Boutin and Berger (1) using the "cold" (E_o = 0.005 ev) neutron technique. The time-of-flight distribution was measured for neutrons scattered at 90° from highly crystalline (85%) polyethylene. Polyethylene temperatures of 468°, 428°, 412°, 293° and 100°K were studied. For these measurements, target plates 6" x 6" x 0.032" were prepared from Phillips Marlex 6050 pellets.

The time-of-flight distribution for neutrons scattered at 90° from a 293°K target is shown as Figure 3a. The corrected number of counts per channel is plotted as a function

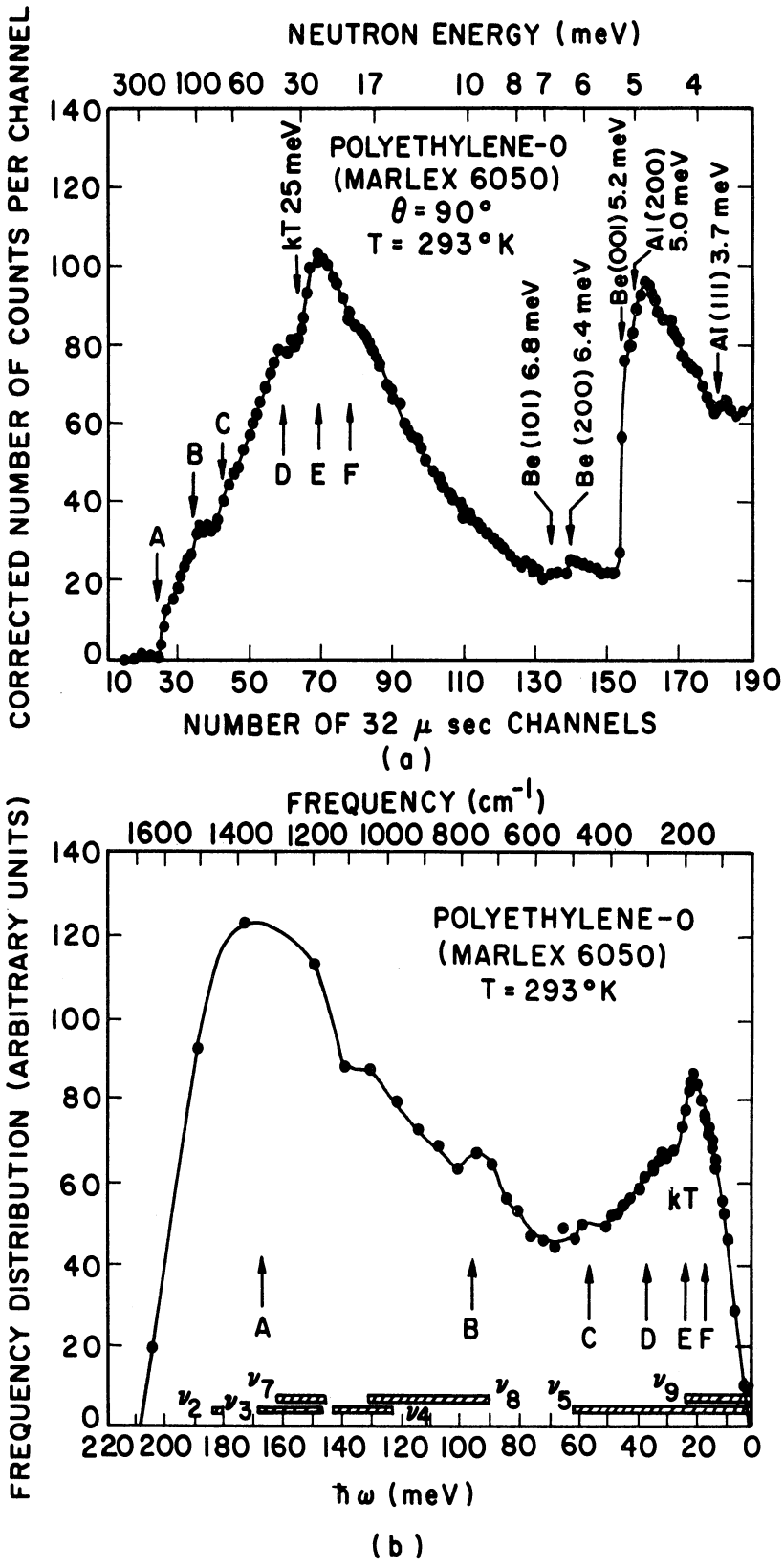

Figure 3. (a) Time-of-flight distribution of neutrons scattered at 90° from a sample of Marlex 6050 at 293°K. (b) Frequency distribution derived from the data in (a) in the one-phonon approximation. (1)

of the channel number. The corresponding energy scale is shown also. The frequency distribution obtained using the one phonon incoherent approximation (Equation II-11) is shown in Figure 3b. The horizontal hatched bars in Figure 3b represent the frequency regions spanned by the dispersion curves calculated by Tasumi, Shimanouchi and Miyazawa (9). The inelastic distribution (above 5.2 mev in Figure 3a) was interpreted to be the superposition of a number of components: a pronounced peak (E) near 170 cm^{-1}, a partially resolved peak (B) at 720 cm^{-1}, a slight rise (C) between 450 and 550 cm^{-1}, a broad component (D) between 230 and 400 cm^{-1}, and a slight shoulder (F) near 90 cm^{-1}.

However, when the polyethylene temperature was lowered from 293°K to 100°K some of these components became sharper. The 100°K scattering data is shown in Figure 4a; the frequency distribution is shown in Figure 4b. The component E remained near 190 cm^{-1}, but D and F change shape and are seen to peak near 340 and 130 cm^{-1} respectively. Component C is shifted and becomes dramatically more pronounced, peaking near 570 cm^{-1}. A weak component (G) is also suggested near 60 cm^{-1}. Clearly an important result of the "cold" neutron experiments is the evidence of a marked temperature dependence of the phonon frequency spectrum; this is evident from a comparison of Figure 3b and 4b.

A second paper, reporting on the results of "cold" neutron experiments with room temperature polyethylene has been published by Zemlyanov and Chernoplekov (10). Results are shown

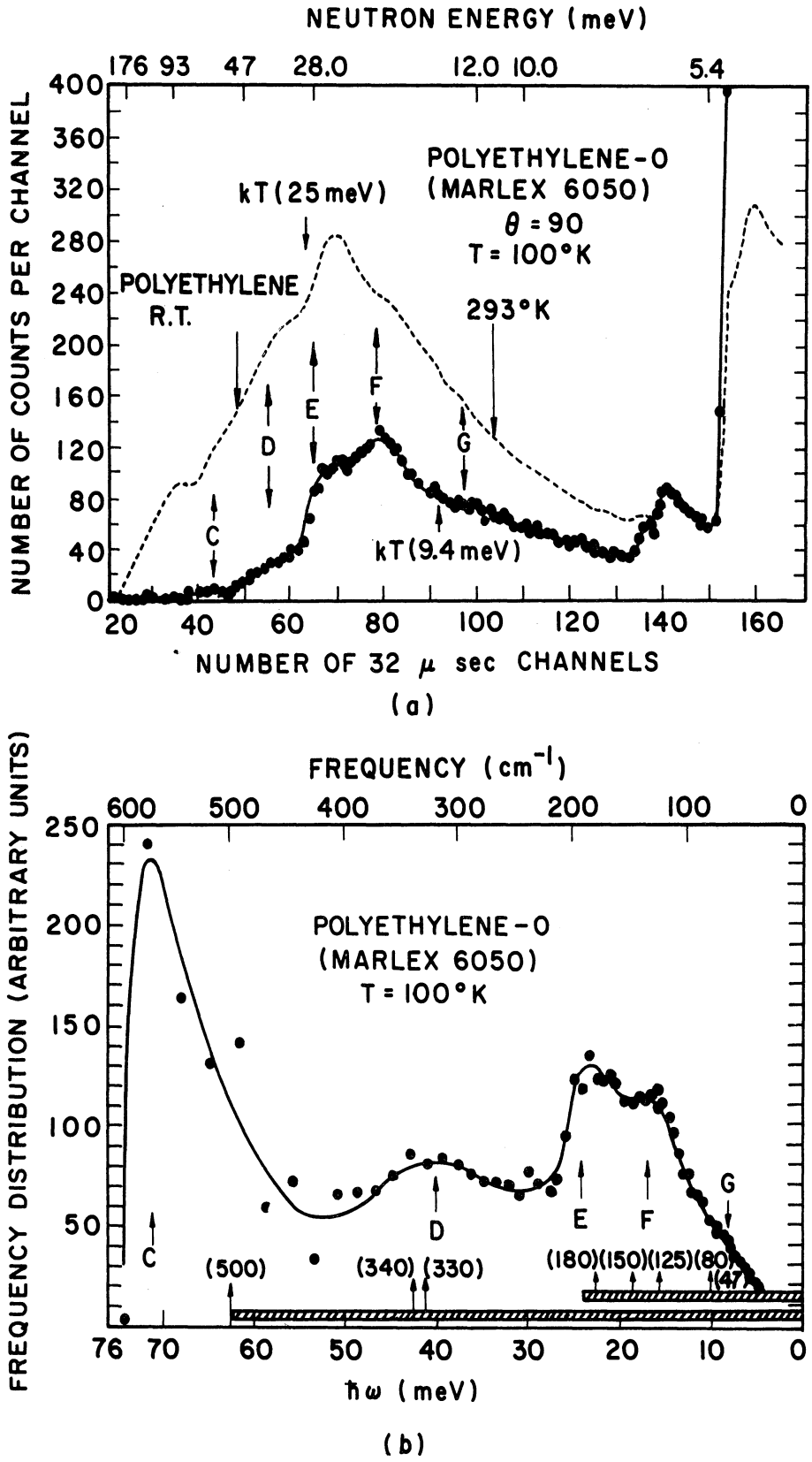

Figure 4. (a) Time-of-flight distribution of neutrons scattered at 90° from a sample of Marlex 6050 at 100°K. (b) Frequency distribution derived from the data in (a) in the one-phonon approximation. (1)

for scattering from both non-irradiated and irradiated polyethylene. The irradiated material was exposed to 500 megarads; this was estimated to produce about 10% joining between the polymer chains. The results are shown as Figures 5 and 6. The scattering to high energies, Figure 5, showed evidence of many of the frequencies observed by infrared and Raman experiments. No noticeable difference was seen between the results for the irradiated and non-irradiated polyethylene. In the results for lower energy transfers, Figure 6, a small difference apparently resulted. The scattering data suggested energy transfers at 118 cm^{-1}, 167 cm^{-1} and 247 cm^{-1}. Two other transfers, at 94 cm^{-1} and 33 cm^{-1}, were seen more strongly in the spectrum of the non-irradiated polyethylene; however, the spectra were basically similar. Comparison of Figure 6 with the 293°K results of Danner et al., obtained by the same experimental technique (Figure 3a), reveals some basic differences. The magnitudes of elastic to inelastic scattering differ, as well as the shape of the inelastic spectrum. A neutron energy scale has been added to Figure 6 to help in this comparison of the experimental results. It is difficult to explain the difference in the spectra without more information on the physical properties of the polyethylene target examined by Zemlyanov and Chernoplekov.

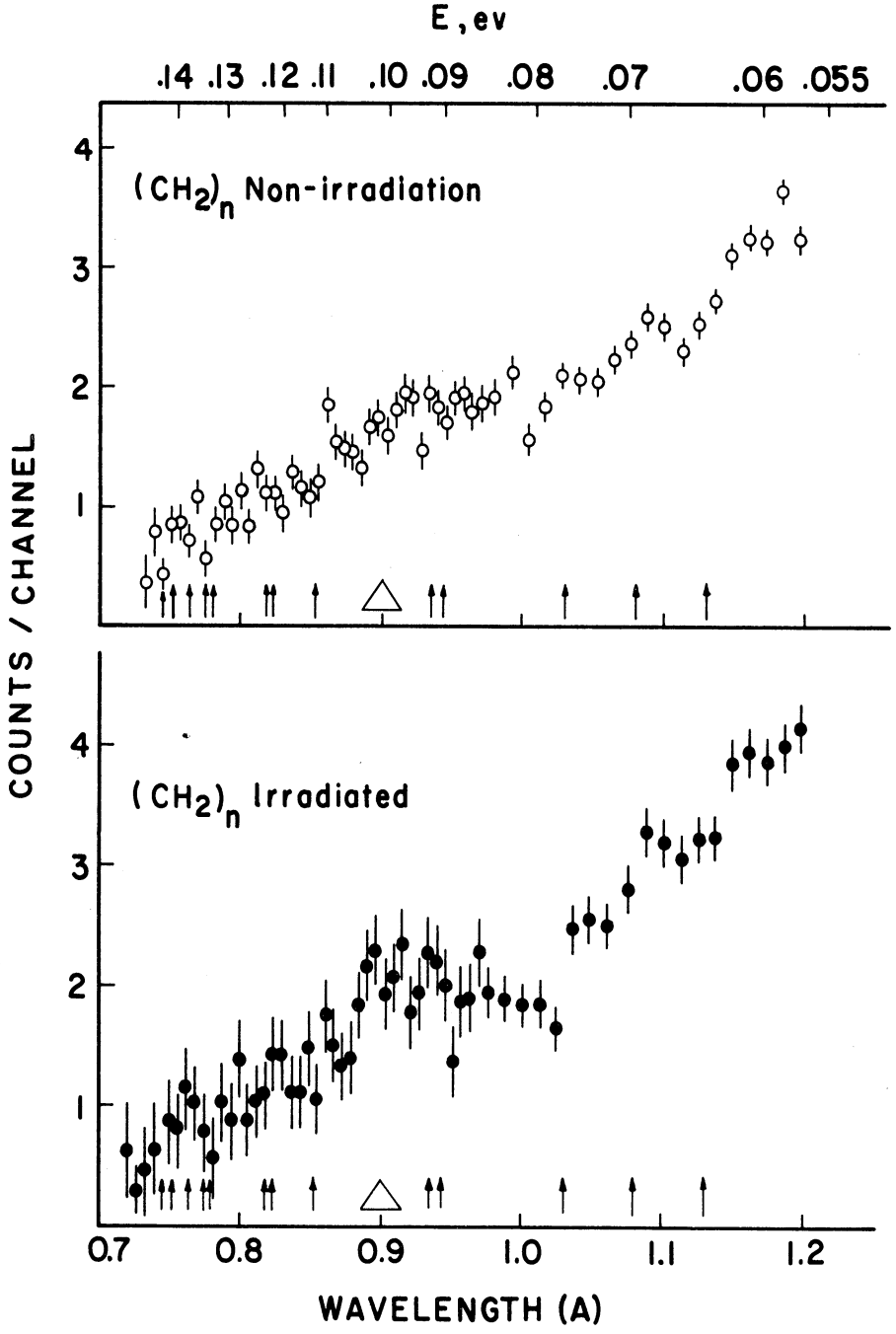

Figure 5. Spectrum of neutrons scattered by irradiated and non-irradiated polyethylene in the wavelength interval 0.7 to 1.2 A. (10)

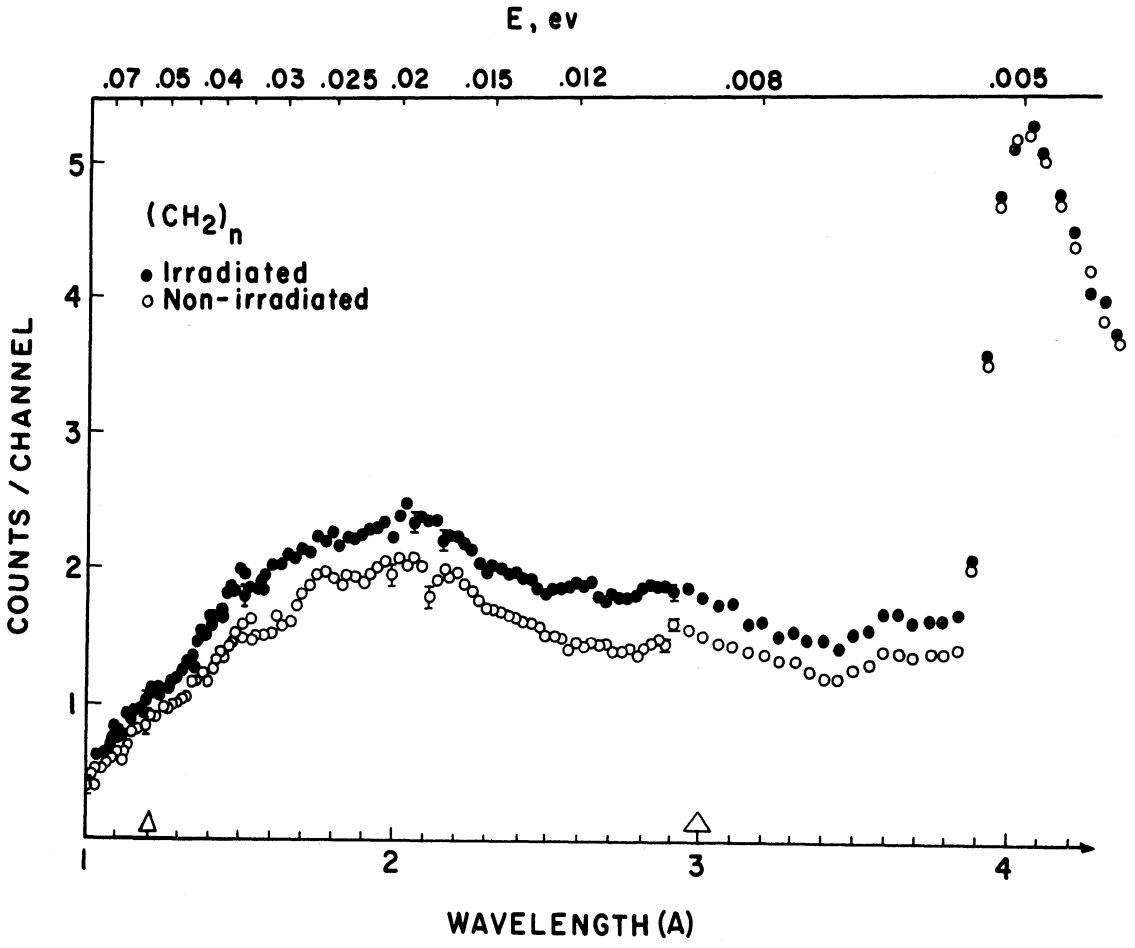

Figure 6. Spectrum of neutrons scattered by irradiated and non-irradiated polyethylene in the wavelength interval 1.2 to 4.5 A. (10)

Specific heat measurements

The best published measurements on the specific heat of polyethylene at constant pressure (c_p) have been carefully compiled by Wunderlich (8) and the data used to compute the specific heat at constant volume, c_v. Attempts to get a frequency spectrum directly by an inversion of the specific heat curve failed; the result was usually only a smoothed spectrum. An attempt at an inversion to the integral spectrum led to oscillating solutions which could only be made well behaved by such amounts of smoothing that the results were unusable. These results demonstrated the fact that specific heat is relatively insensitive to changes in the vibrational spectrum, especially at higher frequencies.

Wunderlich used the theoretical calculation of Tasumi, Shimanouchi and Miyazawa (9) for the normal vibrations of an infinite, uncoupled, and extended polyethylene chain to construct a composite frequency spectrum from the calculated dispersion curves. Because the model ignored the influence of intermolecular coupling, the low frequency region of the spectrum was adjusted to obtain agreement with the measured specific heat data. The adjustment was based on two experimental parameters: (1) a ν^2 dependence of the frequency spectrum in the low frequency region, based on the T^3 low-temperature law, which was cut-off at 50 cm^{-1} to obtain agreement with the experimental data; (2) the ratio of the vibrations in the two linear frequency regions, 50 - 110 cm^{-1} and 190 - 370 cm^{-1}. The amplitude of the

two linear portions was adjusted to make the area of the frequency spectrum agree for the two acoustic modes. The resulting "best-fit" frequency spectrum is shown in Figure 7. This spectrum does not agree very well in certain respects with the frequency spectrum measured by Danner et al. (1), Figure 4b. In particular, the structure below the acoustic mode at 190 cm^{-1} does not resemble the Danner spectrum, and the frequency region between 200 and 450 cm^{-1} has much less amplitude.

The inelastic scattering experiments reported in this thesis confirm the existence of the two acoustic modes predicted by the single chain theory. They also verify the existence of two other vibrational frequencies seen in the cold neutron results (65 cm^{-1} and 135 cm^{-1}) and suggest some additional frequencies. They support approximately the results of Danner et al. in the frequency region between the two acoustic modes, i.e., the large amplitude relative to the specific heat prediction. The higher frequency acoustic mode near 500 cm^{-1} is seen more clearly and with better statistics than in any previous measurement. The temperature dependence of the phonon frequency spectrum observed in the "cold" neutron experiments is confirmed, but found to be more dramatic. It is believed that the general agreement between the "cold" and "warm" neutron results demonstrates that a triple axis crystal spectrometer can be used successfully for incoherent, inelastic scattering experiments using the energy loss technique with "warm" neutrons.

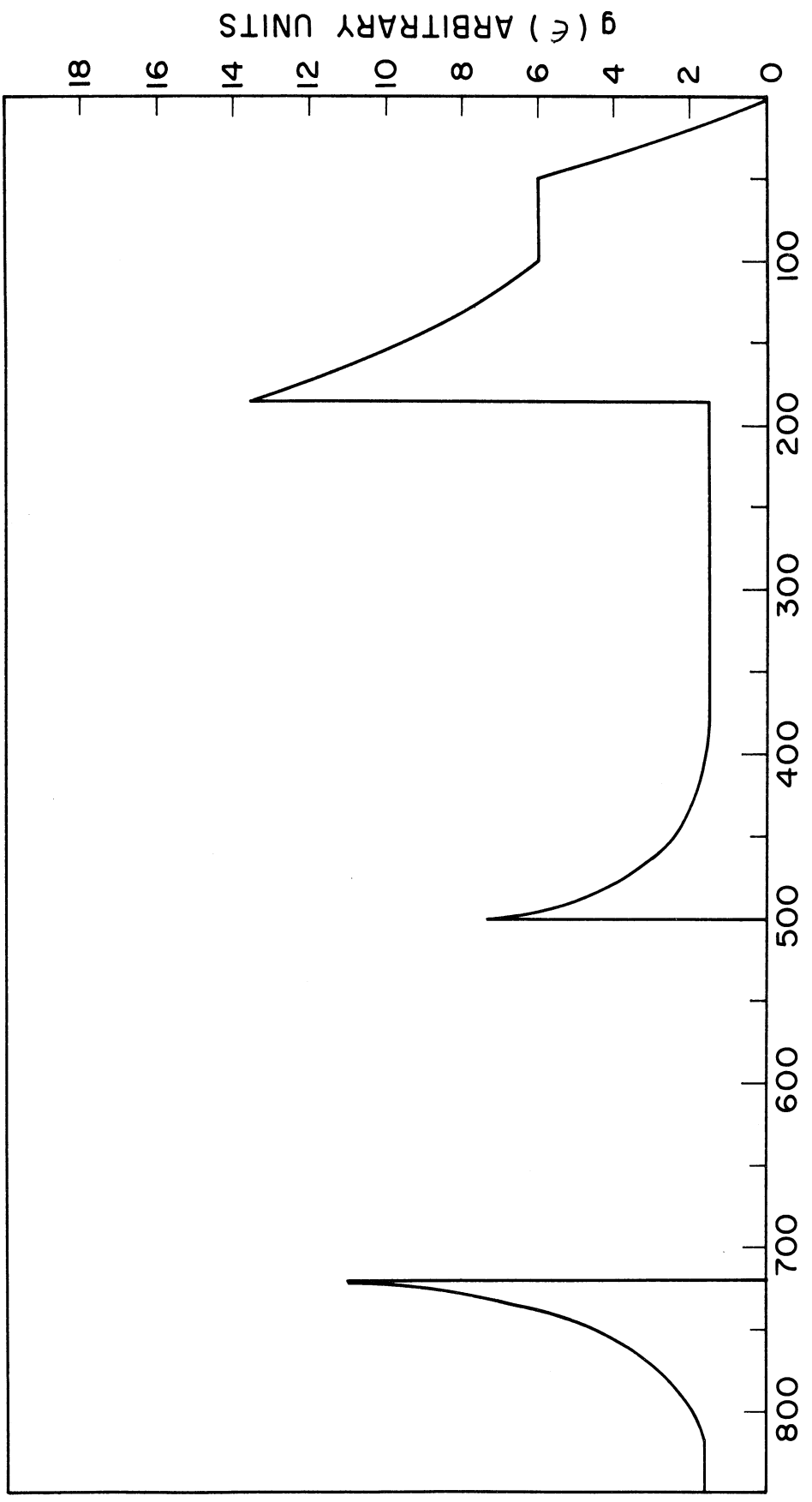

Figure 7. "Best-Fit" frequency spectrum calculated by Wunderlich (8) from specific heat data.

CHAPTER II

THEORY

Neutron scattering in solids

This section briefly outlines the theory for the interaction of thermal neutrons with solids. A general expression for the differential cross section is obtained; the incoherent cross section is presented in the zero, one and two phonon approximations. The development follows the treatments of Zemach and Glauber (11) and of Sjolander (12) as applied to polyethylene by Summerfield (13). The scattering system is a collection of nuclei in the solid state. The nuclei have energy eigenstates $|\ell\rangle$ such that

$$H|\ell\rangle = E_\ell|\ell\rangle$$

and

$$|\ell\rangle = |\psi_\ell(\underline{r}_1, \cdots\cdots, \underline{r}_n)\rangle \qquad \text{(II-1)}$$

where H is the Hamiltonian of the collection of nuclei, and $\underline{r}_i$ is the position vector of the i-th nucleus. A neutron at $\underline{r}$ interacts with all nuclei in the solid with an interaction potential $V(\underline{r})$ taken as the superposition of the N two-body neutron-nucleus potentials $V_b(\underline{r} - \underline{r}_b)$:

$$V(\underline{r}) = \sum_{b=1}^{N} V_b(\underline{r} - \underline{r}_b) \qquad \text{(II-2)}$$

where N is the number of nuclei in the system.

Consider an interaction in which the neutron momentum changes from k to k′ while the molecule simultaneously undergoes a transition between the initial and final states ψ_i and ψ_f for which the molecular energies are E_i and E_f respectively. In the Fermi pseudopotential approximation, the first Born approximation is used with the potential:

$$V(\underline{r}) = \sum_{b=1}^{N} \frac{2\pi\hbar^2}{m} a_b \delta^3(\underline{r} - \underline{r}_b) \qquad \text{(II-3)}$$

to obtain the angular differential cross section for neutron scattering from the nuclei(28). In (II-3), a_b is the bound atom scattering length for the b-th nucleus, and m is the mass of the neutron. The cross section, including an energy conservation condition is:

$$\frac{d\sigma_{fi}}{d\Omega} = \int \frac{k'}{k} \left| \langle \psi_f | \int e^{-i(\underline{K}\cdot\underline{r})} \sum_b a_b \delta^3(\underline{r} - \underline{r}_b) d^3r \, | \psi_i \rangle \right|^2$$
$$(x)\ \delta(\epsilon + E_i - E_f)\, d\epsilon$$
$$= \int \frac{k'}{k} \left| \langle \psi_f | \sum_b a_b e^{-i\underline{K}\cdot\underline{r}_b} | \psi_i \rangle \right|^2 \delta(\epsilon + E_i - E_f) d\epsilon \qquad \text{(II-4)}$$

where $\underline{K} = \underline{k}' - \underline{k}$, where k' and k refer to the final and initial wave vectors. The energies in equation (II-4) must obey conservation of energy, $\epsilon = E_f - E_i$, where ϵ is the energy transfer, and the final neutron energy must be non-negative $\epsilon \leq E_i$, where $E_i = \hbar^2 k^2 / 2m$ is the initial neutron energy. The angular differential cross section (II-4), is summed over all final system states and averaged over a thermal distribution of

initial states. The differential cross section per unit energy gain is:

$$\frac{d^2\sigma}{d\Omega\, d\epsilon} = \sum_{f,i} \sum_{b} \frac{k'}{k} \frac{e^{-\beta E_i}}{Z} \left| \langle \psi_f | a_b e^{-i \underline{K}' \cdot \underline{r}_b} | \psi_i \rangle \right|^2 \delta(\epsilon + E_i - E_f) \quad \text{(II-5)}$$

where $\beta = (k_B T)^{-1}$ and $Z = \sum_i e^{-\beta E_i}$

The expectation value in equation (II-5) can be evaluated approximately by representing the N nuclei as coupled harmonic oscillators vibrating about fixed lattice positions. The instantaneous position of the S-th particle in the ℓ-th unit cell is $\underline{R}_\ell^s$, or

$$\underline{R}_\ell^s(t) = \underline{X}_\ell^s + \underline{u}_\ell^s(t) \quad \text{(II-6)}$$

where $\underline{u}_\ell^s(t)$ is the instantaneous displacement from the equilibrium position $\underline{X}_\ell^s$.

The Hamiltonian for this system is approximately:

$$H = \sum_{s\ell\alpha} \frac{m_s \dot{u}_{s\ell\alpha}^2}{2} + \sum_{\substack{s\ell\alpha \\ s'\ell'\alpha'}} \frac{1}{2} u_{s\ell\alpha}\, u_{s'\ell'\alpha'}\, A_{s\ell\alpha}^{s'\ell'\alpha'} \quad \text{(II-7)}$$

where α refers to the direction components of the displacements in a cartesian coordinate system fixed in the lattice, and

$$A_{s\ell\alpha}^{s'\ell'\alpha'} = \left[\frac{\partial^2 \mathcal{U}}{\partial u_{\ell\alpha}^s \, \partial u_{\ell'\alpha'}^{s'}} \right]_0$$

where subscript o means that the second order derivitive of the interparticle potential energy, $\mathcal{U}$, is to be evaluated at the

equilibrium positions.[1] In (II-7) the potential energy term contains cross product terms in the displacements. To eliminate the cross product terms, a new set of coordinates, the normal coordinates, are introduced for the actual displacements in the vibrating lattice. The transformation from the time dependent displacements $u_{s\ell\alpha}$ to the normal coordinates is given by Born and Huang (29). Using normal coordinates the Hamiltonian becomes the sum of the kinetic and potential energy of 3 N uncoupled harmonic oscillators. Following the treatment of Zemach and Glauber (11), it is possible to express the expectation value in (II-5) as an exponential function. If the delta function also is replaced by its integral representation, (II-5) becomes in the incoherent approximation:

$$\frac{d^2\sigma}{d\Omega\, d\epsilon} = \frac{N k'}{2\pi\hbar k} \sum_s e^{-2W_s} \left| a^s_{inc} \right|^2 \int_{-\infty}^{\infty} dt\; e^{-i\epsilon t/\hbar}$$

$$(x)\; \exp\left\{ \sum_{j q \alpha} \frac{K_\alpha^2 \left(\gamma_j^{s\alpha}\right)^2 \hbar}{2 w_j m_s N} \left[\frac{e^{-i w_j t}}{1 - e^{-\beta\hbar w_j}} + \frac{e^{-i w_j t}}{e^{\beta\hbar w_j} - 1} \right] \right\} \tag{II-8}$$

where the index S refers to atoms within a unit cell, N is the

---

[1] In the absence of detailed knowledge of U, the approximation conventionally employed is that of Born and Oppenheimer (29, 30).

number of unit cells, a^s is the scattering length of the s-th atom, the indices j and q refer to the phonon branch and the phonon momentum, respectively, ω_j is the frequency of the j-th branch, α refers to the direction components on a cartesian coordinate system fixed in the lattice, and $2W_s$, the exponent in the Debye-Waller factor is given by:

$$2W_s = \sum_{jq\alpha} K_\alpha^2 \left(\gamma_j^{s\alpha}\right)^2 \frac{\hbar}{2\omega_j m_s N} \frac{1+e^{-\beta\hbar\omega_j}}{1-e^{-\beta\hbar\omega_j}} \qquad \text{(II-9)}$$

K_α is the component of momentum transfer in the direction α and the $\gamma_j^{s\alpha}$ are the normalized eigenvectors of the secular matrix (9):

$$C_{s\alpha}^{s'\alpha'}(q) = \sum_{\ell=-\infty}^{\infty} e^{-(q\cdot\ell)\ell} A_{s\ell\alpha}^{s'\ell'\alpha'} \left(m_s m_{s'}\right)^{-1/2}$$

$$\sum_{s\alpha} C_{s\alpha}^{s'\alpha'}(q)\, \gamma_j^{s\alpha} = \omega_j^2\, \gamma_j^{s'\alpha'}$$

$$\sum_{s\alpha} \gamma_j^{s\alpha}\, \gamma_{j'}^{s\alpha} = \delta_{jj'}$$

To apply the cross section expression, equation (II-8), to the scattering from polyethylene, several approximations are made. The average overall directions of $\underline{K}$ for the randomly oriented polyethylene chains is approximated by:

$$\langle F(K_\alpha^2)\rangle = F(\langle K_\alpha^2\rangle) = F\left(\frac{K^2}{3}\right)$$

This approximation is considered to be good for neutron scattering from low temperature polyethylene. The sum on α is then just an average of the eigenvectors, $\gamma_j^{s\alpha}$, over all directions

and can be approximated by:

$$\sum_{\alpha} \left(\gamma_j^{s\alpha} \right)^2 = \frac{m_s}{M_c}$$

where

$$M_c = \sum_{s} m_s$$

This approximation can be justified for simple models if, in a particular normal mode, all the atoms within a unit cell move with the same amplitude.

The sums over j and q are performed by introducing the frequency distribution function, $g(\hbar\omega)$, which is defined as the number of frequencies in the interval $d\omega$ about ω. The number of frequencies is equal to the number of degrees of freedom; the normalization of $g(\hbar\omega)$ is:

$$\int_0^\infty g(\hbar\omega)\, d(\hbar\omega) = 18 N_o$$ where $18 N_o$ is the number of unit cells.

For the polyethylene one-dimensional chain, there are six atoms per unit cell, and hence 18 phonon branches, each doubly degenerate because of reflection symmetry, so that there are nine dispersion curves. The sums over j and q are expressed in terms of the phonon frequency distribution according to:

$$\sum_{j,q} \{\quad\} = \int d(\hbar\omega)\, g(\hbar\omega) \{\quad\}$$

With these approximations, the zero, one, and two phonon cross sections are obtained by a series expansion of the time dependent exponent in (II-8), following the method of Sjolander (12), commonly known as the "phonon expansion."

These three cross sections are:

Zero:

$$\frac{d^2\sigma^{(0)}}{d\Omega\, d\epsilon} = \frac{N k'}{k}\,\delta(\epsilon)\sum_s \left|a^s_{inc}\right|^2 e^{-2W} \qquad \text{(II-10)}$$

One:

$$\frac{d^2\sigma^{(1)}}{d\Omega\, d\epsilon} = \frac{k'}{k}\sum_s \left|a^s_{inc}\right|^2 e^{-2W}\frac{\hbar^2K^2}{6M_c}\int d\epsilon'\,\frac{g(\epsilon')}{\epsilon'}\left[\frac{\delta(\epsilon'-\epsilon)}{1-e^{-\beta\epsilon'}} + \frac{\delta(\epsilon'+\epsilon)}{e^{\beta\epsilon'}+1}\right] \qquad \text{(II-11)}$$

Two:

$$\frac{d^2\sigma^{(2)}}{d\Omega\, d\epsilon} = \frac{k'}{k}\sum_s \left|a^s_{inc}\right|^2 \frac{e^{-2W}}{9}\left(\frac{\hbar^2K^2}{2m}\right)^2\int d\epsilon'\int d\epsilon''\,\frac{m^2}{2NM_c^2}\,\frac{g(\epsilon')g(\epsilon'')}{\epsilon'\epsilon''}$$

$$(X)\left\{\frac{\delta(\epsilon'+\epsilon''-\epsilon)}{(1-e^{-\beta\epsilon'})(1-e^{-\beta\epsilon''})} + \frac{2\delta(\epsilon'-\epsilon''-\epsilon)}{(1-e^{-\beta\epsilon'})(e^{\beta\epsilon''}-1)} + \frac{\delta(\epsilon'+\epsilon''+\epsilon)}{(e^{\beta\epsilon'}-1)(e^{\beta\epsilon''}-1)}\right\} \qquad \text{(II-12)}$$

where the Debye-Waller factor is:

$$2W = \frac{\hbar^2K^2}{2m}\int d\epsilon\,\frac{m}{3M_cN}\,\frac{g(\epsilon)}{\epsilon}\,\frac{1+e^{-\beta\epsilon}}{1-e^{-\beta\epsilon}} \qquad \text{(II-13)}$$

In the experiments reported in this thesis, neutron energy loss in scattering from the polyethylene target was observed. The one phonon incoherent cross section, (II-12), becomes:

$$\frac{d^2\sigma^{(1)}}{d\Omega\, d\epsilon} = \frac{k'}{k}\,\frac{\hbar^2 K^2}{6M_c}\sum_s |a^s_{inc}|^2 e^{-2W}\,\frac{g(\epsilon)}{\epsilon}\,\frac{1}{1-e^{-\beta\epsilon}} \tag{II-14}$$

Using (II-14), the one phonon frequency distribution is calculated from the measured cross section:

$$g(\epsilon) = \frac{k}{k'}\left[\sum_s |a^s_{inc}|^2\right]^{-1} e^{2W}\,\frac{6M_c}{\hbar^2 K^2}\,\epsilon\left(1-e^{-\beta\epsilon}\right)\,\frac{d^2\sigma}{d\Omega\, d\epsilon} \tag{II-15}$$

Calculation of vibrational frequencies of polyethylene

To identify the observed frequency distribution function with physical motions of the molecule, it is necessary to obtain, if possible, a theoretical g (ϵ) function from the equations of motion of the complete lattice. At low temperature (90°K) the internal rotations are assumed to be absent, and translation and rotation of the molecule as a whole are excluded because of the large size of the polyethylene molecule. A normal mode calculation is necessary to give a complete description of the remaining internal vibrational motions and in the general case, a solution of the equations of motion in normal coordinates is required.

To obtain a potential energy expression which leads to a secular determinant which can be solved, various assumptions

as to the nature of the force field and force constants have been made. Perhaps the simplest approach, originated by Kirkwood (14) and applied to the polyethylene chain by Liang, Krimm and Sutherland (32), replaces the CH_2 groups by point masses arranged in a planar zig-zag configuration. A more realistic treatment by Tasumi, Shimanouchi and Miyazawa (9) includes the separate motions of all the nuclei. It is based on a potential including a semi-empirical set of Urey-Bradley force constants, and the assumption that the frequencies of the normal vibrations are determined primarily by the intramolecular force field. This calculation gives the dispersion curves for all nine vibrational modes. Three of these modes are included in the frequency range 0 -800 cm^{-1}: two acoustic modes, ν_5 and ν_9 with high frequency limits at 500 cm^{-1} and 190 cm^{-1} respectively, and one optical mode ν_8, with a low frequency limit at 720 cm^{-1}. These three modes, plus the next lowest optical mode, ν_4 are shown in Figure 8.

Both the calculations of Liang, Krimm and Sutherland (32) and the calculations of Tasumi, Shimanouchi and Miyazawa (9) predict frequencies in good agreement with the observed infrared absorption bands for the optical modes, although the point mass treatment results in an incorrect inversion of the $\nu_4(0)$ and $\nu_4(\pi)$ skeletal frequencies. Prior to the neutron scattering data, verification of the acoustic mode predictions has presumably not been possible. However, the acoustic modes are most sensitive to the intermolecular force field which has

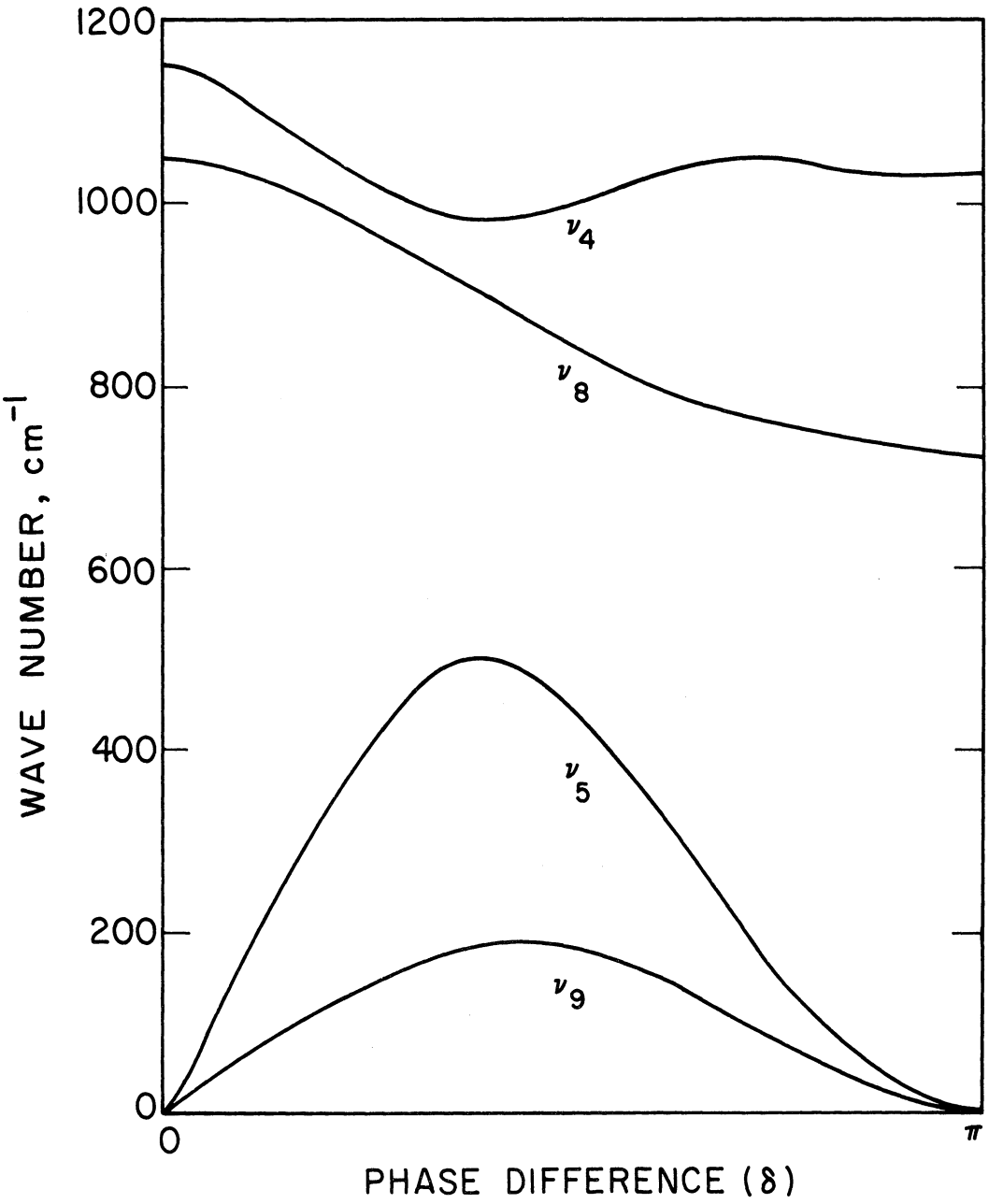

Figure 8. Calculated polyethylene frequency-phase difference curves for ν_5, ν_9, ν_4, and ν_8 in an infinite trans-planar polyethylene chain.

been ignored in these calculations. The existence of this force field can be inferred from the observed splitting of infrared absorption bands.

To present a more complete description including the effects due to inter- as well as intramolecular forces, Tasumi (18) estimated the normal frequencies of crystalline polyethylene. The unit cell, which contains two chains, is shown in cross sections in Figure 9(a). An intermolecular potential, describing the forces between hydrogen atoms closer than 3Å to each other, was added to the intramolecular potential and a perturbation treatment applied to the single chain calculation. The intermolecular force constants were evaluated from the observed splitting (doublets) in the infrared optical spectra. The perturbation method was justified because the intermolecular force constants are small compared to the intramolecular force constants. The secular equation was again solved for phase differences of 0 and π. The results are shown in Table 3 together with the optical frequencies observed in infrared spectra. The dispersion curves for the acoustic modes, ν_5 and ν_9 are split and shifted to higher frequency limits by the addition of the intermolecular force field, and non-zero intercepts occur for 0 and π phase differences. Tasumi also calculated the frequencies for a phase difference of 60° and these are given in Table 4. Although the values for $\nu_5(60°)$ are increased only by a small amount, the values of $\nu_9(60°)$ have increased from 172 cm^{-1} to 214 and 230 cm^{-1}. If it is

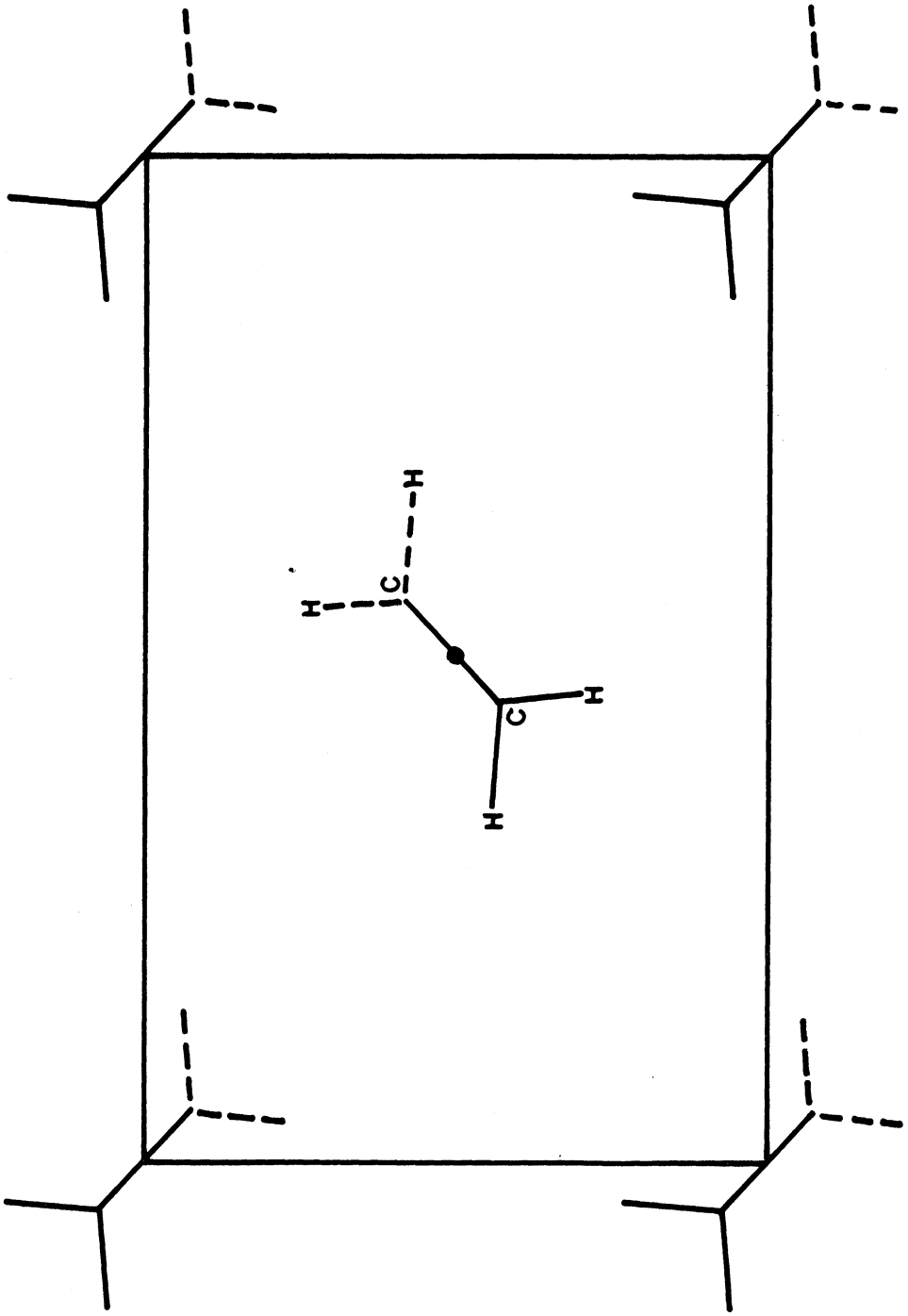

Figure 9. Cross section perpendicular to the chain axis of the polyethylene unit cell.

TABLE 3

POLYETHYLENE FREQUENCIES (cm^{-1}) CALCULATED BY TASUMI (18) AND OBSERVED IN INFRARED MEASUREMENTS

Mode	ν_{obs}	ν_{calc}	Δ_{obs}	Δ_{calc}
$\nu_1(0)$	2848	2844	---	6
		2838		
$\nu_1(\pi)$	2851	2874	---	3
		2877		
$\nu_2(0)$	1440	1437	24	17
	1464	1454		
$\nu_2(\pi)$	1473	1488	10	9
	1464	1479		
$\nu_3(0)$	1175	1183	---	8
		1175		
$\nu_3(\pi)$	1415	1413	(0)	5
		1408		
$\nu_4(0)$	1131	1127	(0)	0
		1127		
$\nu_4(\pi)$	1061	1051	(0)	4
		1055		
$\nu_5(0)$	---	57	---	---
	---	0		
$\nu_5(\pi)$	---	0	---	---
	---	104		
$\nu_6(0)$	2883	2899	---	5
		2904		

TABLE 3--Continued

Mode	ν_{obs}	ν_{calc}	Δ_{obs}	Δ_{calc}
$\nu_6(\pi)$	2919	2917	---	2
		2919		
$\nu_7(0)$	1168	1164	(0)	0
		1164		
$\nu_7(\pi)$	1295	1303	(0)	5
		1308		
$\nu_8(0)$	---	1052	(7)	7
	1050	1059		
$\nu_8(\pi)$	731	747	11	10
	720	737		
$\nu_9(0)$	---	169	---	36
	---	133		
$\nu_9(\pi)$	---	74	---	---
	---	0		

TABLE 4

POLYETHYLENE FREQUENCIES (cm^{-1}) CALCULATED BY TASUMI (18) FOR $\delta = 60°$

Mode	ν_{calc}
ν_1	2852
	2848
ν_2	1458
	1448
ν_3	1266
	1260
ν_4	995
	995
ν_5	503
	502
ν_6	2908
	2904
ν_7	1273
	1267
ν_8	878
	877
ν_9	230
	214

assumed that these calculated frequencies apply to the crystalline regions in polyethylene, new frequency values can be expected to appear in the frequency spectra. The non-zero intercepts for ν_5 and ν_9 are all in the low frequency region below 200 cm^{-1}. However, this model also predicts that the high frequency limits are increased, especially the ν_9 values. These limits were not calculated by Tasumi, but can be estimated to increase from 190 cm^{-1} to about 232 cm^{-1} and 248 cm^{-1}. The neutron scattering data appear to demonstrate frequencies that agree reasonably well with the values of the intercepts predicted at 0 and π phase difference, but the strong acoustic peak remains near 190 cm^{-1}.

Effects of temperature

The theoretical predictions of the vibrational frequencies discussed above for the polyethylene molecule describe the molecule at room temperature. The temperature dependence of the calculated frequencies is not known, so that comparison of these calculations and the results measured at 90°K is uncertain to a small degree. The infrared measurements of Bertie and Whalley (6) report a change in an observed band from 72.5 cm^{-1} at 300°K to 79 cm^{-1} at 100°K, a shift of 9% over this temperature range. However, it is expected that the force constants depending on separation distances along the carbon skeleton axis will be much less temperature dependent since the axial expansion coefficient is smaller than the coefficient for

expansion perpendicular to the axis. The acoustic motions are skeletal vibrations, so the influence of temperature on these modes is expected to be small.

A second temperature effect in polyethylene is the presence of hindered internal rotations at temperature above 120°K. Both specific heat data (8) and nuclear magnetic resonance measurements (19) indicate that hindered rotations occur in the amorphous regions of polyethylene. The beginning of these rotations defines the glass transition region. To eliminate this effect from the observed neutron scattering data, measurements were taken with the polyethylene target at 90°K.

A third temperature effect which influences the frequency distribution calculated from the observed neutron inelastic scattering cross section is the variation of multi-phonon processes with temperature. For example, the two phonon cross sections, equation (II-12) can be used with the one phonon cross section, equation (II-11), to demonstrate the temperature dependence of the two phonon correction term:

$$g^{(1+2)} = g(\epsilon) + C K^2 f(\epsilon, \beta) \qquad \text{(II-16)}$$

where C is a constant and $f(\epsilon, \beta)$ is given by:

$$f(\epsilon,\beta) = (1-e^{-\beta\epsilon}) \int d\epsilon' \int d\epsilon'' \frac{g(\epsilon')g(\epsilon'')}{\epsilon'\epsilon''} \times \left\{ \frac{\delta(\epsilon'+\epsilon''-\epsilon)}{(1-e^{-\beta\epsilon'})(1-e^{-\beta\epsilon''})} + \frac{2\delta(\epsilon'-\epsilon''-\epsilon)}{(1-e^{-\beta\epsilon'})(e^{\beta\epsilon''}-1)} \right\} \qquad \text{(II-17)}$$

An evaluation of the correction term, $C K^2 f(\epsilon, \beta)$, has been made to estimate the influence of two phonon events on the frequency distributions measured at various target temperatures but calculated according to the one phonon approximation. The magnitude of the correction can be minimized by using low target temperature. It should also be noted in equation (II-17) that the magnitude of the correction term depends on K^2. For a given energy transfer, a "warm" neutron experiment is associated with a larger value of K^2 than a "cold" neutron experiment; hence, the magnitude of the correction term is larger for "warm" neutron experiments.

CHAPTER III

INSTRUMENTATION

Design of the triple axis crystal spectrometer

The design of the triple axis crystal spectrometer is dominated by the need for high intensity in the experimental beam. To achieve enough intensity to do meaningful inelastic scattering experiments, several unique features have been incorporated into the spectrometer design. As always, however, the design represents a compromise between intensity and spectrometer resolution. The parameters that determine these two important features are the horizontal angular divergence of the collimators and the mosaic properties of the monochromator and analyzer crystals. The horizontal angular divergence of the collimators is fixed by the dimensions of the collimators themselves. The crystal parameters can be influenced by the surface treatment given the crystals. The subject of system resolution will be considered in detail in this chapter.

To obtain high intensity while still keeping good system resolution, the design included the use of a convergent primary collimator, two monochromator crystals to allow vertical focusing of the Bragg reflected beam, large beam dimensions, and multiple analyzer systems. The primary collimator, installed in the six inch diameter beam port "A,"

has a vertical aperture tapered from five inches at the source plane, to three inches over its length of 120 inches. One vertical shim is positioned at the center of the collimator. This shim limits the width of each of the horizontal apertures to 0.905 inches; the maximum horizontal angular divergence is 25.9 minutes; the vertical divergence is 1.91 degrees. The exit end of this collimator is nine inches from the monochromator crystals. The triple axis crystal spectrometer is shown in Figure 10. The location of the spectrometer and beam port "A" in relationship to the reactor core and the other beam ports is shown in Figure 11.

The two monochromator crystals are pieces cut from a seven inch long, 3-1/2 inch diameter cylindrical ingot of copper grown by the Semi-Elements Corporation, Saxonburg, Pennsylvania. This ingot has been sliced to provide six crystal plates; the flat surfaces of these plates are parallel to the (200) planes within an accuracy of $\pm$ 2°. Two of these crystal plates are mounted, one above the other, on the monochromator goniometer. The goniometer and monochromator crystals are shown in Figure 12. By slightly tilting the two crystals, the reflected Bragg beam can be focused at the target position, 52-1/2 inches from the crystals. The goniometer table allows each of the crystals to be tilted, rotated and translated independently of the other by remote motor drives.

The goniometer table is inside a twelve inch diameter hole in the shielding turret. A six inch thick sector of lead

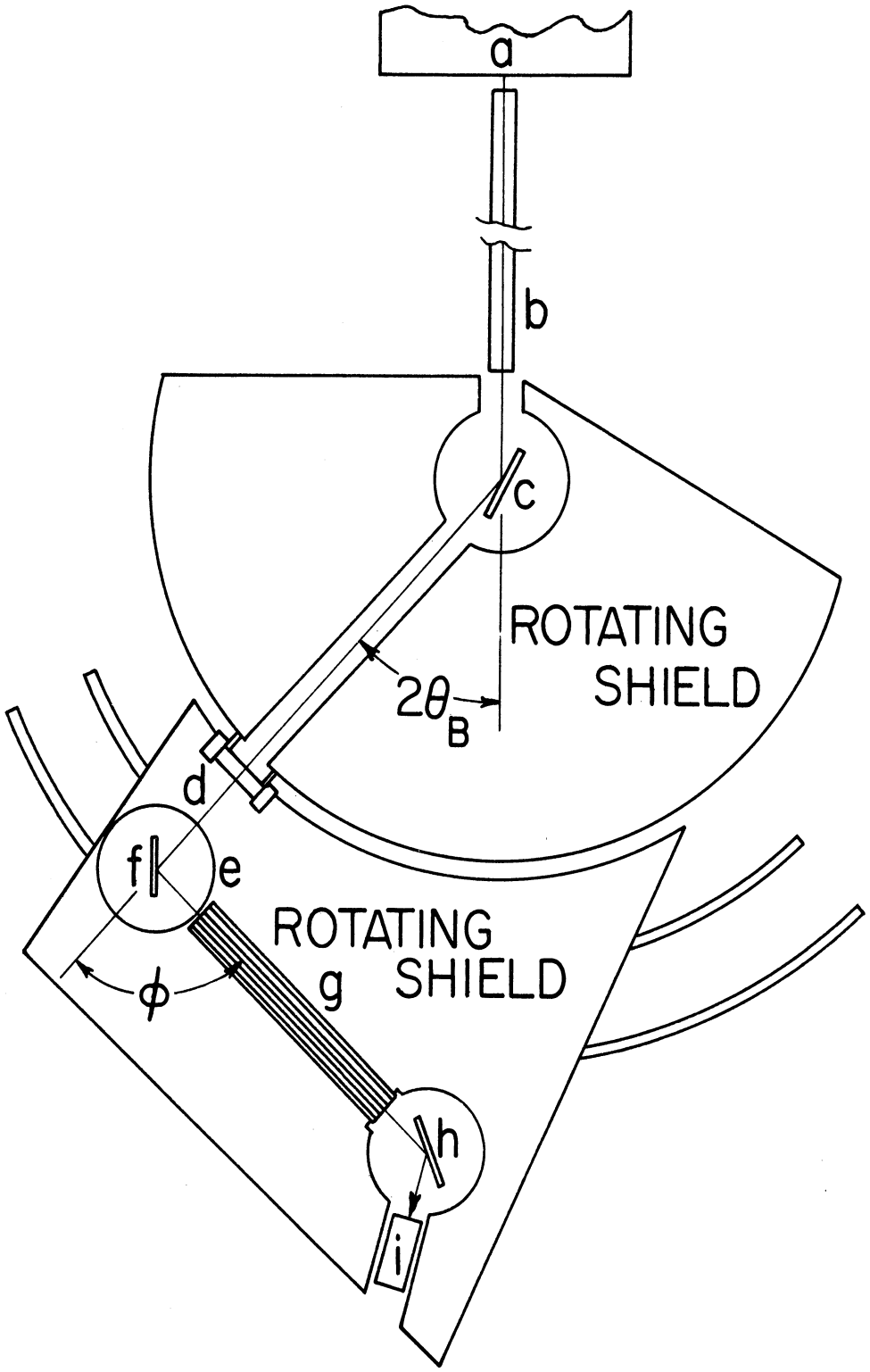

Figure 10. Triple axis crystal spectrometer. (a) Two megawatt FNR core. (b) Primary collimator. (c) Vertically focused copper monochromator crystals. (d) Primary beam monitor. (e) Cryostat. (f) Target. (g) Analyzer Soller collimators. (h) Copper analyzer crystal. (i) Three inch diameter BF_3 detector.

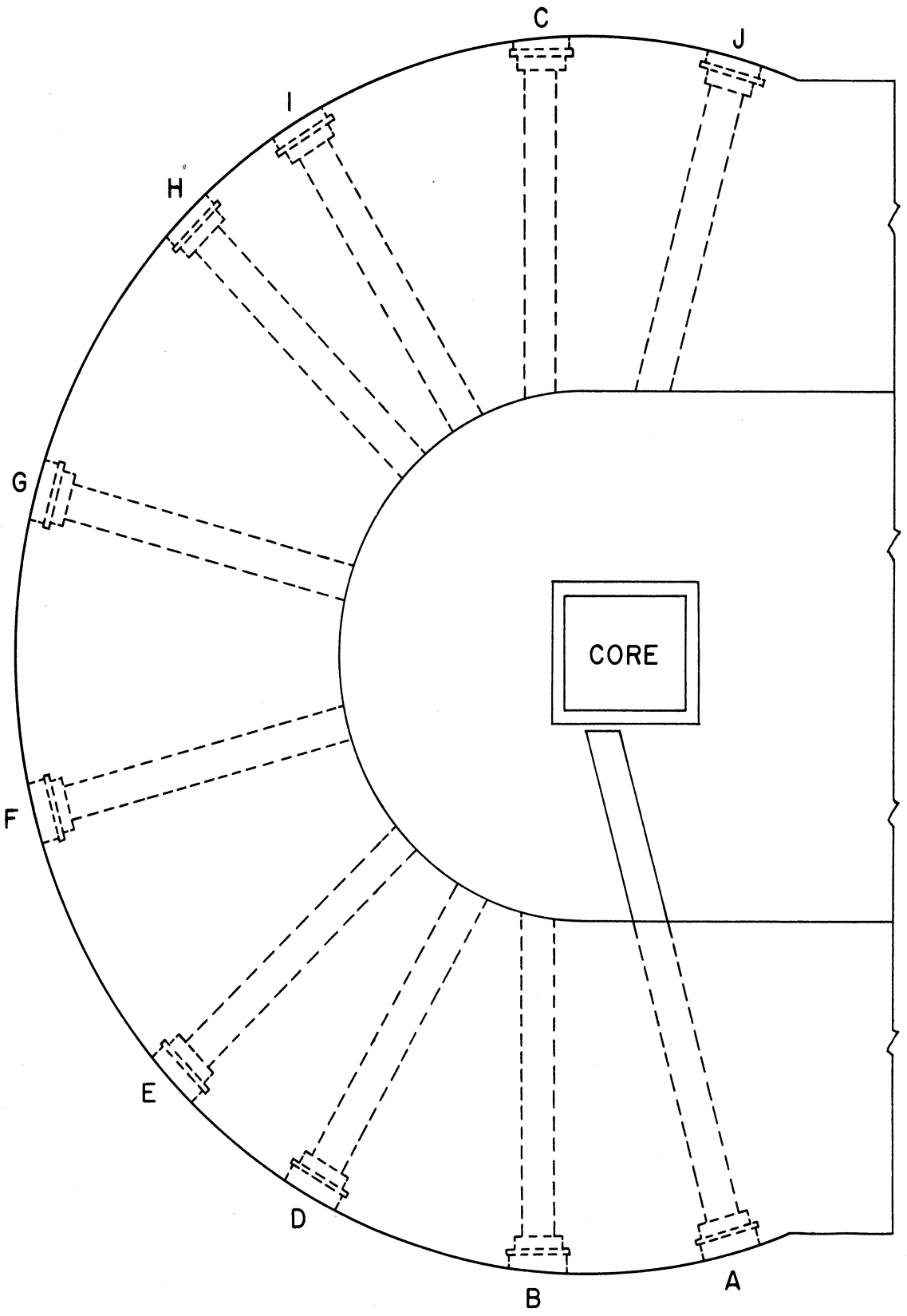

Figure 11. Reactor and beam port arrangement of the Ford Nuclear Reactor.

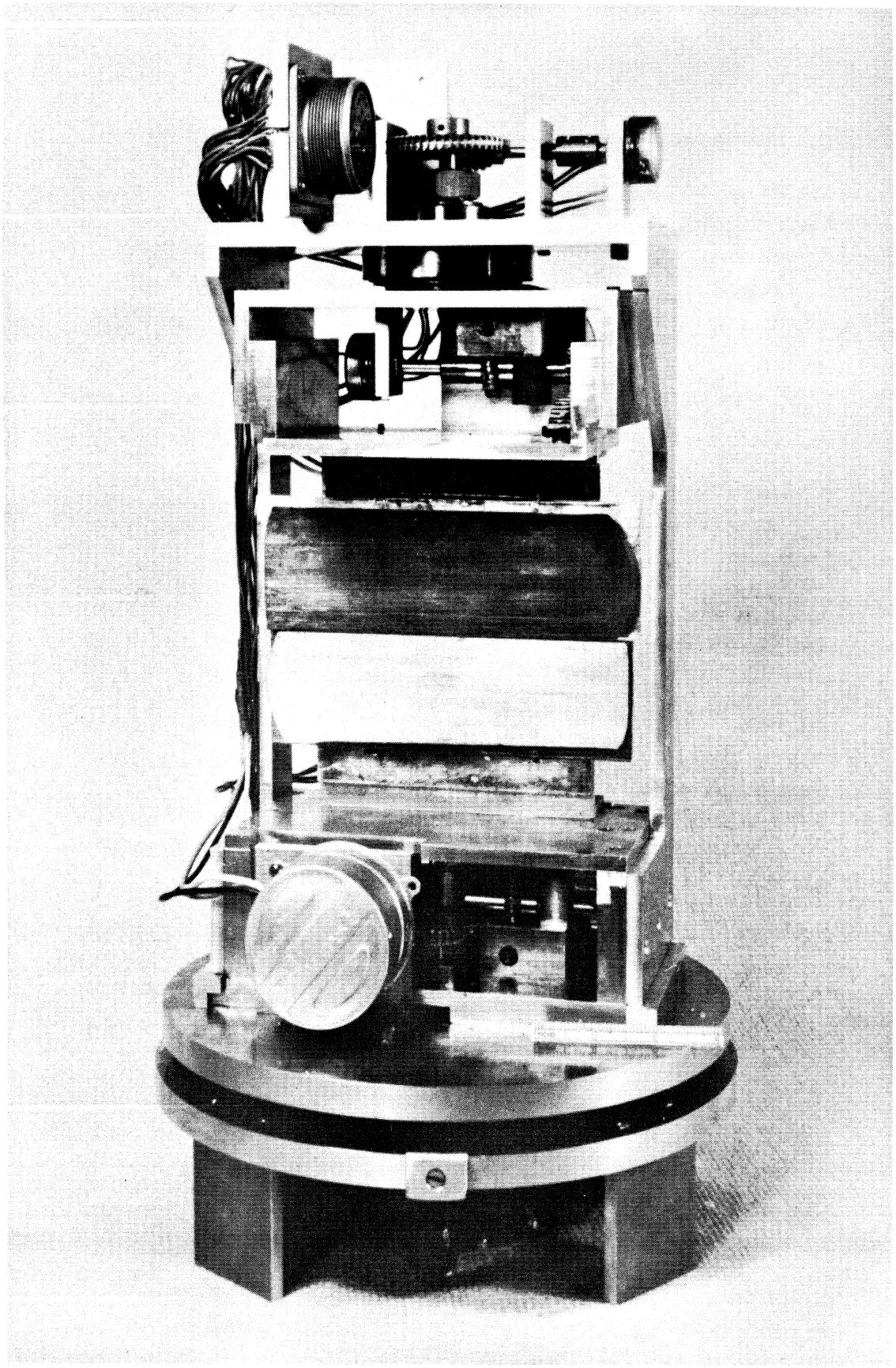

Figure 12. Goniometer and copper monochromator crystals.

is inserted in the the turret behind the monochromator crystals to absorb the gamma rays from the primary collimator; the rest of the turret is high density masonite (Benelux, 1.3 gms/cc). This material is an excellent shielding material for slowing down high energy neutrons because of the high hydrogen density. The radius of the turret is 36 inches; it can rotate 34° about the monochromator crystal axis. Four 3-1/2 inch diameter beam ports (30° apart) are used to obtain Bragg scattering angles from -1° to 45°. For most experiments, one beam port is adequate; the Bragg angle is varied from 30° to 13°. Masonite plugs are inserted in the three beam ports not in use. A transmission type fission monitor is mounted at the exit of the open beam port.

The main Bragg arm is mounted below the turret and coaxial with the axis of rotation of the goniometer table. The 2:1 turning motion between the crystals and the Bragg arm is obtained through 0.020 inch thick 3/8 inch steel bands which wind around precision drums. The 2:1 motion showed a measured accuracy of 1.0 minutes in 90° of rotation of the Bragg arm. The Bragg arm supports the target table, where the material under investigation is positioned in the neutron beam. The turret, target table, fission monitor and Bragg arm are shown in Figure 13.

This figure also shows the large shielding tanks which are used to reduce the background in the experimental area. Water filled shielding tanks are positioned at both sides of the turret; these two tanks support a third large water filled

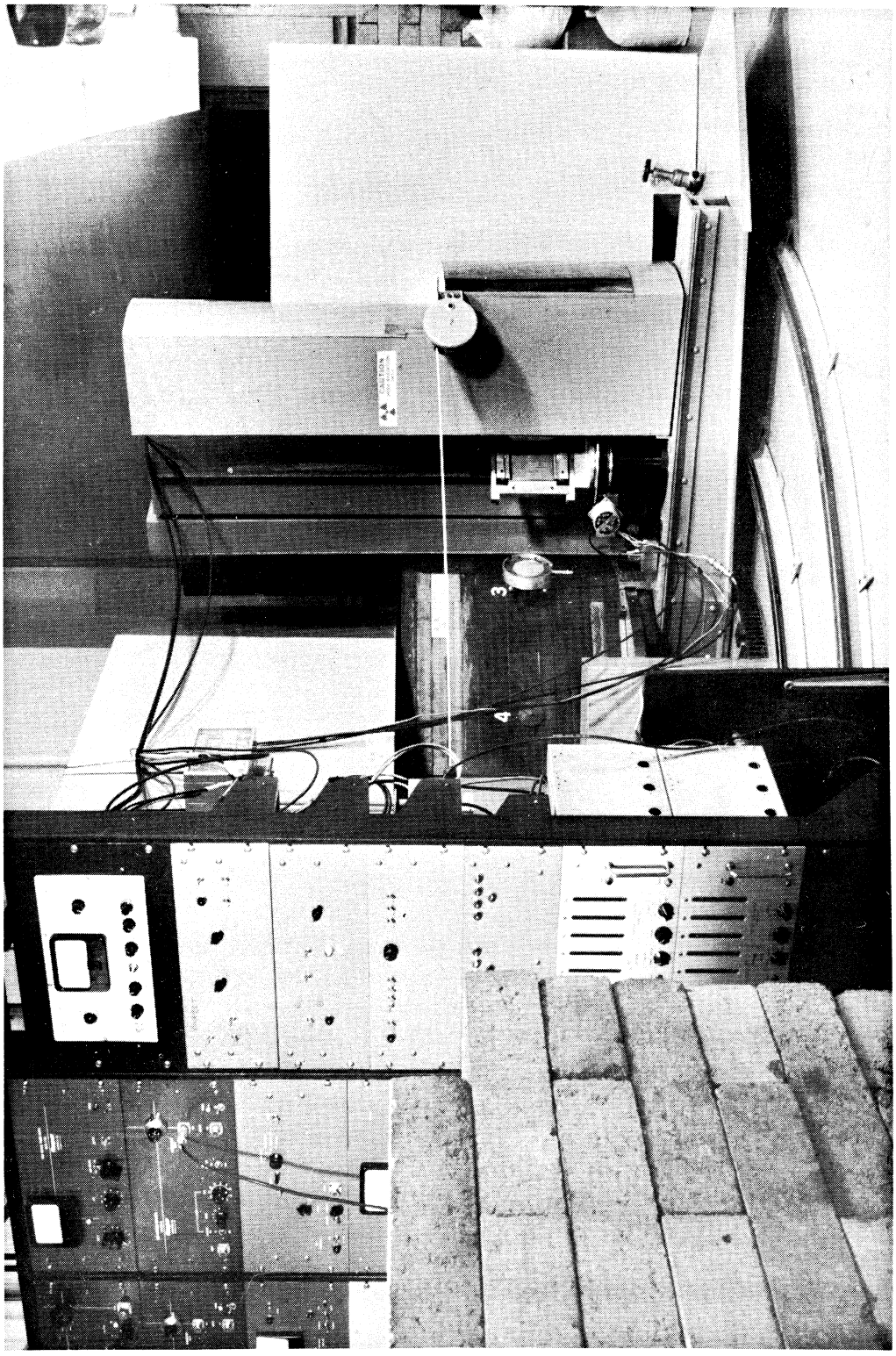

Figure 13. Front view of the triple axis crystal spectrometer.

tank which covers the top of the turret. The tanks in front of the turret form a cave surrounding the neutron detectors. These tanks are water filled also, except for the quadrant around the target table. This shield is filled with borated paraffin and supports the four analyzer collimators. The complete detector cave, which weighs approximately 7,000 pounds, is supported on a one inch thick aluminum plate which rides on two railroad tracks mounted on the floor; the plate is attached to the main Bragg arm. The tracks, which are concentric with the axis of rotation of the turret, can be seen in Figure 13. For the present experiment, the analyzer collimators are positioned at 90 degrees to the experimental beam.

The four analyzer collimators are hollow polyethylene boxes, 3" x 3" x 18" long. Eighteen cadmium plated .0156 inch steel shims are inserted in accurately milled Soller slots. The cadmium plating thickness varies from about 0.0005 inches at one end of the shims, to 0.001 inch at the other end. The horizontal angular divergence of these analyzer collimators is 25.0 minutes; the vertical divergence is 7.5 degrees. The front face of each collimator is six inches from the center of the target. The rotation axes of the analyzer crystals are located five inches from the back face of the analyzer collimators. In the present experiment, only three of the four analyzer collimators were used. The center collimator is in the horizontal plane of the incident beam (horizontal scattering plane); the other two are positioned above and below this collimator, requiring a tilt in the scattering planes of $\pm$ 18.2°.

The copper analyzer crystals are supported on an integral analyzer collimator-crystal-detector assembly. This assembly is bolted to the quadrant shield to focus on the center of the target. Alignment of the collimator, analyzer crystal and BF_3 neutron detector tube is fixed by this rigid assembly. Gears are used to provide 2:1 motion between the analyzer crystals and the detectors. The detectors are positioned inside boron carbide filled shield cans. The shield cans are 15 inches long, 7-1/8 inches in diameter and provide a 3-1/8 inch diameter, 13-1/2 inch long annulus to hold the BF_3 detectors. The boron carbide powder inside the cans has a density of 1.6 gms/cc. The shield cans begin four inches from the axis of the analyzer crystals; the entrance windows of the detectors are 8-1/2 inches from the crystal rotation axes.

The neutron beam leaving the primary collimator is three inches high by 1.86 inches wide. At the target position, it is about 4.7 inches high and 3.5 inches wide; the horizontal and vertical full widths at half maximum are, respectively, 1-3/4 and 2-1/2 inches. Measured profiles at the target position are shown in Figure 14. Because the target is positioned at 45° to the experimental beam, the effective area of the beam on the target surface is 4.7 inches high by 5 inches wide. The analyzer collimators are 2-3/8 inches high by 2.80 inches wide.

The scattering experiments are carried out by varying the incident energy while keeping the analyzer energy fixed. This arrangement was incorporated into the spectrometer design for several reasons. First, by keeping the analyzer energy fixed,

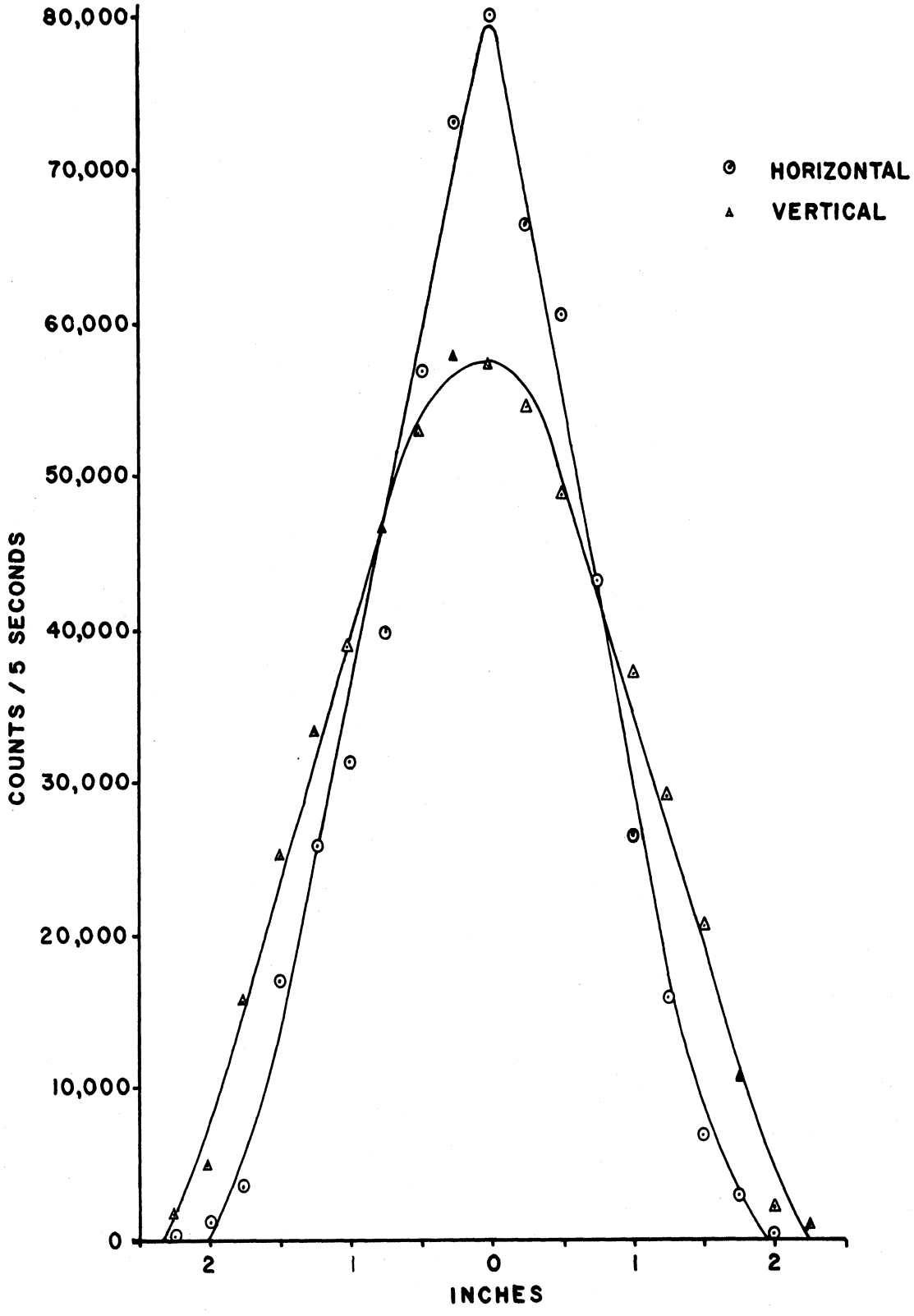

Figure 14. Measured horizontal and vertical beam profiles at the target position.

a rigid analyzer assembly could be designed and used. This is desirable because the shield cans surrounding the detectors must be massive. Moving these detectors in a 2:1 motion with rotating analyzer crystals would be a difficult mechanical problem. Second, since the analyzer assembly is fixed in space during an experimental run, the shielding tanks can be arranged close around the detectors. This helps to guarantee that the shielding arrangement remains fixed, so only very slow changes in the background count rate would be expected.

Third, no correction to the scattering data for the efficiency of the BF_3 detectors is needed. In fact, the only required correction to the count rate is the variation of the thin fission monitor efficiency with energy; this correction can be more accurately calculated than the variation of the BF_3 detector efficiency with energy. Fourth, a correction for the finite size of the analyzer crystals is not needed. If the analyzer crystals were rotated to do an energy analysis of the scattered neutrons, this correction would be needed because the analyzer crystals are not quite long enough to intercept all of the neutron beam from the analyzer collimators as the crystals rotate to small Bragg angles. And fifth, it would be very difficult to design independent analyzer systems in which the crystals would rotate exactly together; this would be necessary to keep the energy of analysis the same for each of the analyzer systems. All of these problems are eliminated by using fixed analyzer energy, and varying the incident energy.

Calibration and performance of the spectrometer

1. Source Spectrum

The initial experimental study made with the spectrometer was the measurement of the thermal neutron leakage spectrum from beam port "A." Information from this experiment is used in calculations of the available neutron intensity as a function of energy, the magnitude of second order contamination of the beam incident on the targets studied in inelastic scattering experiments, and for determination of a Maxwellian temperature to characterize the spectrum. Direct measurement of the leakage spectrum can be carried out using either a crystal spectrometer or a mechanical chopper. Both of these instruments require that detector efficiency corrections must be applied to the observed data. For a mechanical chopper, an instrumental transmission function which varies with energy must be calculated; analogously calculation of the crystal reflectivity as a function of order and energy must be made for the crystal spectrometer.

To measure the leakage spectrum, the Bragg reflected beam intensity is measured.[1] The count rate measured by the fission monitor is related to the flux incident on the monochromator crystal:

---

[1]The reactor core and the source end of the beam tube are separated by a three inch thickness of graphite reflector and a one inch water gap. The relative orientation of the beam port and the reactor is shown in Figure 11.

$$\text{Count Rate} = \text{C.R.}(\theta) = \int \phi(\theta)\, P(\theta)\, \epsilon(\theta)\, d\theta$$

where $\phi(\theta)$ is the source flux per unit Bragg angle per unit time

$P(\theta)$ is the crystal transmission probability

$\epsilon(\theta)$ is the fission chamber efficiency

and where the (constant) effect of the collimator has been ignored. The crystal transmission function is sharply peaked in angle. Over very small angular ranges, both the flux and the efficiency functions can be considered to be constant, or

$$\text{C.R.}(\theta_0) = \phi(\theta_0)\, \epsilon(\theta_0) \int P(\theta)\, d\theta = \phi(\theta_0)\, \epsilon(\theta_0)\, R(\theta_0)$$

where $R(\theta_0)$ is the integrated reflectivity at θ_0. Taking into account that the crystals will Bragg scatter neutrons of all orders from the incident beam:

$$\text{C.R.}(\theta_0) = \sum_{n=1}^{\infty} \phi^n(\theta_0)\, \epsilon^n(\theta_0)\, R^n(\theta_0) \qquad \text{(III-1)}$$

After Bragg reflection, the beam passes through the fission monitor. A cadmium iris was centered over the inside face of the monitor to allow only the thermal neutrons within a 1.5 inch diameter circle to pass into the monitor. For an epicadmium background measurement at each angular position, a full sheet of cadmium was positioned over the inside face of the monitor.

Measurements were made over the energy range 0.025 to 0.293 ev. The count rate obtained by subtracting out the epicadmium neutron background is shown in Figure 15 for the energy range 0.025 to 0.16 ev. The signal to background ratio

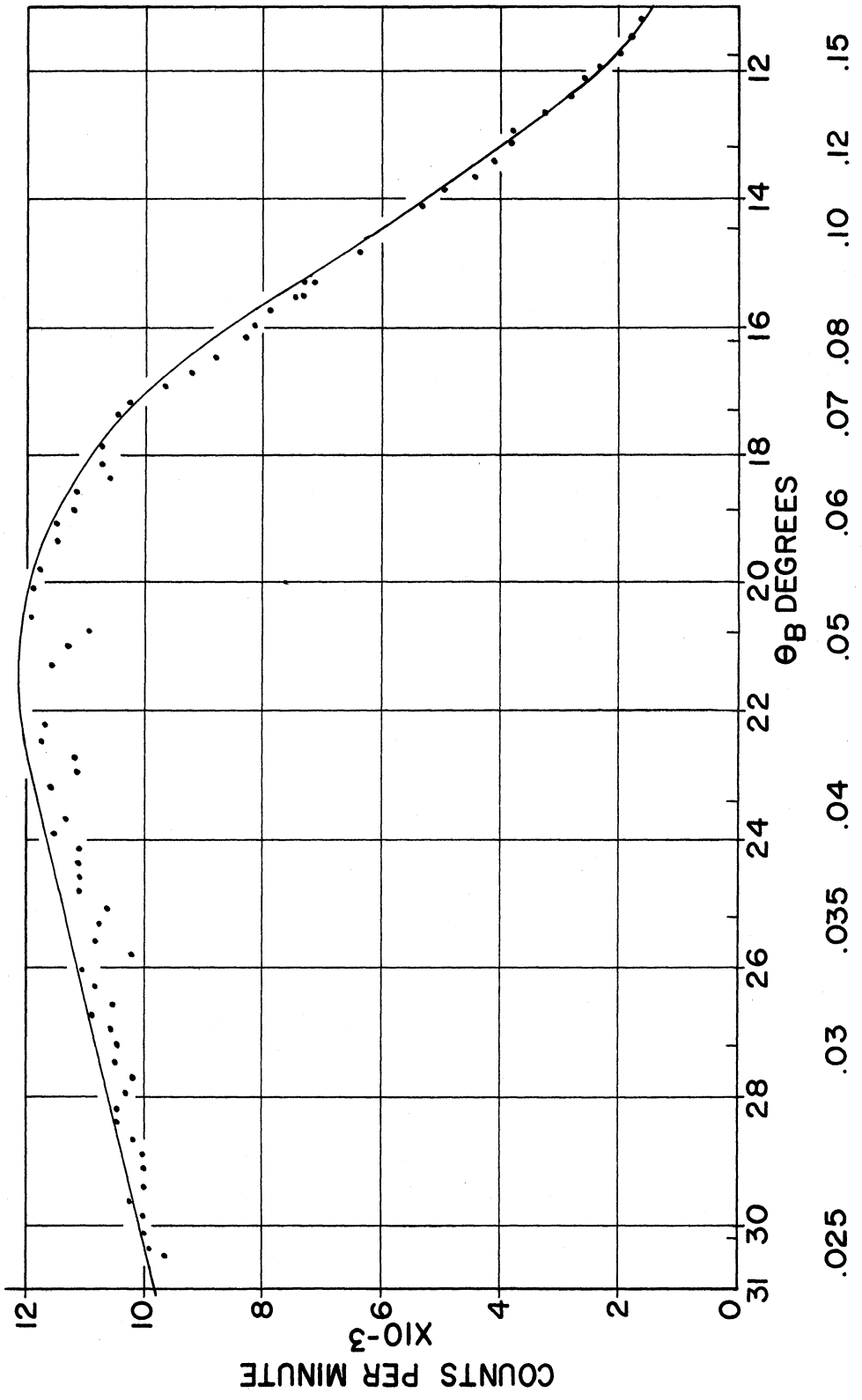

Figure 15. Measured neutron count rate for the energy range 0.025 to 0.16 ev.

varies from a minimum of 6.5 at 0.28 ev to 100 or more below 0.075 ev. The dips in the measured count are due to destructive interference from competing planes in the crystal. The smooth curve shown fitted to the measured points was used for computation of the thermal spectrum.

The calculated reflectivity $R(\theta)$ for the (200) planes of the copper crystal is shown in Figure 16 for first- and second-order reflection as a function of energy. These values were used in the spectrum calculations. Another set of reflectivity values are presented in Figure 17 for different copper crystal parameters. The first set (Figure 16) (n = 2 minutes, t_o = 1.5 inches) refers to the copper crystal after the ingot was divided into two semicylindrical crystals; the second set (Figure 17) refers to the crystal after each semicylinder was cut to provide three crystal plates, and the crystal surface was scored to increase the mosaic spread (see Chap. 3). The value of the crystal mosaic spread (η) was determined from single and double crystal rocking curves. The reflectivity calculation for a crystal used in reflection follows the expression given by Bacon (20)[1]:

---

[1]The definition of μ used differs from the definition in Reference (20). Here μ is defined as the total cross section minus the coherent scattering cross section, $\mu = N(\sigma_{TOT} - \sigma_{COH})$.

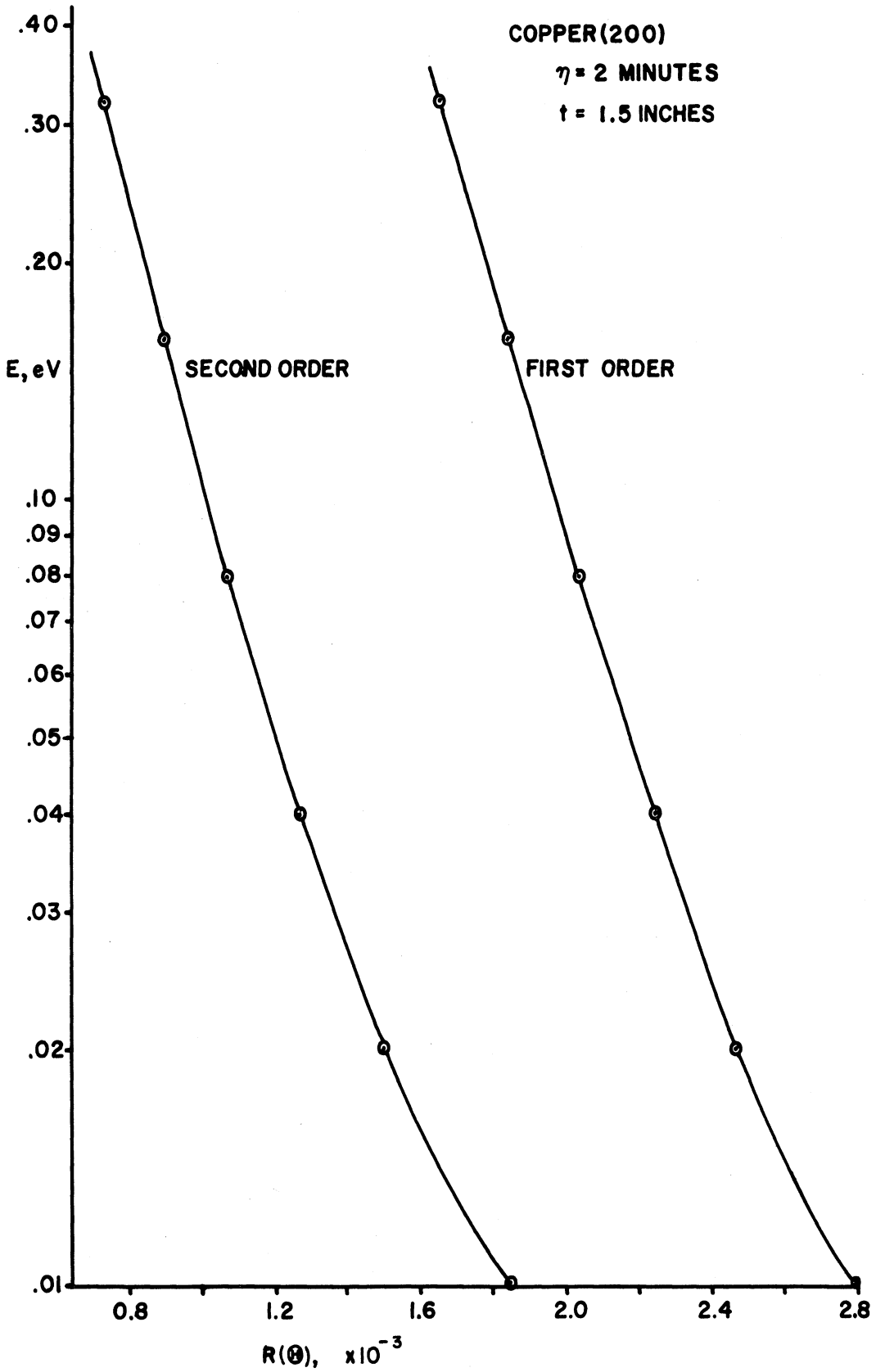

Figure 16. Calculated first and second order reflectivity for copper (200), η = 2 minutes, t_o = 1.5 inches.

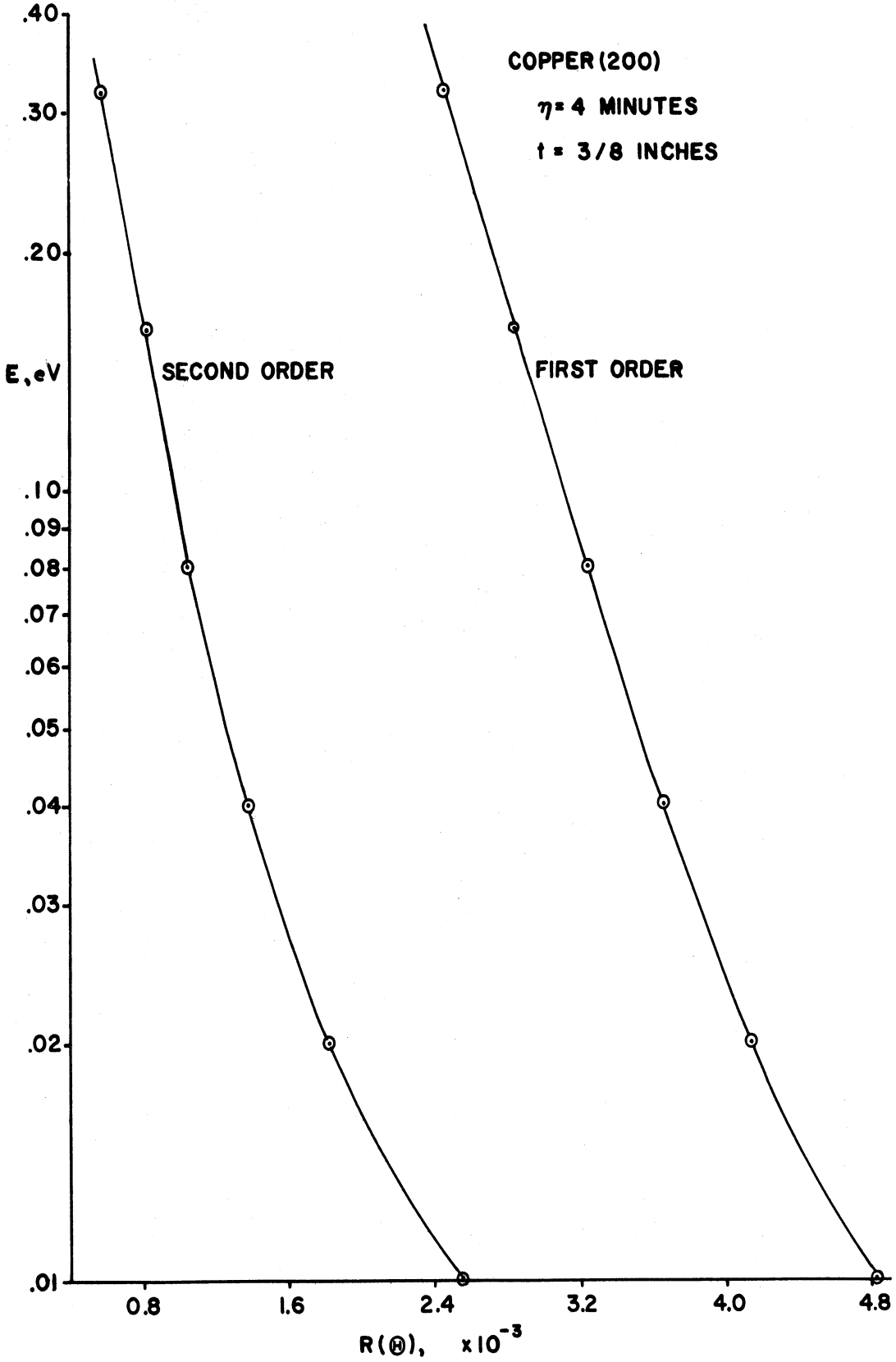

Figure 17. Calculated first and second order reflectivity for copper (200), η = 4 minutes, t_o = 3/8 inch.

$$R(\theta) = \int_{-\infty}^{\infty} \frac{a \, d\Delta}{(1+a) + (1+2a)^{1/2} \coth\left[A(1+2a)^{1/2}\right]} \qquad \text{(III-2)}$$

where $a = (Q/\mu)\left[\eta(2\pi)^{1/2}\right]^{-1} e^{-\Delta^2/2\eta^2}$

$Q = \lambda^3 N^2 F^2/\sin 2\theta$

λ = neutron wavelength

N = number of unit cells per unit volume

F = structure factor of a unit cell

μ = total cross section minus coherent scattering cross section

$\Delta = \theta - \theta_B$

$A = \mu t_o/\sin\theta$

t_o = crystal thickness

For these calculations, the following values were used for the copper crystal:

$t_o = 3.8$ cm

$\mu(E) = .319\,(0.025/E(ev))^{1/2}$

$F^2(200) = 9.24 \times 10^{-24}\ cm^2 e^{-.155n^2}$

$N^2 = 4.50 \times 10^{44}\ cm^{-b}$

$\eta = 2$ minutes $= 5.82 \times 10^{-4}$ radians

The efficiency of the monitor is shown in Figure 30. This curve is the product of the cross section and thickness of the U-235 plating in the fission monitor.

The observed count rate at a high energy (0.28 ev) was used to begin the order correction to the raw data.

Assuming that the spectrum above 0.28 ev varies as 1/E and that only first- and second-order contributions are important, the first-order count rate at 0.28 ev can be computed.

Define:

Observed Count Rate at θ = C.R. (0)

First-Order Count Rate = C.R. (1)

Second-Order Count Rate = C.R. (2)

First-Order Reflectivity, Efficiency: $R'(\theta)$, $\epsilon'(\theta)$

Second-Order Reflectivity, Efficiency: $R^2(\theta)$, $\epsilon^2(\theta)$

First-and Second-Order Flux: $\phi'(E)$, $\phi^2(E)$

First-Order Jacobian: $\left[dE'/d\theta\right] = 2E' \cot\theta$

Second-Order Jacobian: $\left[dE^2/d\theta\right] = 8E' \cot\theta$

Then, following the results of equation (III-1),

C.R. (0) = C.R. (1) + C.R. (2)

$$= \phi'(E) R'(\theta) \epsilon'(\theta) \frac{dE'}{d\theta} + \phi^2(E) R^2(\theta) \epsilon^2(\theta) \frac{dE^2}{d\theta} \qquad \text{(III-3)}$$

Now at .28 ev, $\phi^2(E) = \frac{\phi'(E)}{4}$

and at all energies $\frac{dE'}{d\theta} = 4 \frac{dE^2}{d\theta}$

For the 1/E region, therefore,

$$\text{C.R. (0)} = \phi'(E) 2E' \cot\theta \left[R'(\theta)\epsilon'(\theta) + R^2(\theta)\epsilon^2(\theta)\right] \qquad \text{(III-4)}$$

From the observed count rate at one megawatt reactor operation, equation (III-4) gives a flux at 0.28 ev of $1.77 \times 10^{+5}$ neutrons/cm^2-sec.

This value was used to compute the flux up to 1.12 ev; the 1/E flux relationship was used for this energy range. The resulting flux values were then used in equation (III-3) to correct the observed count values from 0.28 ev down to 0.07 ev. Below this energy the raw count was corrected using the corrected count for the energy range 0.10 to 0.28 ev.

The first-order flux as a function of Bragg angle, is then computed:

$$\phi^1(\theta) = \frac{\text{corrected count rate}}{R'(\theta)\ \epsilon'(\theta)} = \frac{C.R.(1)}{R^1(\theta)\ \epsilon^1(\theta)}$$

and the flux as a function of energy is

$$\phi^1(E) = \phi^1(\theta)\frac{d\theta}{dE^1} = \phi^1(\theta)\ \frac{1}{2E^1 \cot\theta}$$

The flux $\phi^1(\theta)$ is shown in Figure 18. The temperature T corresponding to this spectrum can be found if a Maxwell-Boltzmann distribution is assumed:

$$\phi_{MB}(\theta) = \phi_{MB}(E)\, 2E \cot\theta = K' E^2 e^{-E/k_B T} \cot\theta$$

Now,

$$\lambda = 2d \sin\theta = C' E^{-1/2}, \quad E = C \sin^{-2}\theta$$

Then

$$\phi_{MB}(\theta) = \frac{K \cos\theta \exp(-C \sin^{-2}\theta / k_B T)}{\sin^4\theta \sin\theta} = \frac{K \cos\theta \exp(-C \sin^{-2}\theta / k_B T)}{\sin^5\theta}$$

The peak of this distribution can be obtained by setting the derivitive equal to zero:

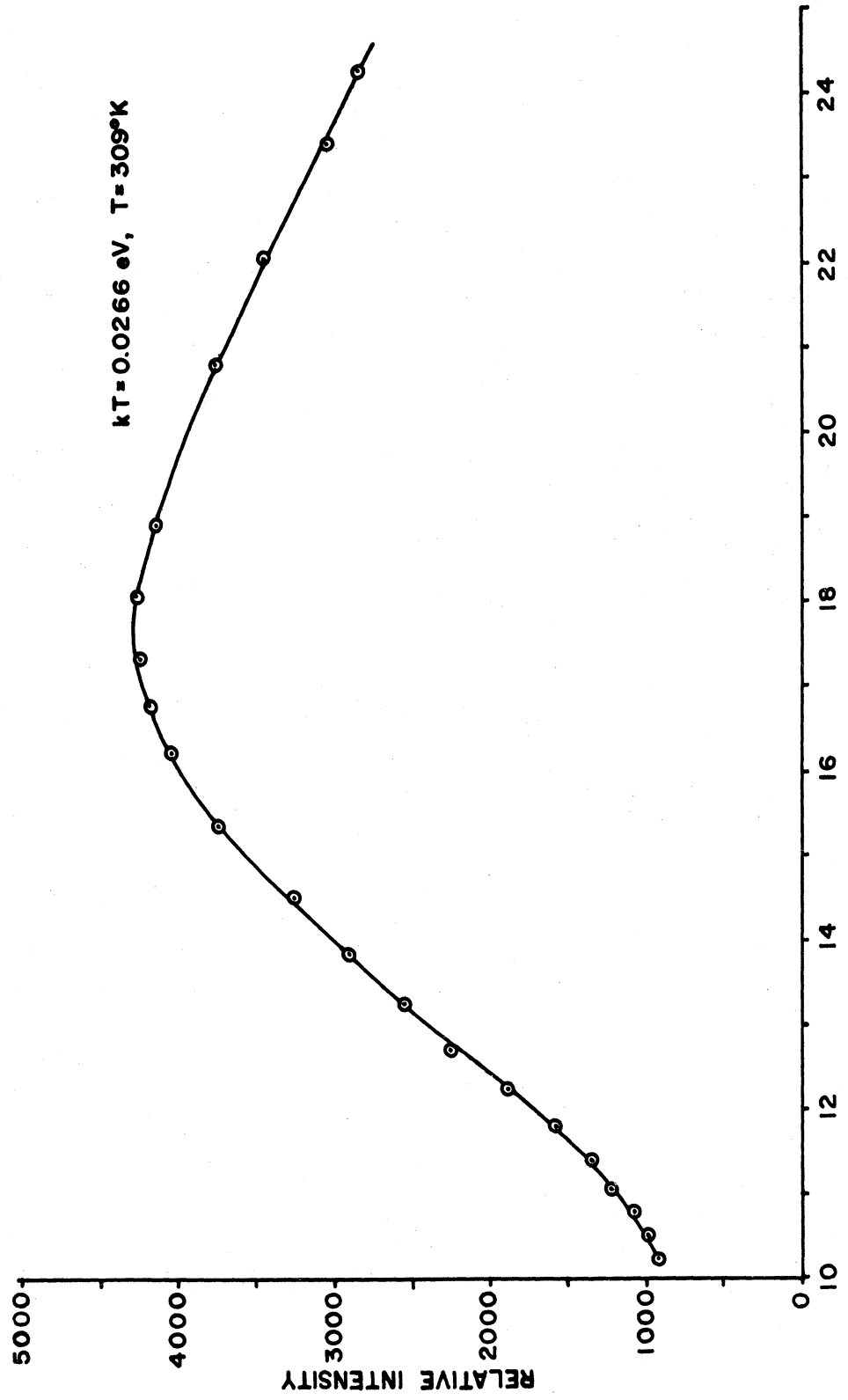

Figure 18. Measured reactor spectrum as a function of Bragg angle.

or $$\frac{2C\cot^2\theta}{k_B T \sin^2\theta} = 1 + 5\cot^2\theta$$

$$k_B T = \frac{2C}{\sin^2\theta(5+\tan^2\theta)} \qquad \text{(III-5)}$$

where

$$C = \left(\frac{.286}{2d}\right)^2 = \left(\frac{.286}{3.615}\right)^2$$

From Figure 18 the peak of the curve is seen to occur at $\theta = 17.6^\circ$. Then using (III-5):

$$kT = \frac{2(.286/3.615)^2}{(.0916)(5+0.10)} = 0.0266 \text{ ev}$$

Another method may be used to obtain the value of kT corresponding to the measured spectrum. It may be noted that, again assuming a Maxwell-Boltzmann distribution,

$$\phi = KE e^{-E/kT}, \quad \frac{\phi(E)}{E} = K e^{-E/kT}, \quad \ln\left[\frac{\phi(E)}{E}\right] = \ln K - \frac{E}{kT}$$

Therefore, a plot of $\ln(\phi(E)/E)$ versus E will have a slope of (-1/kT). This is shown in Figure 19. The slope of the straight line fitted to the points between 0.025 and 0.12 ev corresponds to the value kT = 0.0266 ev, which is equivalent to a Maxwellian temperature of 309°K. The above analysis of $\phi^1(\theta)$ corresponds to a spectrum temperature of 309°K. These values are considerably above the temperature of the pool water (301°K) when the reactor is operated at one megawatt.

Figure 20 shows the measured spectrum plotted as a function of energy. For comparison purposes, a Maxwell-

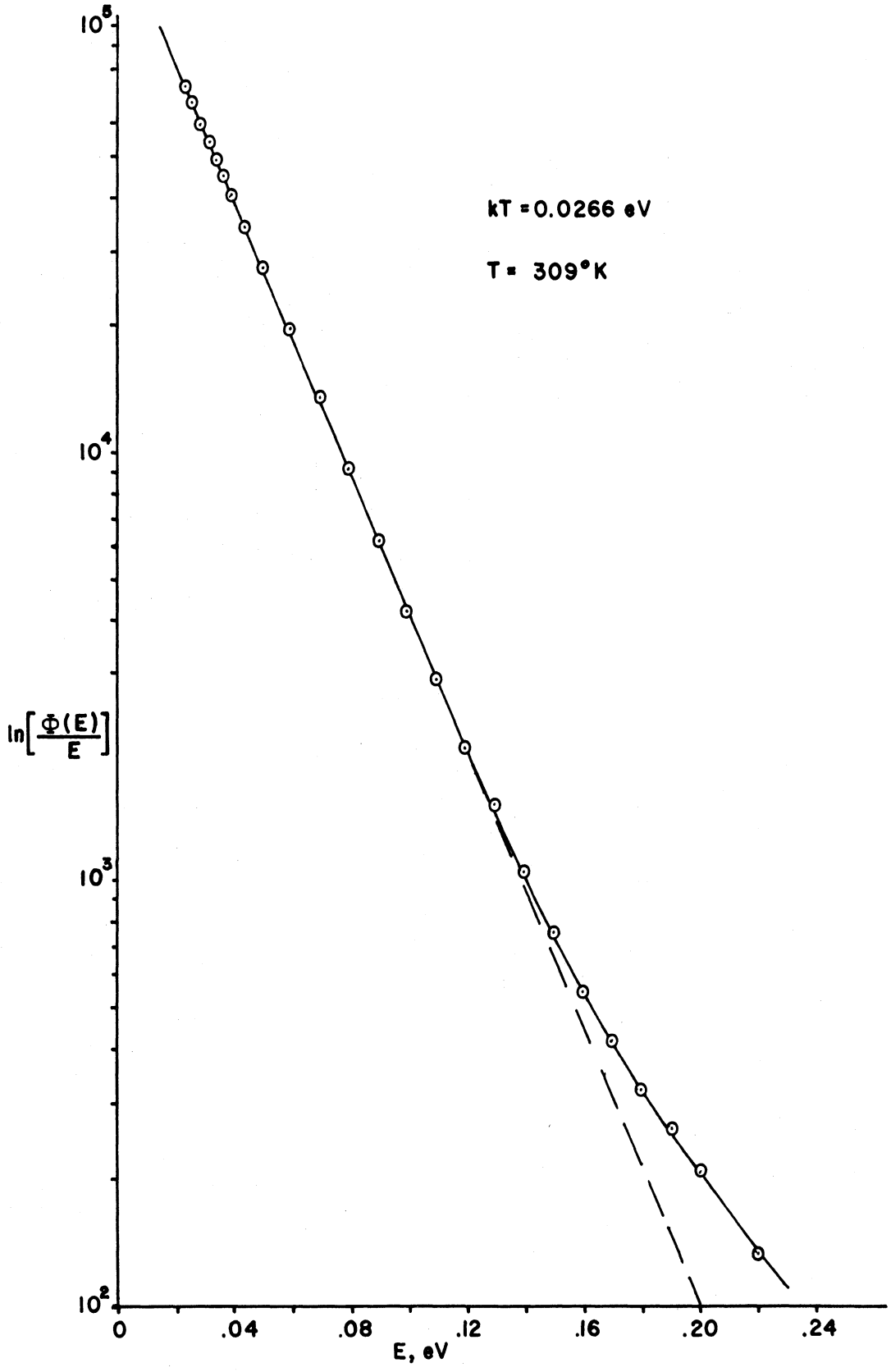

Figure 19. Determination of a characteristic temperature from the measured energy spectrum.

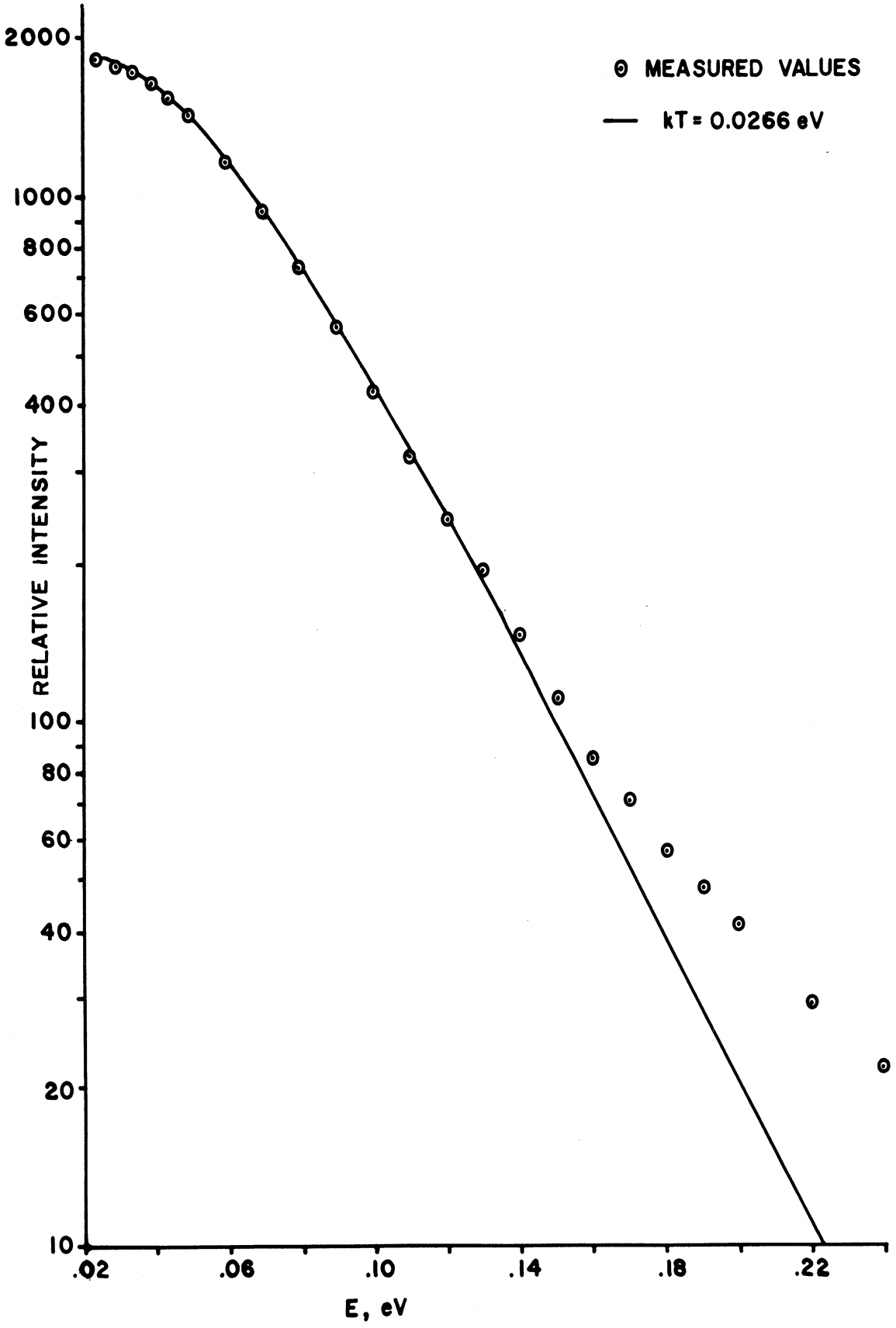

Figure 20. Measured reactor spectrum as a function of energy.

Boltzmann distribution corresponding to kT = 0.0266 ev is also shown. It will be noted that the 1/E contribution becomes important above 0.13 ev; it is equal to the Maxwell-Boltzmann contribution at E = 0.215 ev.

The percentage of the observed count rate at the monitor at any energy that is due to first-order neutrons is shown in Figure 21. From this curve, the magnitude of the correction to be applied to an observed monitor count for calculating the first-order component incident on a target used in a scattering experiment can be obtained.

Scattering experiments also require knowledge of the relative flux values at the target as a function of energy. The spectrum measured above is that which is incident on the monochromating crystal. This spectrum is modified after reflection off the copper crystal because of the variation of the crystal reflectivity with energy. Figure 22 gives the second-order contamination of the beam incident on a scattering target as a function of energy.

2. Energy calibration

A precise measurement of neutron energy versus Bragg arm position is made by measuring the angular distribution of the neutrons diffracted from a 3/4 inch thick plate of aluminum. The plate is essentially polycrystalline and presents planes of all possible orientation to the incident beam. The measured angular distribution is taken with a fixed main Bragg arm position. A scale and vernier mounted on the front face of the

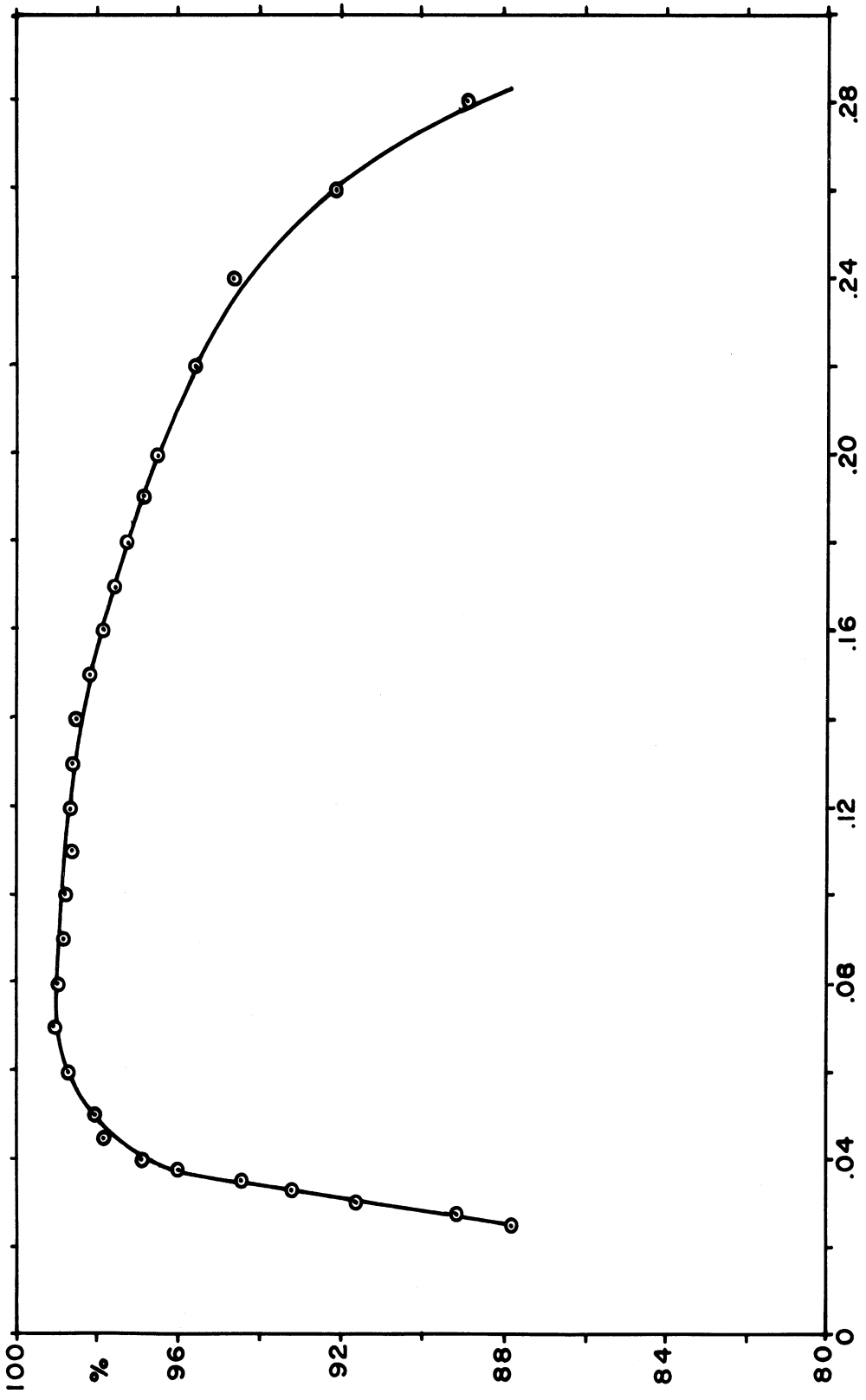

Figure 21. Percentage of the monitor count rate due to first order neutrons.

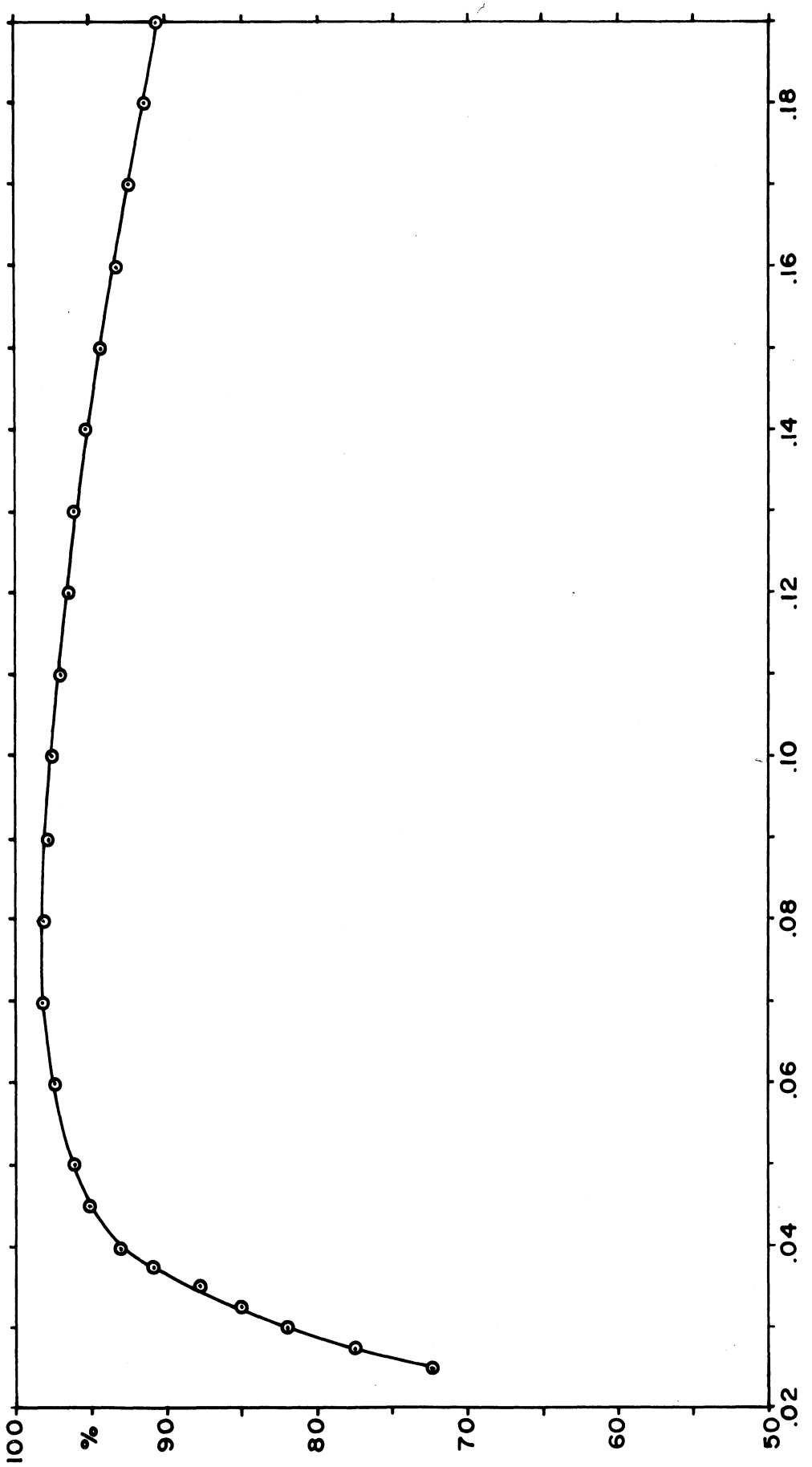

Figure 22. Percentage of first order neutrons in the experimental beam.

turret measures the Bragg arm position; this scale is calibrated in terms of energy by observing the angular positions in the angular distribution corresponding to the (111), (200), (220) and (311) aluminum diffraction peaks. Using the Bragg relationship, $n\lambda = 2d\sin\theta$, the value of λ (or E) corresponding to the fixed arm position is determined. A typical diffraction pattern is shown in Figure 23. This energy calibration is repeated for several Bragg arm positions to obtain an energy calibration curve for the spectrometer. In Figure 23 several second-order diffraction peaks can be seen and these can also be used to obtain an estimate of the second order contamination of the experimental beam.

Before the energy calibration data is taken, a geometric allignment of the beam at the target position is made. A 3/4 inch diameter BF_3 tube (effective diameter $\approx$ 1/4 inch) is mounted on a continuous screw drive to obtain profiles of the vertical and horizontal intensity at the target position. Vertical adjustment of the Bragg beam is permitted by the tilt adjustment of the monochromator crystals. Horizontal adjustment is obtained by use of the translation and rotation motions possible for each monochromator crystal. The position of the beam is adjusted for each monochromator separately. After the position of one monochromator crystal is accurately determined, it is tilted to remove its reflected beam from the target. The other monochromator crystal is then set, after which the first crystal is returned to its proper tilt position. A final

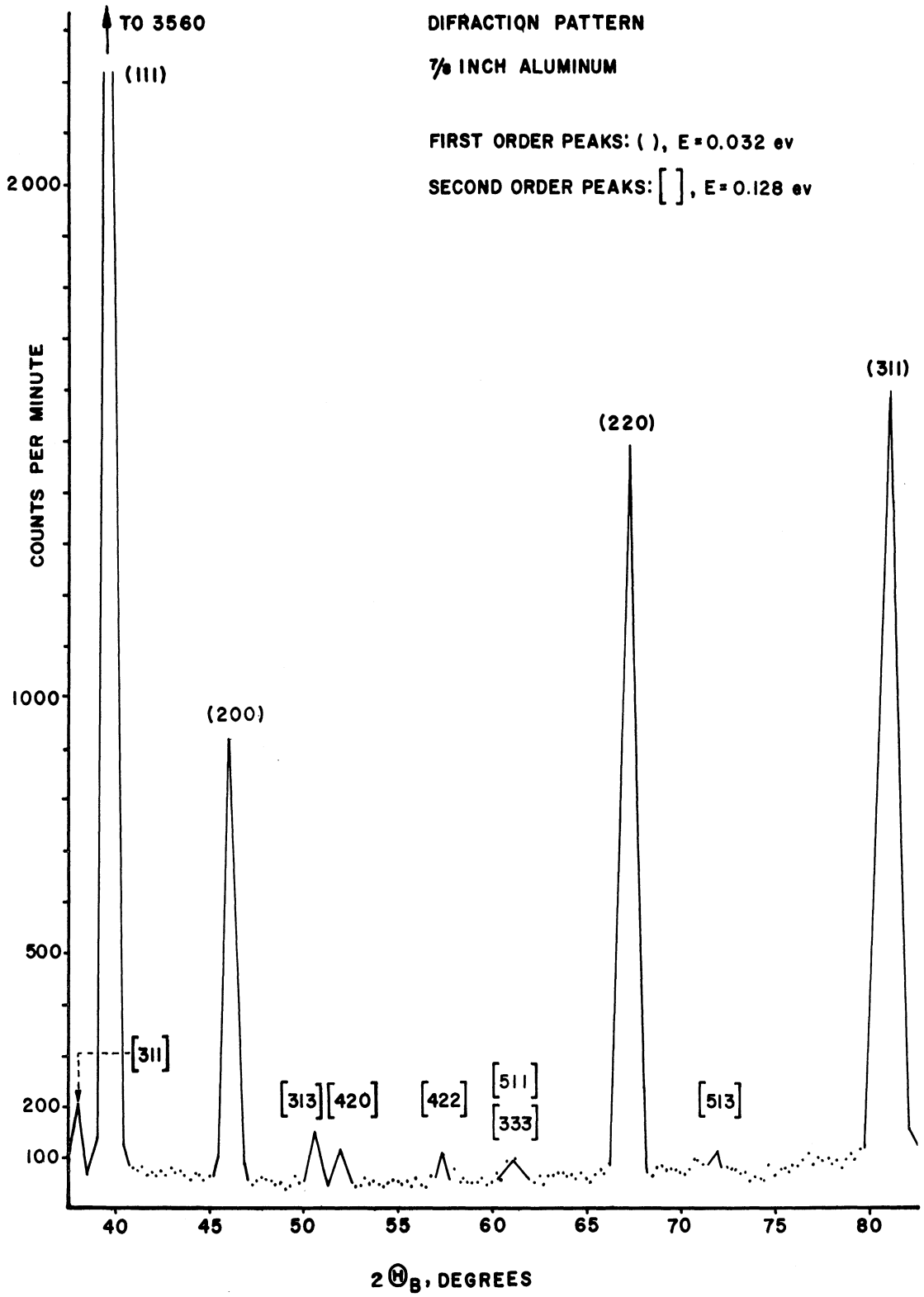

Figure 23. Aluminum diffraction curve used for energy calibration of the experimental beam.

intensity profile is taken at the target position to insure that the optimum adjustment has been obtained. Typical horizontal and vertical profiles are shown in Figure 14. Two secondary checks also are made. First, the energy content of the focused Bragg beam is remeasured by another aluminum diffraction pattern to guarantee that each monochromator crystal is providing the same energy neutrons in the experimental beam. Second, the position of the experimental beam is determined for several main Bragg arm positions to guarantee that the 2:1 motion is followed. Another method is used also to study the beam profile and beam position; a Polaroid camera, adapted to respond to thermal neutrons by Dr. A. Arrott of the Ford Scientific Laboratories, is used to photograph the experimental beam. The $B^{10}(n,\alpha)$ reaction is used in this neutron camera to produce light scintillations which are recorded by the 3000 speed Polaroid film. A typical photograph of the experimental beam can be made in fifteen seconds.

After the primary beam calibration is complete, the energy settings of the three analyzer systems must be set. To accurately select the analyzer energy, each of the three units is calibrated independently. This is done by inserting a 0.246 inch vanadium target; the vanadium scattering cross section is primarily elastic, incoherent and isotropic ($\sigma_{COH} \cong 0.03\,b$, $\sigma_{INC} \cong 5.1\,b$). For each analyzer a sweep of the incident energy is made to obtain a resolution curve. The peak of the curve corresponds to the energy setting of the analyzer. A typical calibration curve

for one of the analyzers is shown in Figure 24. If necessary, each of the analyzer crystals is then given a small final rotation to set each to the same energy. After the analyzers are correctly set, an "adder" network is used to combine the output signals from the three BF_3 detectors. Another sweep of the incident energy is made to determine the energy resolution of the composite system. After each inelastic scattering experiment, a repeat determination is made to recheck the system resolution and detector response. A typical composite resolution curve is shown in Figure 25.

3. Spectrometer resolution and intensity

The resolution of the triple axis crystal spectrometer is based on a compromise between intensity and resolution. The resolution is determined by the angular aperatures of the collimators and the mosaic properties of the crystals. After the desired compromise has been selected and the system design resolution determined, the apertures of the collimators are calculated to fix the horizontal and vertical angular divergences. Obtaining the desired crystal properties is not as simple. The crystal properties can be altered by various techniques, but this subject is not well understood.

The two semi-cylindrical copper crystals from the Semi-Elements Corporation gave single crystal rocking curves of nine minutes full width at half maximum (FWHM). This value is much less than the collimator widths of 25.9 and 25.0 minutes, so

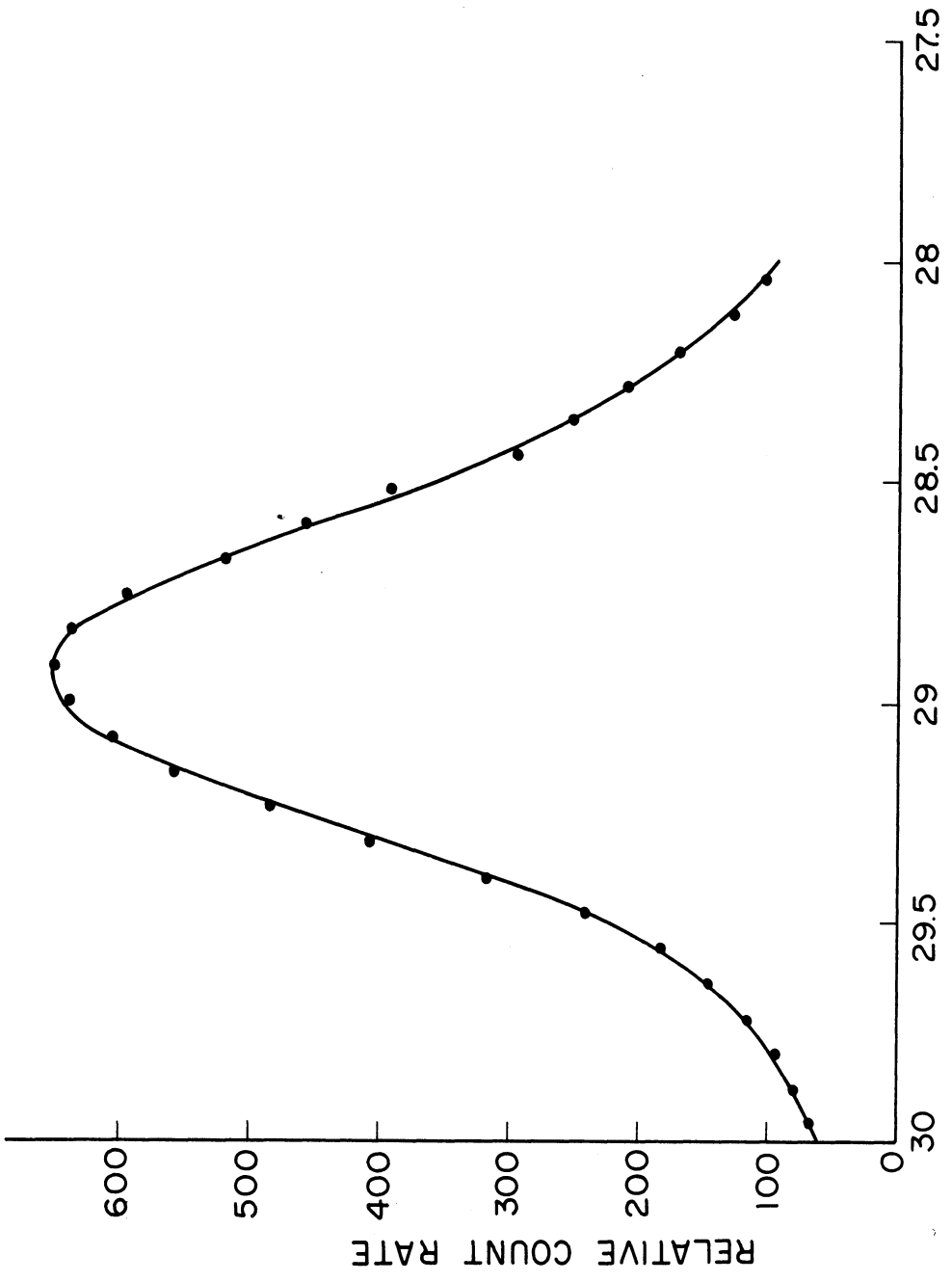

Figure 24. Spectrometer resolution curve for a single analyzer (horizontal unit).

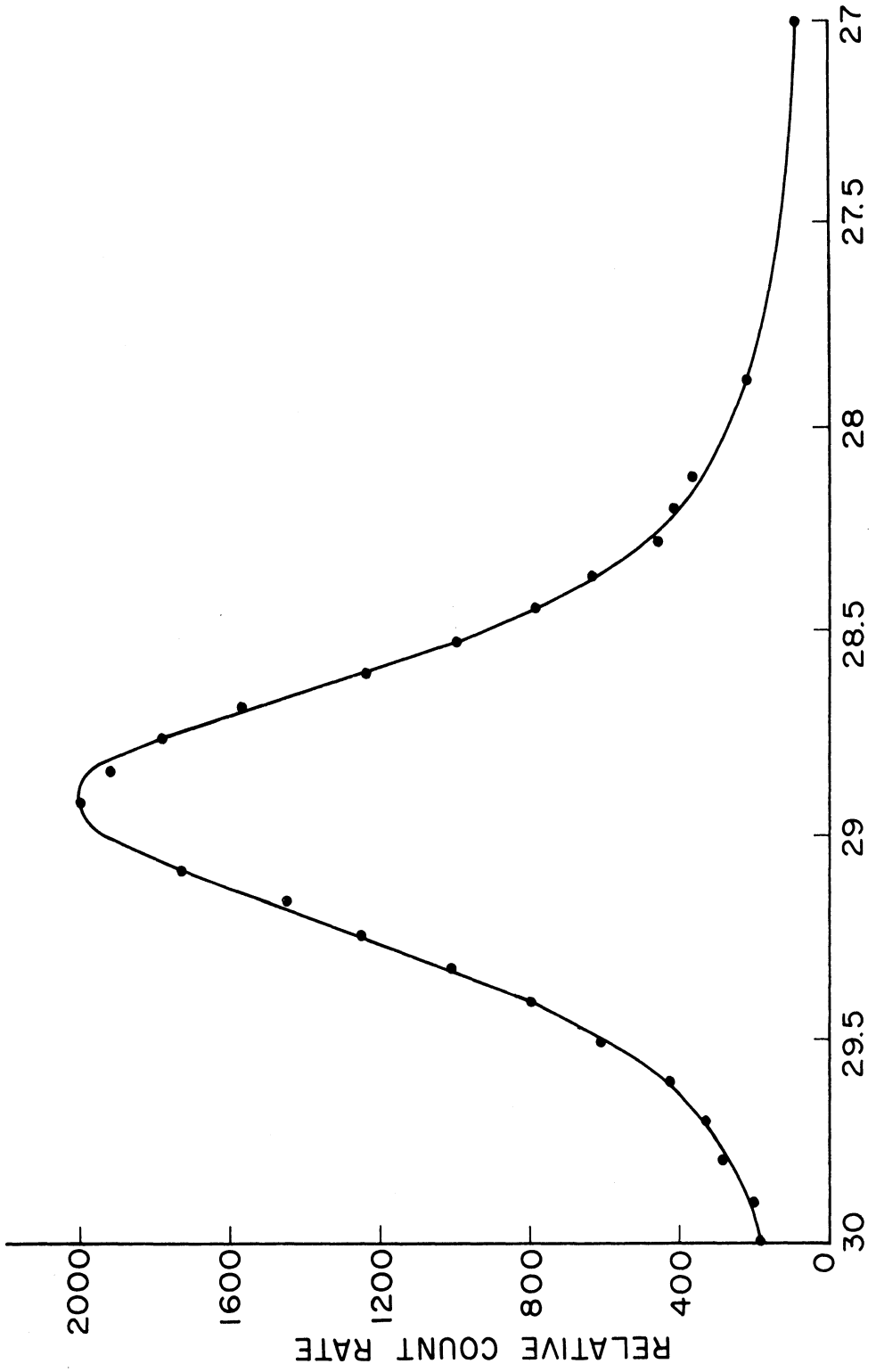

Figure 25. Spectrometer resolution curve for three analyzer systems.

that the resolution is almost completely determined by the collimators (see equation III-9). For values of the crystal full width at half maximum up to about 20 minutes, the calculated crystal integrated reflectivity varies almost linearly with the width. Therefore, if the crystal width can be increased, a large increase in intensity will result with only a small loss in resolution, i.e., the system is matched. Consequently, an attempt was made to increase the width of the single crystal rocking curves by surface treatment.

The count rate expected in a scattering experiment with the triple axis spectrometer can be calculated assuming gaussian functions for the collimator and crystal transmission probabilities. The collimator transmission probability is assumed to be:

$$P(\phi) = c\, e^{-\phi^2/2\alpha^2}$$

where ϕ is the angle measured from the collimator axis, α is related to the full width at half maximum (α') of the actual triangular distribution by:

$$\alpha' = \frac{s}{l} = \sqrt{8 \ln 2}\ \alpha$$

where s is the width and l is the length of the collimator slots. The crystal transmission probability is taken to be:

$$P(\Delta) = \frac{R\, e^{-\Delta^2/2\beta^2}}{\sqrt{2\pi}\ \beta}$$

where R is the integrated reflectivity given in equation III-2, and β is related to the mosaic parameter η by compar-

ing the measured FWHM (β') of the crystal distribution function with the distribution calculated using equation (III-2), noting that

$$\beta' = \sqrt{8 \ln 2}\ \beta$$

The detected count rate for scattering from an initial energy (corresponding to θ_0) to a final energy (θ_f) is:

$$C R(\theta_1, \theta_2, \alpha_0) = \int\!\!\int \Phi(\theta_0, \phi_1) P_1(\phi_1) \delta(\phi_1 + \theta_1 - \theta_0 - \Delta_1) \quad (x)$$
$$P_t(\alpha_0 - \phi_2, \theta_0, \theta_f) P_2(\phi_2) \delta(\phi_2 + \theta_2 - \theta_f - \Delta_2) P_2(\Delta_2) \epsilon(\theta_f) (x)$$
$$d(\theta_0)\, d\phi_1\, d\Delta_1\, d\theta_f\, d\phi_2\, d\Delta_2 \qquad \text{(III-6)}$$

where α_0 is the mean scattering angle and θ_1 and θ_2 are the monochromator and analyzer crystal settings. $\Phi(\theta_0, \phi_1)$ is the source flux impinging on the first collimator per unit Bragg angle and per unit collimator angle, $P_t(\alpha_0 - \phi_2, \theta_0, \theta_f)$ is the target scattering probability, $\epsilon(\theta_f)$ is the efficiency of the detector at the final scattering energy corresponding to θ_f. The angles are shown in Figure 26.

For a resolution measurement using a vanadium target, whose cross section is assumed purely elastic, incoherent and isotropic, equation (III-6) can be simplified. The source flux is slowly varying in angle and is constant in ϕ_1; equation (III-6) becomes:

$$\text{C.R.} \approx \Phi(\bar{\theta}_0) P_t(\alpha_0, \bar{\theta}_0) \epsilon(\bar{\theta}_0) \int\!\!\int\!\!\int\!\!\int P_1(\phi_1) P_1(\Delta_1) P_2(\phi_2) P_2(\Delta_2)\, d\phi_1\, d\Delta_1\, d\phi_2\, d\Delta_2 \qquad \text{(III-7)}$$

where $\bar{\theta}_0$ in the mean Bragg angle.

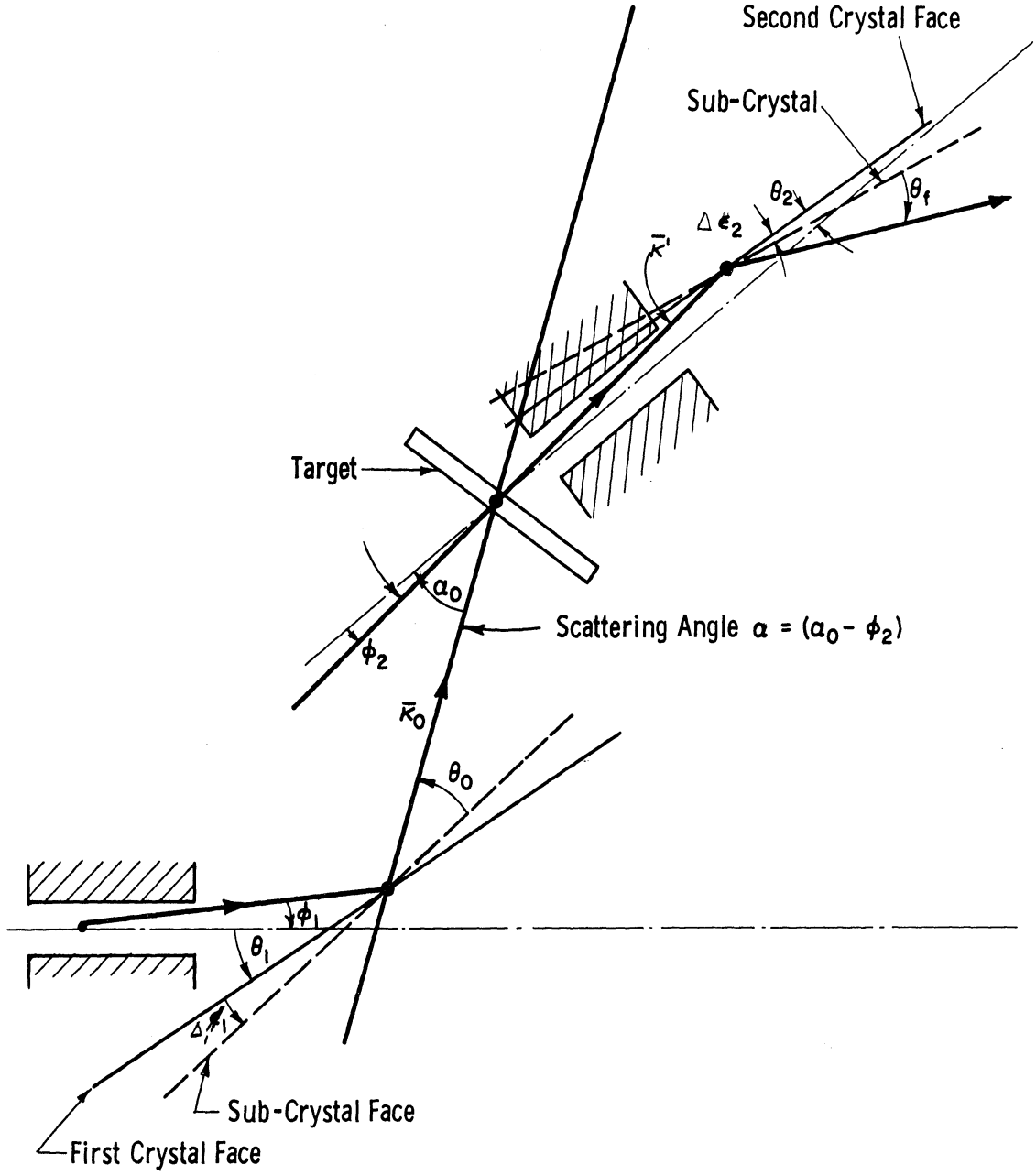

Figure 26. Angle relationships for the analysis of the triple axis crystal spectrometer count rate.

The angles are related by the Bragg conditions. When (III-7) is integrated after substituting the collimator and crystal transmission functions, the result is: (21)

$$C.R. = \frac{(const.)\, R_1(\theta_0)\, R_2(\theta_0)}{(\alpha_1^2+\alpha_2^2+\beta_1^2+\beta_2^2)^{1/2}} \exp - \left[\theta^2/2(\alpha_1^2+\alpha_2^2+\beta_1^2+\beta_2^2)\right] \tag{III-8}$$

where $R_1(\theta_0)$, $R_2(\theta_0)$ refer to the integrated reflectivity for the monochromator and analyzer crystal, respectively; $\theta = \theta_1 - \theta_2$, where θ_1 and θ_2 are the monochromator and analyzer crystal settings, respectively. Equation (III-8) expresses the angular uncertainty for a target with a purely elastic scattering cross section. The FWHM of the distribution, obtained when the monochromator crystal is varied, is:

$$FWHM = \left[\alpha_1^2+\alpha_2^2+\beta_1^2+\beta_2^2\right]^{1/2}\left[8\ln 2\right]^{1/2} \tag{III-9}$$

The calculated change in count rate and resolution as a function of the crystal mosaic spread for the triple axis spectrometer is shown in Table 5. The calculated change in integrated reflectivity as a function of crystal thickness for β = 17 minutes, E = 0.04 ev, is shown in Table 6. This shows that for copper crystals with this mosaic, most of the neutrons are reflected near the surface.

Previous observations on the change in crystal mosaic spread as the result of surface treatment have been reported by Sturm (22) for a lithium fluoride crystal. His results are

TABLE 5

CALCULATED SPECTROMETER RELATIVE COUNT RATE AND RESOLUTION AS A FUNCTION OF CRYSTAL FULL WIDTH AT HALF MAXIMUM

F.W.H.M.,* minutes	Relative Count Rate	Relative Resolution
9	1.00	1.00
12	2.16	1.04
16	3.60	1.11
20	5.33	1.17

*F.W.H.M., the full width at half maximum.

TABLE 6

CALCULATED CHANGE IN COPPER (200) INTEGRATED REFLECTIVITY AS A FUNCTION OF CRYSTAL THICKNESS FOR β =17 MINUTES, E=0.04 ev

Thickness, inches	Percentage of Infinite Thickness Reflectivity
.030	50
.078	75
.176	90
.250	98
.375	100

summarized in Table 7. Because a relatively large collimator angular divergence was used in Sturm's experiments, no quantitative conclusions could be drawn about the change in the value of the crystal mosaic spread with the various surface treatments. In all cases the rocking curve measured 22 $\pm$ 1 minutes. Compton and Allison (23) observed an increase in the mosaic spread of a calcite crystal as a function of time after cleavage of a fresh face, apparently due to a change in the

crystal surface. Also, an increase in the mosaic spread of an aluminum crystal after a 0.6 inch hole was drilled in the piece, was observed by Clayton and Heaton (24). This observed increase vanished after the surface of the crystal was etched.

TABLE 7

MEASURED VARIATION OF REFLECTIVITY WITH CRYSTAL SURFACE PROPERTIES FOR LiF (100), (22)

Surface	Relative Measured Reflectivity
Smooth cleavage face	1.00
Surface ground	1.65
Surface polished	2.34
Surface roughened with coarse abrasive	2.36

Following these observations and calculations, the two copper semi-cylinder crystals were cut on a bandsaw to provide six crystal plates approximately 3/8 inch thick, with the flat surfaces parallel to the (200) planes. Rocking curves were obtained before and after cutting, and again after various surface treatments were applied to the faces of the crystals. The intensity obtained in the triple axis spectrometer was also correlated with the crystal treatment. The surface treatments investigated were:

1. Surface milled flat with 3/4" tool
2. Milled surface polished on a belt sander
3. Surface scored with lines at 0.005 and 0.010 inch spacing, approximately 0.005 inches deep.

The monochromatic beam intensity as measured by the beam monitor

for the various surface treatments is shown in Table 8. Table 9 lists the overall spectrometer change in resolution and intensity observed with the various crystals installed in either the monochromator or analyzer crystal position.

TABLE 8

MEASURED MONITOR BEAM INTENSITY AT 0.049 ev

Crystal	Neutrons/Minute, x 10^7	Percentage Intensity Increase
Original	2.94	0
After cutting on band saw	3.68	25
After grinding	2.74	-7
After light milling	3.82	30
After heavy milling	4.20	39
After scoring, .010" spacing	5.08	73
After scoring, .005" spacing	6.08	106

The values reported in Table 9 can be used to derive an approximate value of the crystal mosaic spread in two independent ways, and this can then be compared to the value measured from crystal rocking curves. First, starting with System II, with $\beta_1 = \beta_2 = 9$ minutes, the collimator contribution to the resolution measurement can be isolated (equation III-9):

$$\left(\alpha_1^2 + \alpha_2^2 + \beta_1^2 + \beta_2^2\right)^{1/2} = 36.0 \text{ minutes}$$

or

$$\alpha_1^2 + \alpha_2^2 = 1134$$

Using System III in Table 9, a value for the scored monochromator (crystal face #1) can be estimated:

$$(39.6)^2 = 1134 + \beta_1^2 + 81 = 1215 + \beta_1^2 = 1565, \quad \beta_1 = 18.7 \text{ minutes.}$$

TABLE 9

SPECTROMETER RESOLUTION AND INTENSITY MEASUREMENTS FOR VARIOUS CRYSTAL SURFACE TREATMENTS

System*	FWHM, min.	Relative Resolution	Relative Monitor Intensity	BF_3 Intensity Counts/min.	Relative Spectrometer Intensity
I Original	35.5	1.00	1.00	4.65	1.00
II Polished M, Original A	36.0	1.01	0.94	4.65	1.00
III Scored M Original A	39.6	1.12	1.62	8.10	1.74
IV Scored M Scored A	43.8	1.24	1.62	14.25	3.06

*M refers to monochromator position, A to analyzer position.

From System IV, the mosaic value of the scored analyzer crystal (crystal face #3) is:

$$(43.8)^2 = 1134 + 350 + \beta_2^2 = 1484 + \beta_2^2 = 1920, \beta_2 = 20.9 \text{ minutes}$$

Second, using the observed intensity increase from System II to System III, 1.74, and using the dependence of the count rate on reflectivity given in equation (III-8):

$$CR = \frac{R_1(\theta)\, R_2(\theta)}{\left[\alpha_1^2 - \alpha_2^2 - \beta_1^2 - \beta_2^2\right]^{1/2}}$$ we calculate, for $R_2(\theta)$ fixed,

$$\frac{CR(II)}{CR(I)} = \frac{R_1^{II}[FWHM^{I}]}{R_1^{I}[FWHM^{II}]} = \frac{R_1^{II}(36.0)}{R_1^{I}(39.6)} = 1.74$$

$$\frac{R_1^{II}}{R_1^{I}} = 1.74\left(\frac{39.6}{36.0}\right) = 1.91$$

The scoring of the monochromator produced a reflectivity increase of 1.91; since the reflectivity is almost linearly proportional to the mosaic spread, this indicates a mosaic increase to at least β_1 = 17.2 minutes.

From System III to System IV, the observed intensity increase was 1.75; using the same analysis as above, the reflectivity increase for the scored analyzer crystal was 1.95, indicating a mosaic value of at least 17.6 minutes for β_2.

Four crystal rocking curves were obtained for different small surface positions on the monochromator crystal, β_1. The four surface areas, each about 3/8" x 3/4", were evenly spaced along the surface of the seven inch long crystal. The mosaic spread values derived from these curves are 17.0, 14.8, 21.0 and 9.4 minutes. This data indicates that the surface treatment is not uniform; the experimental values obtained in the spectrometer with a large beam covering most of the surface of the crystal are average values for the crystals.

The assumption of the Gaussian approximations for the crystal and collimator transmission functions can be crudely tested by observing the shape of the measured resolution curve. The assumptions appear to be valid. After the inelastic vanadium component is removed, the resulting resolution data is fit very well by a Gaussian. A Gaussian curve calculated for the same full width at half maximum is shown with the data in Figure 27.

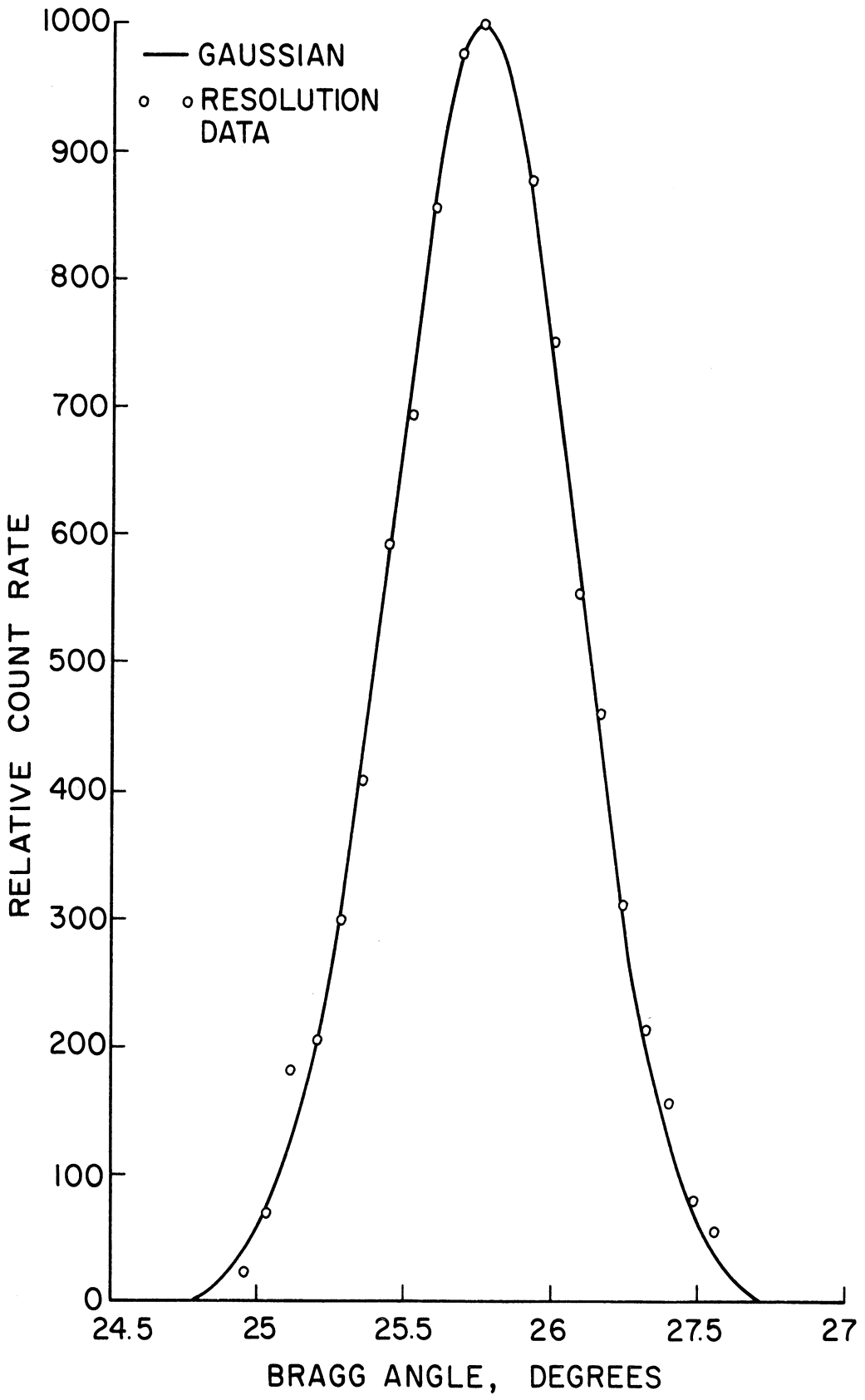

Figure 27. Comparison of vanadium resolution data with a calculated Gaussian.

Absolute intensity measurements were made at various locations along the neutron beam path, from the center of the reactor to the analyzer detectors. Table 10 lists the observed intensities and the total beam current measurements corresponding to 0.246 inch vanadium elastic scattering at two megawatt reactor power. The reactor measurements were made by one mil gold foil activation; the reactor face - beam port entrance measurement is for a flux neither isotropic nor unidirectional.

TABLE 10

OBSERVED INTENSITY AND BEAM CURRENT MEASUREMENTS, 0.246 INCH VANADIUM TARGET, 2 MEGAWATT REACTOR POWER

Location	Intensity, n/cm^2-sec	Total Beam Current, n/sec
Center of core	2.3×10^{13}	-
Between graphite reflector and "A" port	1.3×10^{13}	-
One inch inside "A" port	4×10^{12}	-
Target position (0.063 ev)	-	9×10^5
Target position (0.027 ev)	-	7.3×10^5
BF_3 detector (0.027 ev)	-	14

It can be accurately related to the collimator exit current only by a detailed diffusion analysis at the source plane (25). The total attenuation of the neutron beam in the spectrometer system

can be estimated within a factor of four or less by careful evaluation of equation (III-6).

4. Signal to background ratio

The background count rate for each of the three BF_3 detectors with the reactor shut down is about 0.25 counts per minute. When the reactor is operated at two megawatts, the background per detector is about 5 counts per minute. For a typical polyethylene scattering experiment, the signal to background ratio varies from about 160 at the elastic peak to 2.5 at an energy transfer of 0.065 ev.

The BF_3 detector background count is due to high energy neutrons which pass through the boron carbide and cadmium shields around the detector, or thermal neutrons which enter the front face of the detector. A cadmium canopy completely encloses the neutron beam path from analyzer collimator to detector shield can; this eliminates the thermal neutron component of the background. To reduce the fast neutron background, materials with high hydrogen content are used to slow down the fast neutrons. The detectors are surrounded on the sides and top by water filled shield tanks; high density masonite is used below the detectors. This shielding material below the detectors is very important. A large open volume is necessary below the turret to allow motion of the main Bragg arm; fast neutron leakage from this source is appreciable. When a two inch thick piece of masonite was attached to the bottom of the one inch thick aluminum support plate, between the plate and the top of the two support rails, the background count was reduced by 75%.

Target preparation

The polyethylene targets used in these experiments were high crystallinity thin films (29.5 and 16.1 mils) prepared from Phillips Petroleum Company Marlex 6050. The crystallinity was determined at the Dow Chemical Company using x-ray diffraction following the method of Aggarwal and Tilley (26). The percentage crystallinity refers to the weight percentage of the total polymer which is sufficiently ordered to give an x-ray diffraction pattern characteristic of crystalline materials, rather than a diffuse halo characteristic of amorphous or disordered regions. The Dow measurements for a series of polyethylene samples are shown in Table 11.

TABLE 11

PERCENTAGE ABSOLUTE CRYSTALLINITY OF VARIOUS POLYETHYLENES AS DETERMINED BY X-RAY DIFFRACTION

Sample		Percentage Absolute Crystallinity
Marlex 6050	16.1 mils	90.7
Marlex 6050	29.5 mils	89.7
Marlex 6002	20 mils	87.2
Alathon 7511	17 mils	86.4
Resinol Type F	15 mils	86.3
Alathon 7011	30 mils	85.7
Super Dylan 6004	10 mils	84.0
Alathon 31	20 mils	77.8
Resinol Type A	15 mils	75.5
Alathon PE 683	5 mils	73.0
Visqueen	15 mils	72.2
Commercial bag material	5 mils	71.3

The thicker Marlex 6050 polyethylene film (0.0295 inches) was supplied to us by the courtesy of Dr. H. R. Danner of the University of Missouri. This piece of polyethylene was prepared at the same time as the piece used in his cold neutron investigations at Brookhaven National Laboratory (1). Both pieces were prepared from pellets of Phillips Marlex 6050 pressed at 30 tons at 138°C for six minutes and then slowly cooled to ambient temperature. The catalyst residues were removed by de-ashing. The 16.1 mil target was loaned to us by Dr. W. Moore of Rensselaer Polytechnic Institute.

For the room temperature experiments, the sheet of polyethylene under study was positioned against a 20 mil thick sheet of cadmium. The two pieces were mounted inside a picture frame type target holder. This frame was designed to permit slight stretching of the polyethylene film to provide a smooth, flat surface. The target surface was 5-1/2 inches by 5-1/2 inches to completely intercept the experimental beam. All the aluminum support pieces around the target were covered with cadmium to prevent any possible scattering from the frame itself. This target holder is shown in Figure 28.

For the low temperature experiments, a more elaborate picture frame target holder was designed. The sides and bottom of the frame are tubular to allow liquid nitrogen to cool these three edges of the target; a reservoir above the target cools the fourth edge. This target assembly is contained inside an aluminum cryostat. The walls of the cryostat were turned down to 0.040 inches at the neutron beam position. A vacuum pump

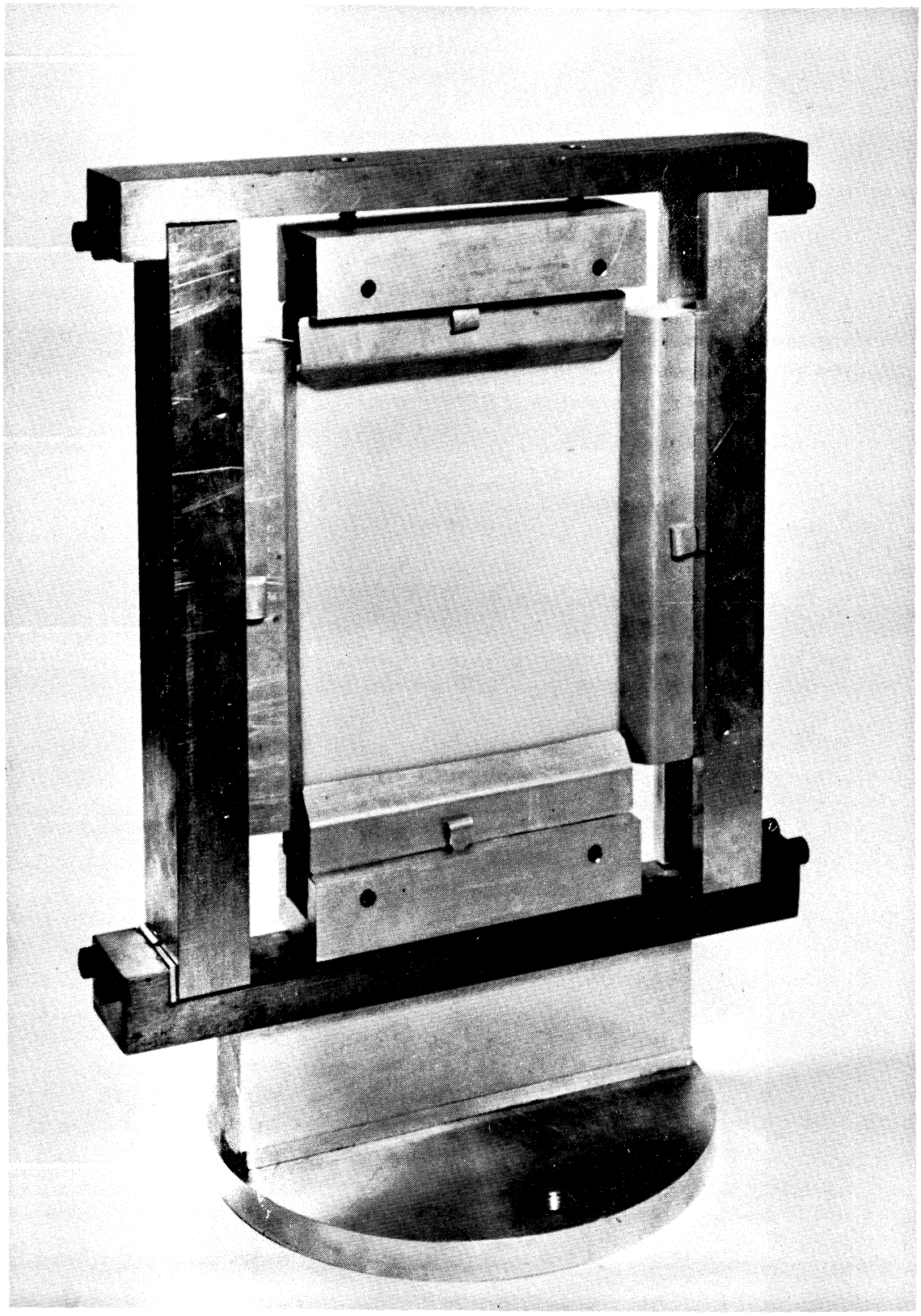

Figure 28. Polyethylene target assembly.

maintains a 20 micron vacuum in the cryostat to prevent water vapor condensation on the target surface. The cryostat and target frame assembly are shown in Figure 29.

The temperature at the edge and the center of the target was measured using a copper-constantan thermocouple. The temperature at the edge of the target was 87°K. With the 0.0295 inch polyethylene target and the 0.020 inch cadmium plate in the picture frame assembly, the temperature at the center of the target was 130°K. An estimation of the average target temperature was made assuming a cosine temperature distribution and using the neutron beam profile curves, Figure 14. This gives an effective average target temperature of 125°K $\pm$ 5°K. To lower the target temperature by reducing radiation losses from the target surface and by increasing conduction to the edges of the target, a thin aluminum foil was placed over the target surfaces and clamped tightly into the frame assembly. With a four mil thick aluminum foil, the temperature at the center of the target was lowered to 95°K. Addition of a five mil aluminum foil around the whole frame assembly lowered the temperature to 90°K.

Order contamination

The copper crystals used in the monochromator position and in the analyzer assemblies will reflect neutrons of all orders. For example, if the monochromator crystals are set to diffract neutrons of energy 0.03 ev, neutrons of energy 0.12 ev (second order) and 0.27 ev (third order) will be reflected into the experimental beam also. In the analyzer position, the same

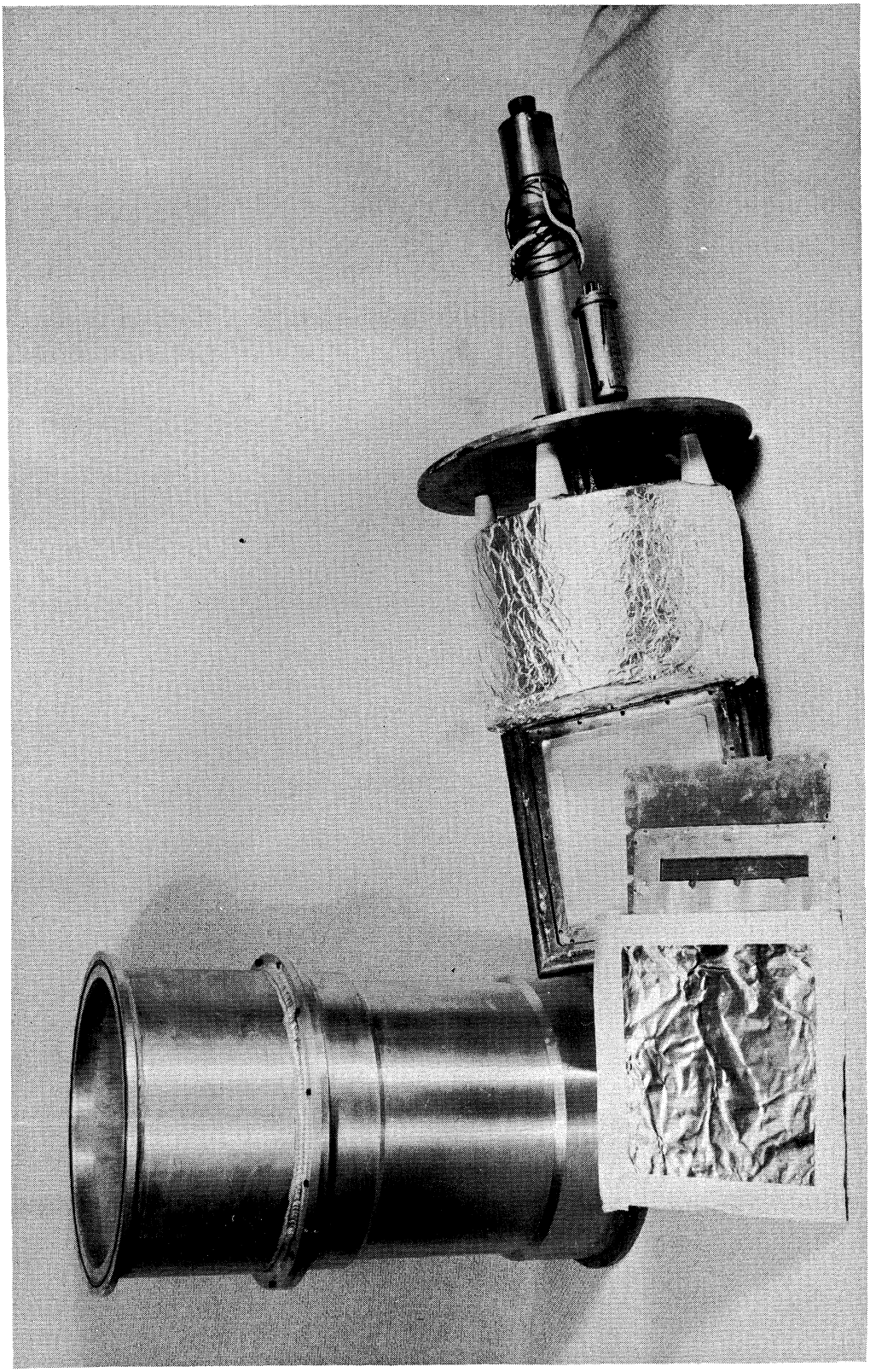

Figure 29. Cryostat and target assembly.

effect occurs. This problem is a major limitation of the system and must be solved if the first order inelastic scattering cross section is to be correctly measured.

For any given incident energy and fixed analyzer energy, the measured scattering will include components of all orders. Considering only first and second order energies in the incident beam (E_o and $4E_o$), and first and second order energies of the analyzer system (E_f and $4E_f$), the measured scattering will include these four components:

a. $E_o \rightarrow E_f$

b. $4E_o \rightarrow E_f$

c. $E_o \rightarrow 4E_f$

d. $4E_o \rightarrow 4E_f$

The cross section under study is $\sigma(E_o \rightarrow E_f)$, component a; the other three components must be eliminated. Two factors minimize the contribution from component b, $\sigma(4E_o \rightarrow E_f)$. First, the inelastic scattering data indicates that for polyethylene the inelastic scattering cross section decreases monotonicly with increasing energy transfer; therefore, component b will generally be smaller than the first order transfer, component a. This cross section behavior has been observed at 298°K, 125°K and 90°K for energy transfers up to 90 millivolts and is expected to continue beyond this energy. (This can be verified by higher energy transfer measurement but this has not been done as yet.) Second, the second order component in the incident beam is small in the energy range 0.040 to 0.15 ev (see Figure 22). An

estimate of the magnitude of this correction for a typical polyethylene experiment (90°K, E_f = 0.027 ev) using the measured cross section data and the measured spectrum data shows that this correction is about 3% for an energy transfer of 3 millivolts, 1% for an energy transfer of 9 millivolts, and less for larger energy transfers. These estimates assume that there are no large resonances in the inelastic scattering cross section beyond the measured energy transfer range. Because of the small magnitude of these values, no correction was made for this component.

Component c, $\sigma(E_o \rightarrow 4E_f)$, is small relative to component a for large energy transfers because of the monotonically decreasing cross section, but, as the incident energy approaches $4E_f$, this component will increase and become larger than component a, the first order cross section. Unfortunately, this energy region near $4E_f$ is important and it was therefore necessary to measure component c. To obtain this correction, two experimental runs were made. The first, with the analyzers set at E_f, measures all four components, a, b, c, and d. The second, with the analyzers set at $4E_f$, measures the two components, c and d. To normalize the two sets of data, vanadium resolution measurements are made at $4E_f$ for both analyzer settings. The ratio of the two vanadium curves is used as a normalization factor. This factor gives the response of the analyzer system to neutrons of energy $4E_f$ for an analyzer setting of E_f relative to that at $4E_f$. In essence, the normalization factor is a measure of the ratio of first to second order reflectivity for

the copper crystal used in the analyzer system modified by the finite size of the crystal. This modification arises because the seven inch long analyzer crystals do not intercept the whole beam from the analyzer collimators at small Bragg angles (high analyzer energies). The normalization factor is of order 0.4.

The net signal for the $4E_f$ experimental scan is multiplied by the normalization factor and subtracted from the first order (E_f) scan to obtain the net first order inelastic scattering data. The magnitude of this correction varies from about 1.5% at the first order elastic peak, to 50% for a transfer of 65 millivolts in a typical experimental run. This procedure corrects for both components c and d. In Chapter IV, the experimental results present the observed net cross section and the second order corrected cross section; by observation of this data, the effect and magnitude of the second order correction can be easily seen. For example, for energy transfers from zero to 30 millivolts, the second order correction is less than 10%.

Detectors and electronics

Detectors

Monitor detectors

The monitor detector is a pancake-shaped fission chamber which intercepts the entire beam at the exit of the turret port. The monitor detector should have a low gamma ray sensitivity, low efficiency and high transmission; the parallel plate fission

chamber meets these requirements very well. The monitor was designed and constructed by Mr. Edward Straker. The monitor windows are 1100-S aluminum plates on which a deposit of uranium (enriched in the isotope 235) was deposited by electrolysis. These two plates form the cathode of the detector; the anode is another thin aluminum plate insulated from the other plates by teflon spacers. The filling gas is 90% argon, 10% methane at atmospheric pressure.

The calculated absolute detection efficiency versus energy is shown in Figure 30. Two sets of monitors have been constructed. Figure 30 shows the absolute efficiency for the first monitors; the second set now in use have an efficiency which is lower by a factor of 13. This reduction was accomplished by decreasing the U-235 enrichment in the plated uranium. A typical counting rate at two megawatts reactor power is 82,500 counts per minute at 0.033 ev. The detector is operated as a pulse ionization chamber at 500 volts. The monitor transmission is about 97.5% and is essentially constant with energy, because most of the neutrons that are removed interact with the aluminum and not with the uranium. The reliability of these monitor detectors has been excellent. The inherent background is very low, less than five counts in 24 hours.

BF_3 detectors

The BF_3 detectors were custom designed and built by the Reuter-Stokes Company for this spectrometer. The design

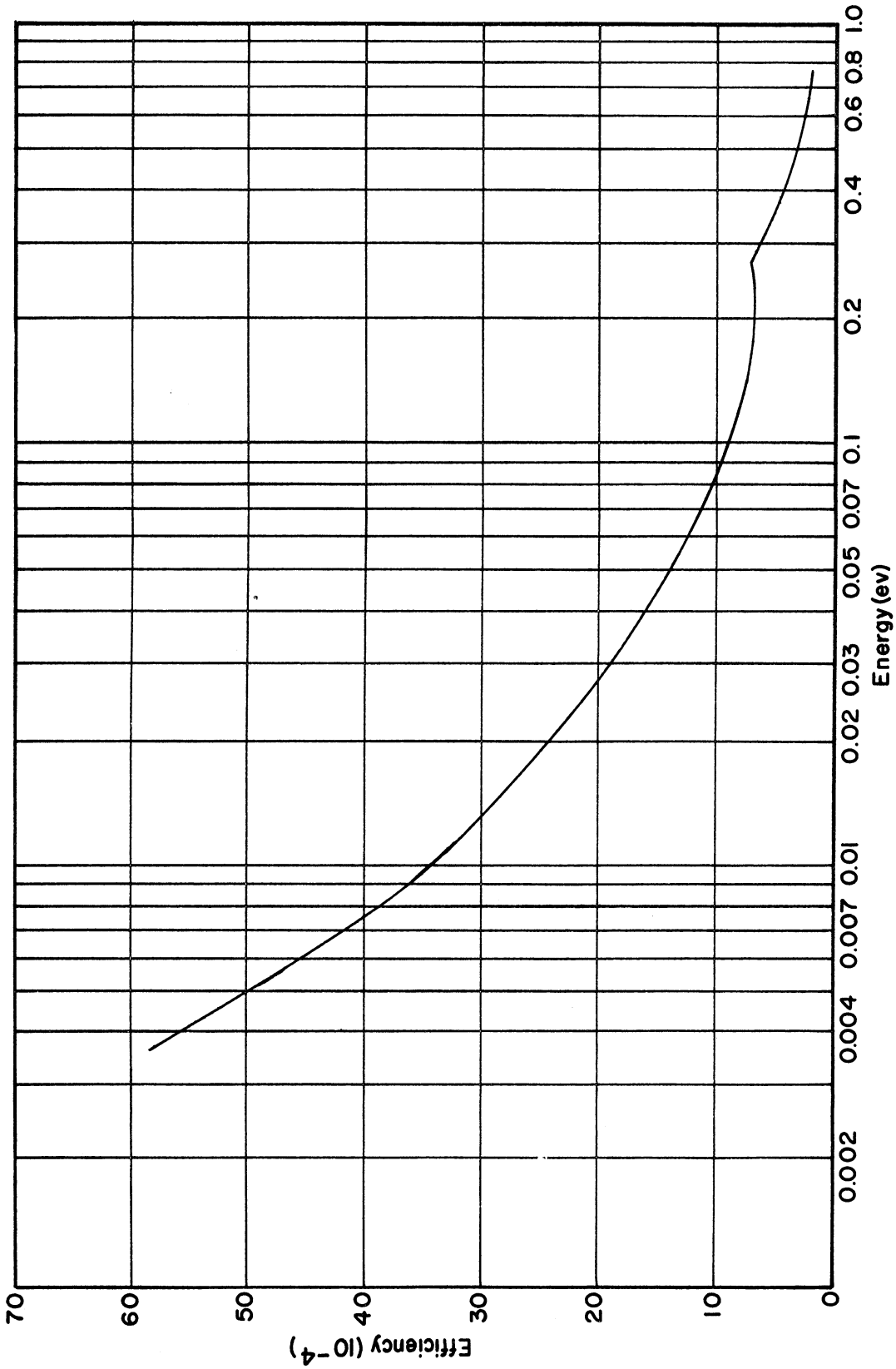

Figure 30. Calculated absolute efficiency for monitor detector.

specifications include a three-inch diameter, a ceramic end window and high efficiency. The plateau for these tubes extends over 300 volts, with a plateau slope of less than 3% per 100 volts. The detectors have low inherent noise (0.25 counts per minute). The calculated absolute efficiency is shown in Figure 31. The detectors have been operated at an anode voltage of 5000 volts. This has caused noise problems in the counting channel, usually associated with high voltage cable connector breakdown or leakage in the preamplifiers when the humidity was high. This problem was solved by controlling the humidity in the experimental area, by sealing the preamplifiers and by joining the preamplifiers directly to the BF_3 tubes. The BF_3 detector characteristics are listed in Table 12.

TABLE 12

BF_3 DETECTOR CHARACTERISTICS

Overall Length	9 inches
Overall Diameter	3 inches
Cathode Material	304 Stainless Steel
Anode Material	.004 inch Tungsten
Active Length	6 inches
Window	0.125 inch Al_2O_3
Fill Gas Pressure	100 cm Hg (96%B^{10})
Typical Operating Settings:	
Voltage	5000 volts
Amplifier Gain	400
Discriminator Setting	20 volts
Plateau Length	200 volts

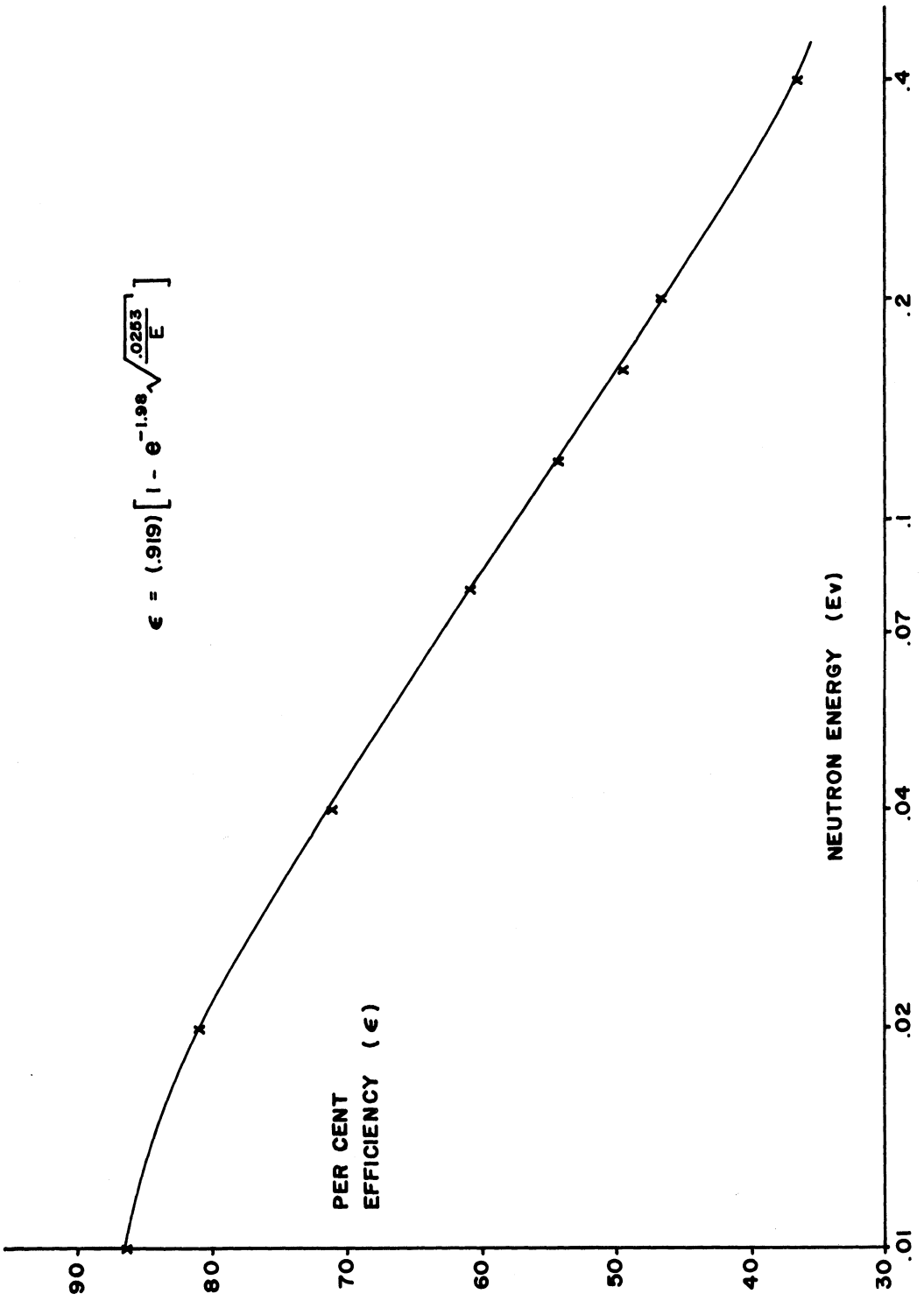

Figure 31. Calculated absolute efficiency for BF_3 detectors.

Electronics

A block diagram of the electronics system is shown in Figure 32. The monitor and counting channels are shown with their associated components. The preamplifiers, preamp power supply, adder network, sequencer and spectrometer configuration components were designed by Mr. William Myers. Rotation of the main Bragg arm and the target table is provided by "Slo-Syn" d.c. impulse motors.

The data collection sequence is initiated by the monitor preset scaler. The detector channel collects background data until the preset monitor count is reached. The accumulated count is printed, the sequencer drives the target to the polyethylene position (180° rotation), the scalers reset, and signal counts are collected until the preset counting ratio (signal to background prints) is reached. At this time, the motor pulsers are activated to generate power pulses to drive the target and main Bragg arm motors. The pulses are counted by the drive scalers until the preset numbers are reached. An "and" circuit generates a signal to reset the monitor scaler when the main arm drive finishes, and data collection at this new incident energy position begins again.

Data processing

The data from the printer tape is punched into input cards for the IBM 7090 Computer. The computer normalizes the counts to a constant number of neutrons incident on the target for each incident energy, computes the net count corresponding

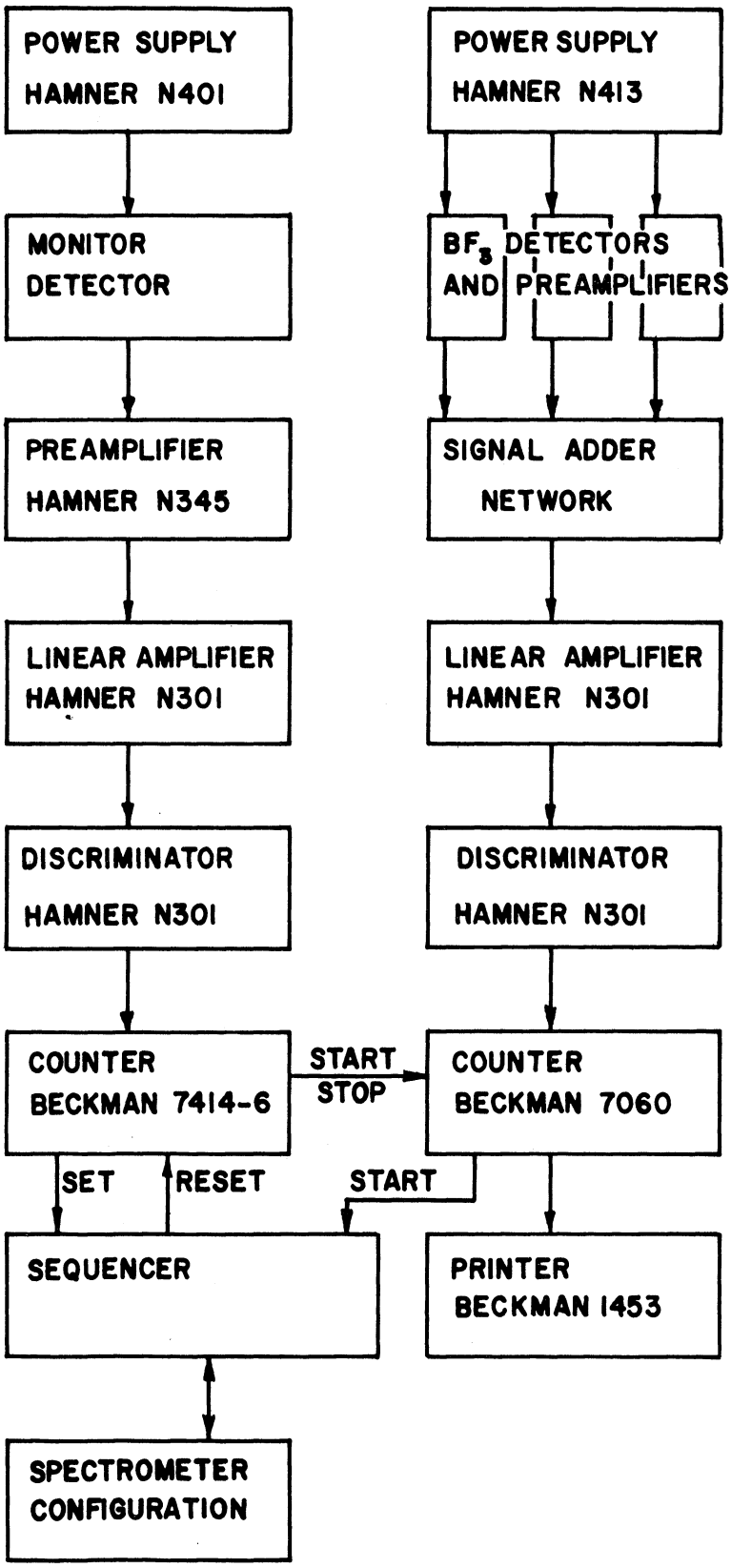

Figure 32. Block diagram of spectrometer electronics.

to each incident energy, and the net count averaged over three and five incident energy positions (two and four nearest neighbor data point averaging). No correction is necessary for the energy response of the BF_3 detectors because the analyzer energy is held fixed during the experimental run. The correction for second order response of the analyzers is made. The net corrected first order count rate which results after these corrections have been made is directly proportional to the energy differential cross section. The phonon frequency distribution, $g(\epsilon)$, is then computed according to equation (II-15).

CHAPTER IV

EXPERIMENTAL RESULTS

Measurements at 298°K

The initial data was taken with a target temperature of 298°K. To check the reproducibility of the spectrometer, a series of measurements were made using three analyzer energy settings. The scattering data for one of these room temperature experiments is shown in Figure 33. The graph presents three curves: first, the measured cross section with all corrections except second order; second, the measured cross section corrected for second order; and third, the measured background data. The corrections to the data (see page 94) are made in the following order: the observed total count is corrected by subtracting the background count, and the net count is multiplied by the monitor correction factor. This value is averaged with the results for the two nearest neighbor values to give the data points shown as Curve b. The monitor corrected net averaged second order count for this same energy setting is multiplied by the normalization factor (see page 88) and the result is subtracted from Curve b to obtain Curve c. This result, Curve c, is directly proportional to the energy differential scattering cross section.[1]

---

[1] The expression for the observed count rate can be written (see derivation of equation [II-7]):

$$CR(\epsilon) = C\,\Phi(E_1)\,R(\theta_1)\left(\frac{d^2\sigma}{d\Omega\,d\epsilon}\right)R(\theta_2)\,\epsilon_A\,\frac{d\theta_1}{dE_1}\,\frac{d\theta_2}{dE_2}$$

where A refers to the analyzer system, $\epsilon = E_1 - E_2$, and C is a constant and the other symbols are defined in Chapter III. The count rate at the monitor (M) is: $CR(E_1) = C\,\Phi(E_1)\,R(\theta_1)\,d\theta_1/dE_1$. When the data is normalized to a constant number of neutrons incident

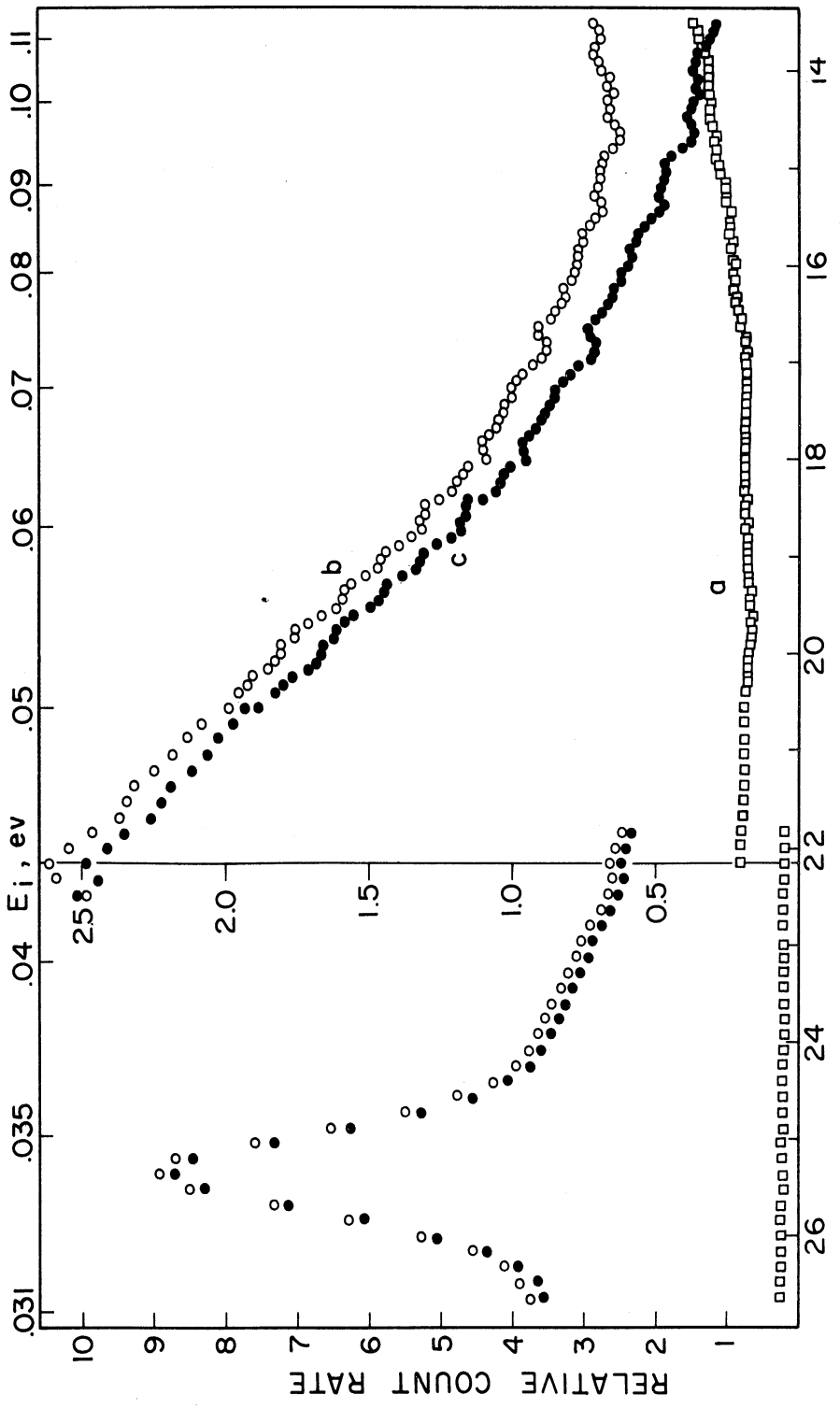

Figure 33. Scattering cross section for Marlex 6050 polyethylene at 298°K, E_f = 0.0341 ev. (a) Background. (b) First and second order cross section, background corrected. (c) Scattering cross section, all corrections made.

The phonon frequency distribution is calculated using the second order corrected data, Curve c.

The three room temperature frequency distributions are shown in Figure 34 for analyzer settings of 0.0268 ev, 0.0341 ev and 0.0595 ev. The 0.0595 ev data is not corrected for second order because for this analyzer energy setting, the correction is very small, as evident from Figure 22.[1] The standard deviation due to counting statistics only is shown at some typical data points in Figure 34. The energy resolution of the system is measured at the analyzer energy setting. To calculate the resolution corresponding to any inelastic energy transfer, the spectrometer resolution in energy is computed using the square root of the sum of the squares of the resolution for the incident energy and the resolution of the analyzer energy. In typical data collection, the number of data points observed is large enough that averaging the data over nearest neighbor data points does not broaden the calculated resolution.

---

on the target, the normalized count rate at the analyzer is: $N.C.R.(\epsilon) = c'' \left[\frac{d^2\sigma}{d\Omega d\epsilon}\right] R(\theta_2)\frac{\epsilon_A}{\epsilon_M}\frac{d\theta_2}{dE_2}$. With the energy of the analyzer system held constant, $\epsilon_A R(\theta_2)\frac{d\theta_2}{dE_2}$ is constant; therefore, the observed count rate multiplied by the monitor correction efficiency (ϵ_M) is directly proportional to the energy differential scattering cross section.

[1]The second order contamination of the primary beam is very low (2% at 0.08 ev, 3% at 0.11 ev). Also, the energy (0.238 ev) which scattered neutrons must possess to be second order reflected by the analyzer crystals, is large relative to the energies in the incident beam. Energy transfers by neutron energy gain from the target to this high energy are unlikely because of the low population density of high energy levels in the target at room temperature ($T \approx 0.025$ ev).

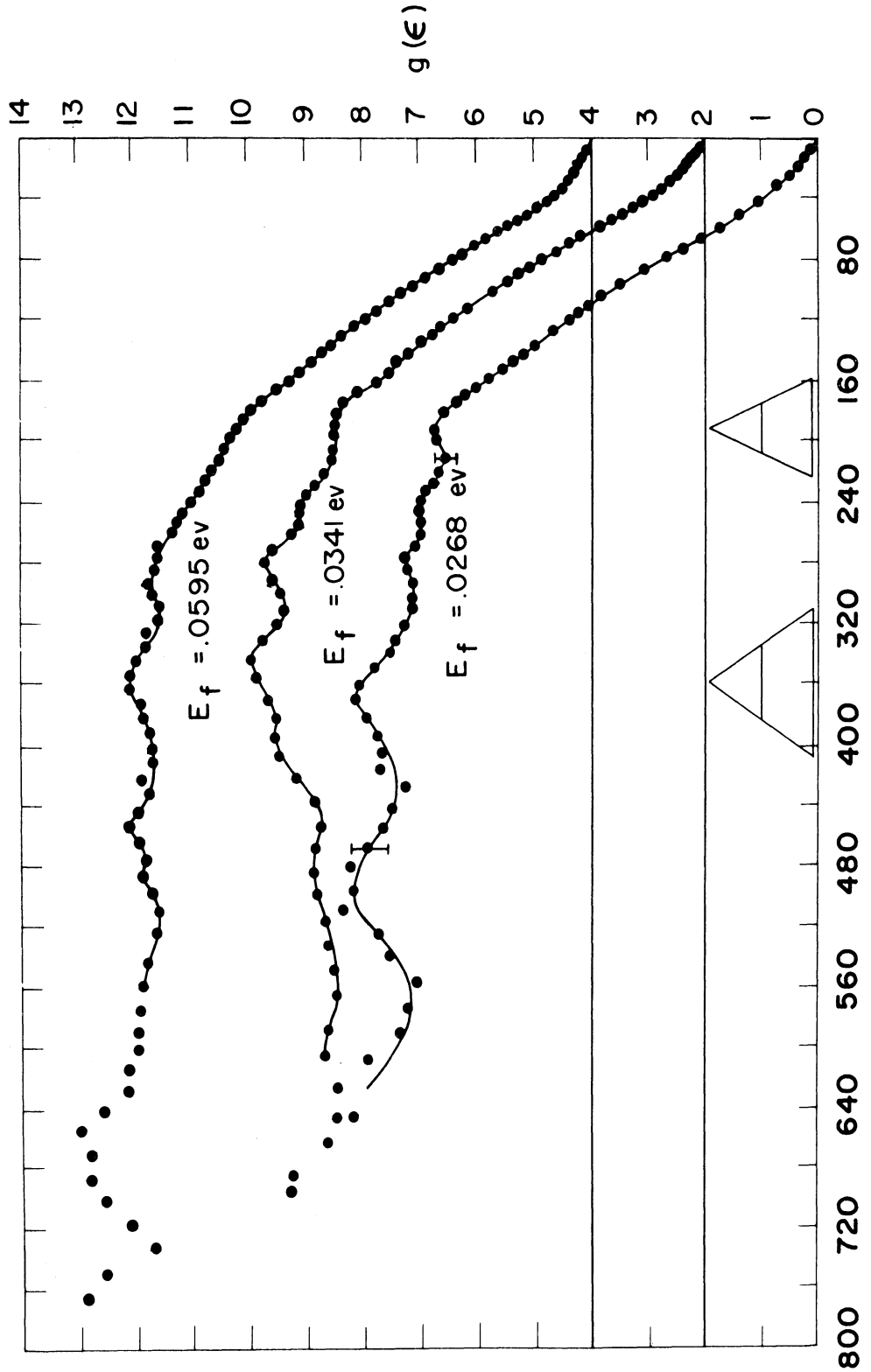

Figure 34. Frequency spectra for Marlex 6050 polyethylene at 298°K, E_f = 0.0268 ev, 0.0341 ev, 0.0595 ev.

Both the frequency spectra and the corrected cross section curves seem to show discrete energy transfers, indicated either as peaks in the data, or changes in slope of the curves. A shoulder or peak is seen in each curve corresponding to an energy transfer of about 190 cm^{-1}.[1] It is assumed that this peak is seen most clearly in the 0.0268 ev data both because the system resolution is best for this curve, and multiphonon effects are minimum (see equation [II-16]). Less pronounced transfers are indicated near 60 cm^{-1}, 95 cm^{-1}, and 140 cm^{-1}, where a change of slope is seen for all three frequency spectra. Each of the curves also indicates a transfer exists near 240 cm^{-1} and 280 cm^{-1}, and near 370 $\pm$ 20 cm^{-1}. A less consistent peak is indicated near 500 cm^{-1}; this peak is most strongly indicated in the 0.0268 ev curve. Clearly these spectra exhibit a much more complicated picture than would be expected from the single chain theory, which predicts just two acoustic modes, near 190 cm^{-1} and 500 cm^{-1}.

The "cold" neutron data obtained by Danner (1) with a similar target at a similar temperature compare rather poorly with these results as is shown in Figure 35. The "cold" data reveal a more distinct peak near 170 cm^{-1}; this is in crude agreement with the present result. Above this first peak, the "cold" spectrum is smoother with an indication of peaks near 265 cm^{-1} and 500 cm^{-1}. The warm spectrum indicates peaks in

---

[1]The frequency values quoted for the inelastic components correspond to energy transfers whose value in electron volts can be obtained by dividing the frequency values by 8060.

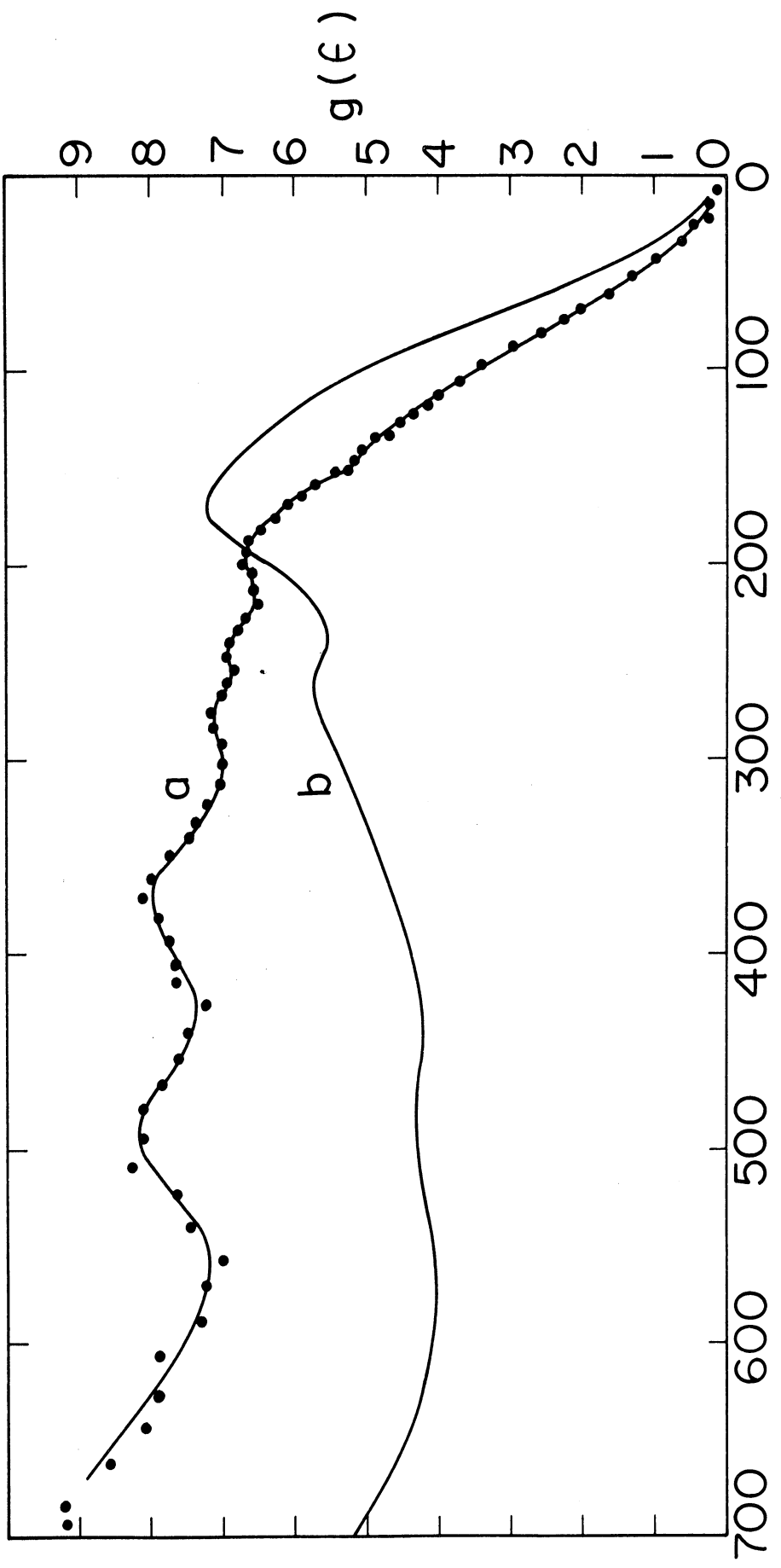

Figure 35. Comparison of frequency spectra for room temperature Marlex 6050 polyethylene (0.029 inch). (a) "Warm" neutron results, E_f = 0.0268 ev. (b) "Cold" neutron results, E_o = 0.005 ev.

this frequency region near 240, 280, 370 and 500 cm^{-1}. Both spectra give a slight indication by change in slope of low frequency events near 90 cm^{-1} and 140 cm^{-1}; however, the rapid rise in the frequency spectrum tends to mask low frequency events, which are better seen in the cross section data.

Measurements at 125°K

As noted in Chapter II, hindered rotations begin in the disordered regions at a temperature near 120°K. To obtain the frequency spectrum when these motions were reduced or eliminated and to reduce the multiphonon effects, a series of low temperature inelastic scattering experiments were undertaken. The first measurements were taken at an average target temperature of 125 $\pm$ 5°K. The analyzers were set to 0.0268 ev to obtain good system resolution as well as to provide comparison with the best room temperature data. The 125°K data are shown in Figure 36. The frequency spectrum calculated from the second order corrected cross section is presented in Figure 37.

The cross section data and the frequency spectrum at 125°K firmly show several energy transfers and suggest several others. The peak at 190 cm^{-1} is much more prominent than in the 298°K data. The slight shoulder seen near 140 cm^{-1} in the 298°K data is now easily seen near 135 cm^{-1}. Low frequency peaks occur near 45 and 65 cm^{-1} and a peak is suggested near 95 cm^{-1}, all more easily seen at 125°K than at 298°K. The frequency region above 200 cm^{-1} is dramatically changed in amplitude relative to the 190 cm^{-1} peak. The 298°K spectrum in

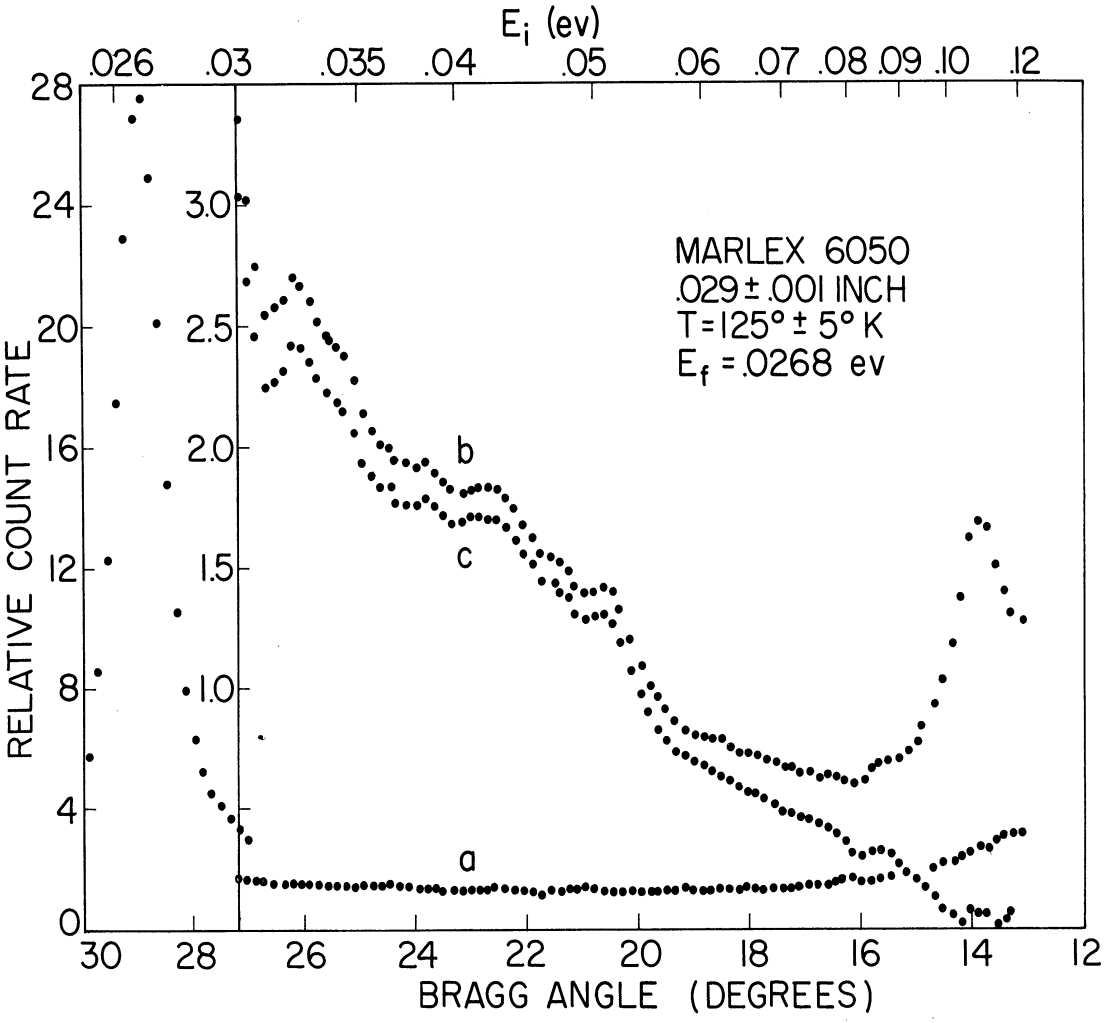

Figure 36. Scattering cross section for Marlex 6050 polyethylene at 125°K, E_f = 0.0268 ev. (a) Background. (b) First and second order cross section, background corrected. (c) Scattering cross section, all corrections made.

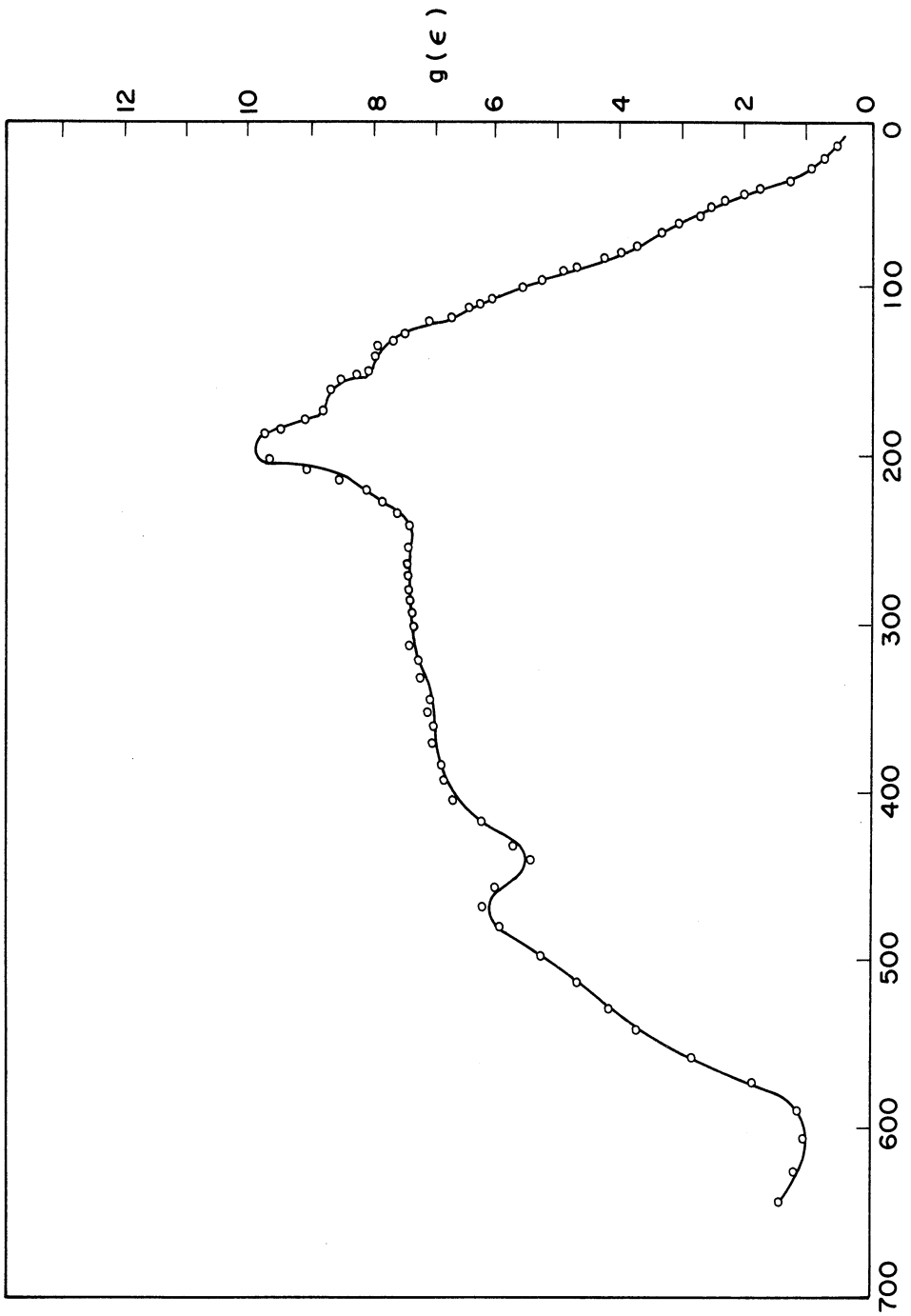

Figure 37. Frequency spectrum for Marlex 6050 polyethylene at 125°K, E_f = 0.0268 ev.

this frequency region indicated events near 240, 280, 370 and 500 cm^{-1}; the 125°K spectrum also suggests events near 280, 390, and 490-540 cm^{-1}. However, the shape of the spectrum changes markedly beyond 540 cm^{-1}, showing this event more clearly and giving better agreement with the single chain theory, which predicts no frequencies between 500 cm^{-1} and the lowest optical mode at 720 cm^{-1}.

Measurements at 90°K

29.5 mil target thickness

The marked change in the data when the target temperature was lowered to 125°K suggested further experiments at a lower temperature. The 29.5 mil thick polyethylene target was again used for the experiments at a temperature of 90°K. The analyzer energy was set to 0.0272 ev. Two identical experimental runs were made. The completely corrected cross section data at each incident energy was computed for each run; the data shown in Figure 38 are the average of results for the two identical experiments. The phonon frequency distribution, based on the average of the values calculated for each of the experiments, is presented in Figure 39.

The cross section data (Figure 38) show several clearly defined energy transfers. The prominent peak at 192 cm^{-1} is obvious, as well as the strong peak at 137 cm^{-1}, and the small peak near 90 cm^{-1}. The 65 cm^{-1} event reappears but only as a weak change in slope in the cross section data. However, while

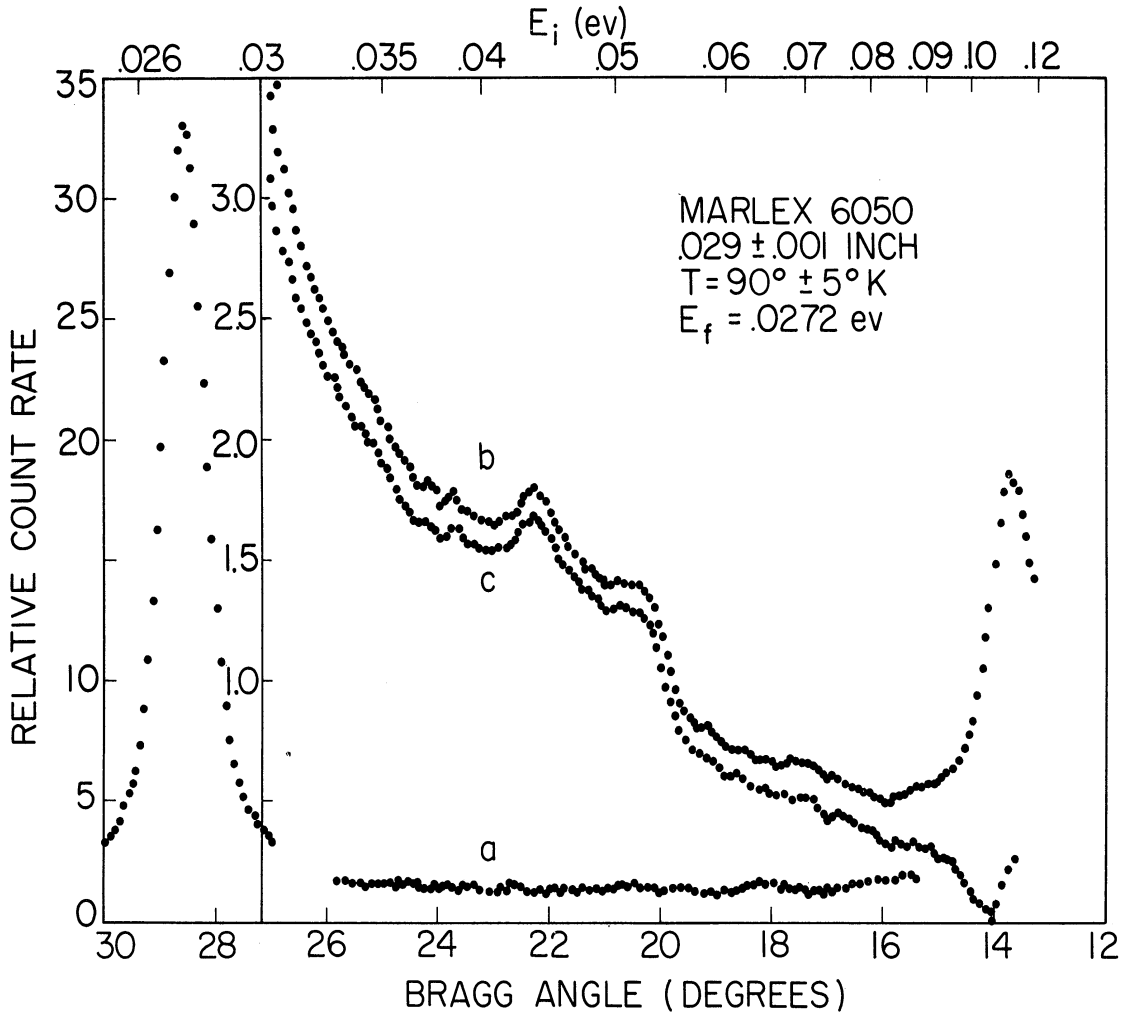

Figure 38. Scattering cross section for 0.0295 inch thick Marlex 6050 polyethylene at 90°K, E_f = 0.0272 ev. (a) Background. (b) First and second order cross section, background corrected. (c) Scattering cross section, all corrections made.

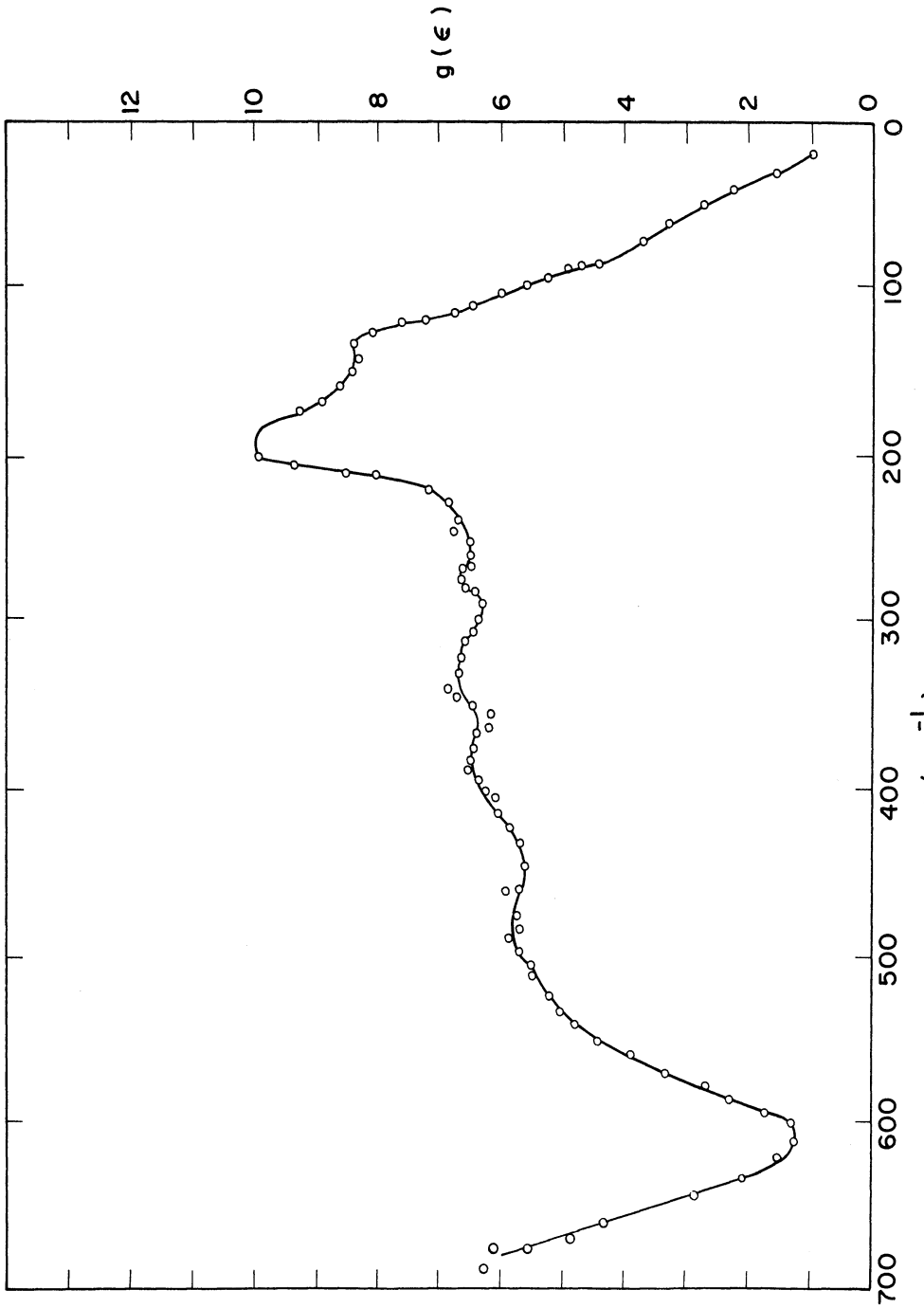

Figure 39. Frequency spectrum for 0.0295 inch thick Marlex 6050 polyethylene at 90°K, E_f = 0.0272 ev.

these peaks reproduce the 125°K data, the cross section data does not reveal the 45 cm^{-1} peak. For the frequency region above 200 cm^{-1}, fair agreement is obtained with the 125 and 298°K data. Table 13 summarizes the data for the three temperatures.

TABLE 13

FREQUENCIES OBSERVED IN MARLEX 6050 POLYETHYLENE AT 90, 125 AND 298°K (E_f=0.027 ev)

Temp., °K	Frequency, cm^{-1}										
298	--	60	95	140	---	190	240	280	---	370	500
125	45	65	95	135	165	190	---	280	---	390	490-540
90	--	65	90	137	165	192	---	270	330	390	500-540

The three frequency spectra observed at 90, 125 and 298°K with the 29.5 mil thick polyethylene target and 0.027 ev analyzer energy setting are shown together in Figure 40 after normalization at the 190 cm^{-1} peak. The decrease with temperature of the amplitude of the frequency region above 200 cm^{-1} suggests that multiphonon events and/or internal rotation effects are much less important for the low temperature targets. Nevertheless considerable scattering amplitude still persists in this frequency region at 90°K. This could be due to one or more of the following reasons: vibrations not predicted by the theory for the infinite chain, i.e., effects of branching or short chains; multiphonon effects which still exist at 90°K; unknown instrumental background effects; errors in the assumptions leading to the expression relating the cross section to the

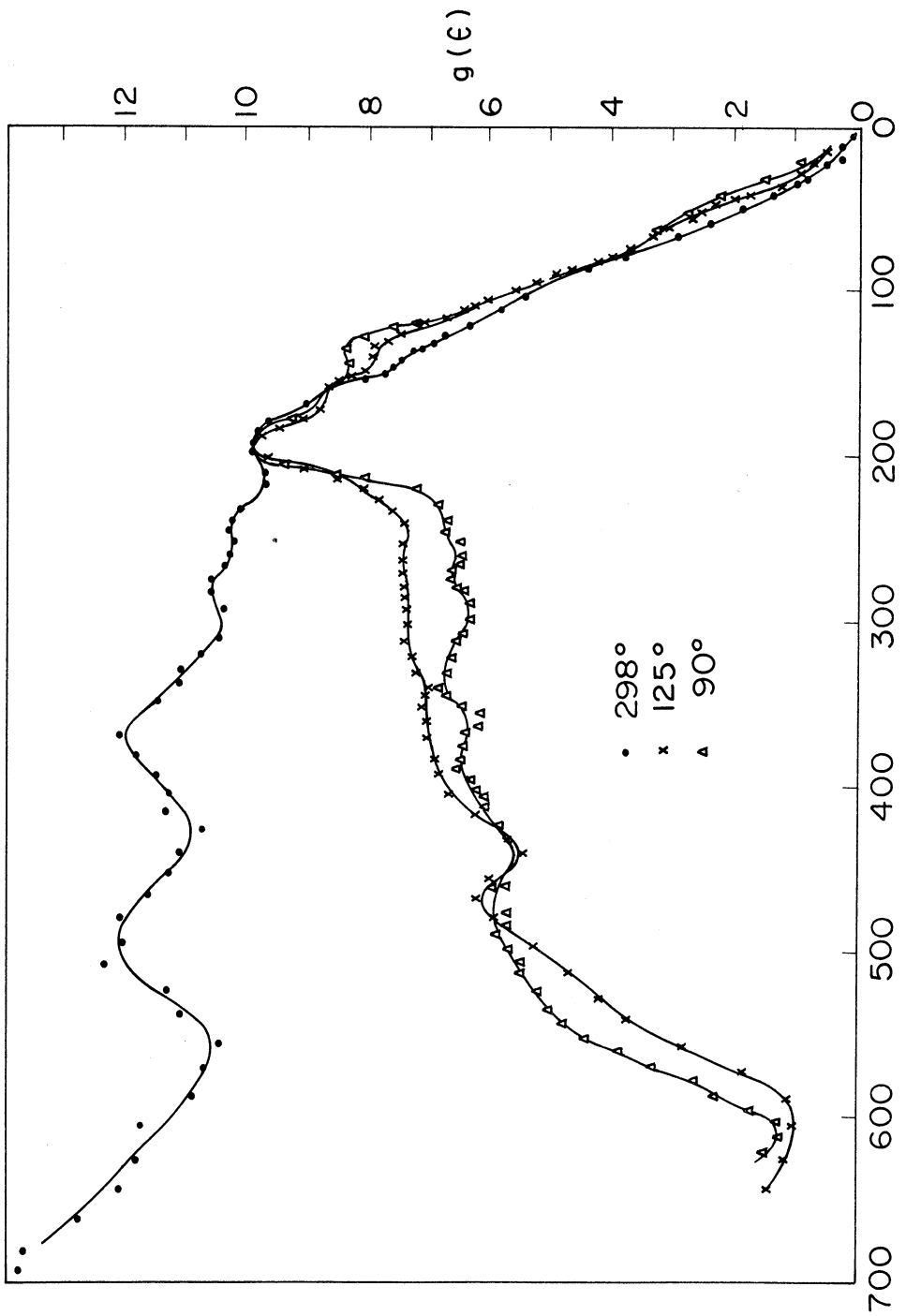

Figure 40. Variation of frequency spectra for 0.029 inch Marlex 6050 polyethylene as a function of temperature.

frequency distribution; or multiple scattering effects. It should be noted at this point that the "cold" neutron spectrum at 90°K (Figure 4b) also shows a much larger amplitude in this region between the two acoustic modes than allowed by the specific heat spectrum calculated by Wunderlich (Figure 7).

16.1 mil target thickness

Keeping the analyzer settings unchanged (0.0272 ev), another measurement was made with a thinner polyethylene target to investigate the influence of multiple scattering effects on the frequency spectrum. The target material was still Marlex 6050, with a thickness of 16.1 mils rather than 29.5 mils. This thickness change corresponds to a change in transmission at 0.045 ev from 64% for the thicker target to 78% for the thinner target.

The measured cross section data for the thinner target is presented in Figure 41. The calculated phonon frequency distribution is shown in Figure 42. Again two complete experimental runs were made; the data shown in Figures 41 and 42 are the average values of the two runs. In general the cross section data reproduces the results seen with the thicker target, but there are some differences.

First, the ratio of the peak at 192 cm^{-1} to the valley at 250 cm^{-1} has increased; in this respect the thinner target data more closely resembles the "cold" neutron data (Figure 4b). Second, the most prominent transfers at 45 cm^{-1}, 135 cm^{-1} and 192 cm^{-1} remain, but the transfer near 160 cm^{-1} is now much

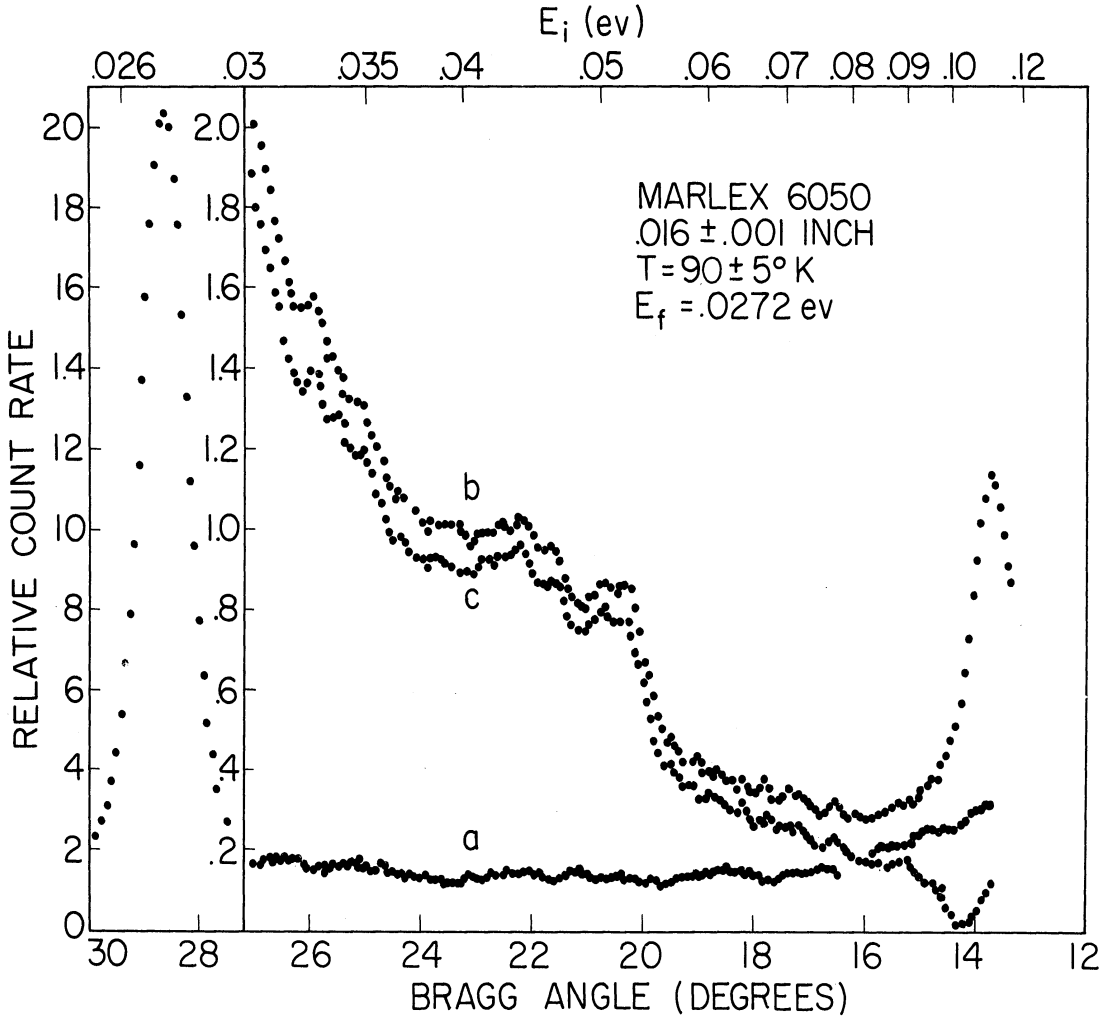

Figure 41. Scattering cross section for 0.0161 inch thick Marlex 6050 polyethylene at 90°K, E_f = 0.0272 ev. (a) Background. (b) First and second order cross section, background corrected. (c) Scattering cross section, all corrections made.

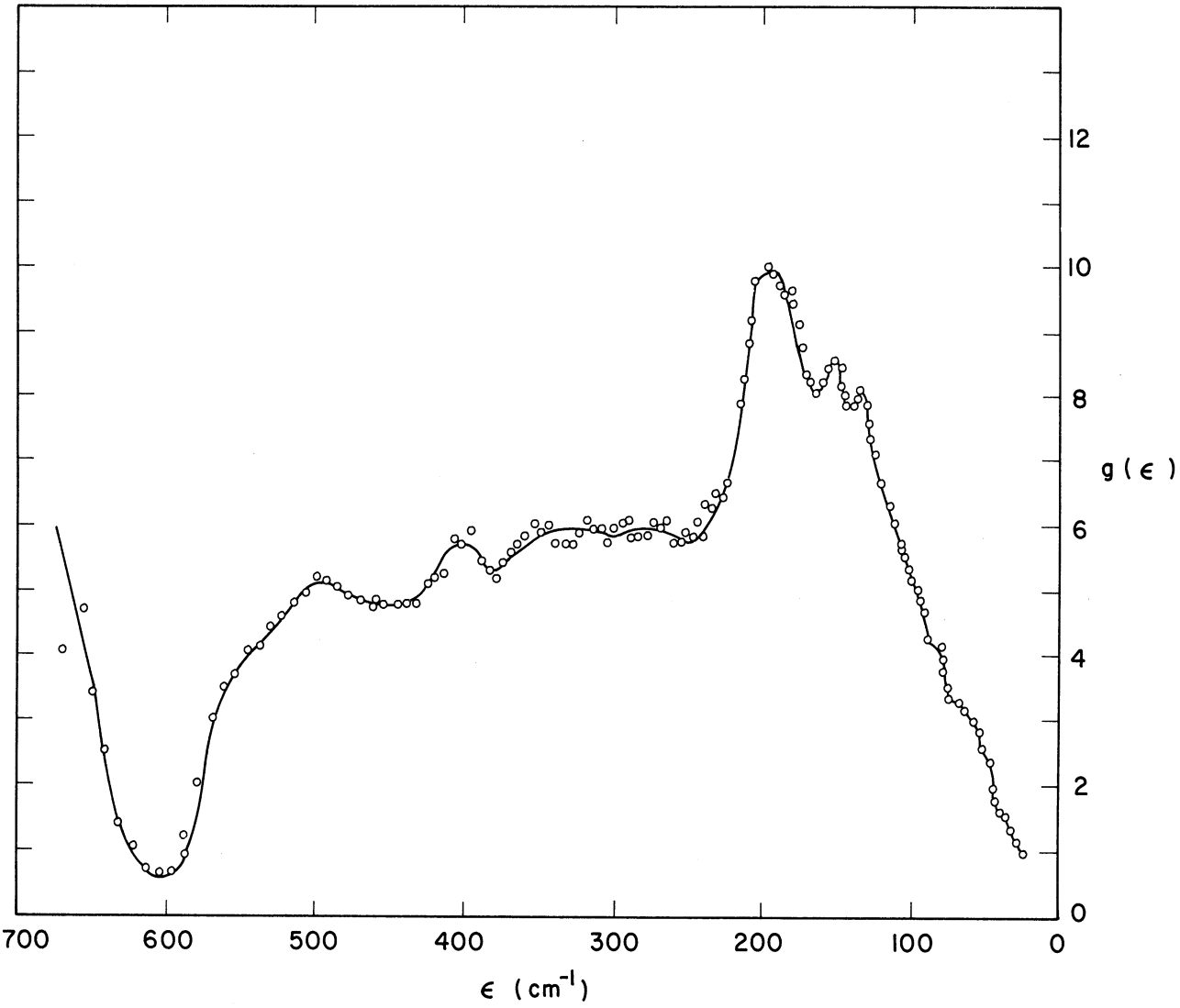

Figure 42. Frequency spectrum for 0.0161 inch thick Marlex 6050 polyethylene at 90°K, E_f = 0.0272 ev.

sharper. The easily identified transfers near 510 cm^{-1} and 270 cm^{-1} are again seen as well as the weaker transfers near 65 cm^{-1}, 95 cm^{-1}, and 390 cm^{-1}. The large amplitude of the component of the frequency distribution in the frequency region between the two predicted acoustic modes remains. The magnitude of the frequency distribution in this region is somewhat less than for the thicker target, again agreeing more closely with the "cold" neutron data when the three sets of data are normalized at the 190 cm^{-1} peak.

Comparison of the spectra at 90°K for the two different target thicknesses indicates that the effect of multiple scattering is not large although the target thickness was changed by almost a factor of two. The 90°K frequency spectra are shown together in Figure 43 where they are compared to the 100°K "cold" neutron data. Although both targets are Marlex 6050 and the crystallinities are similar (89.7 and 90.7%), it is not possible to rule out possible differences in the lattice structures, such as branching, since they were not prepared from the same source. For this reason further experiments with thin targets of identical composition are needed to fully guarantee the absence of multiple scattering effects.

It should be noted that the interpretation of the scattering data for large energy transfers (above about 450 cm^{-1}) is complicated by the large second order correction necessary with the analyzer system set to 0.027 ev. At this energy setting, the second order elastic peak is centered about 0.108 ev, which corresponds to an apparent first order energy transfer of 0.081 ev

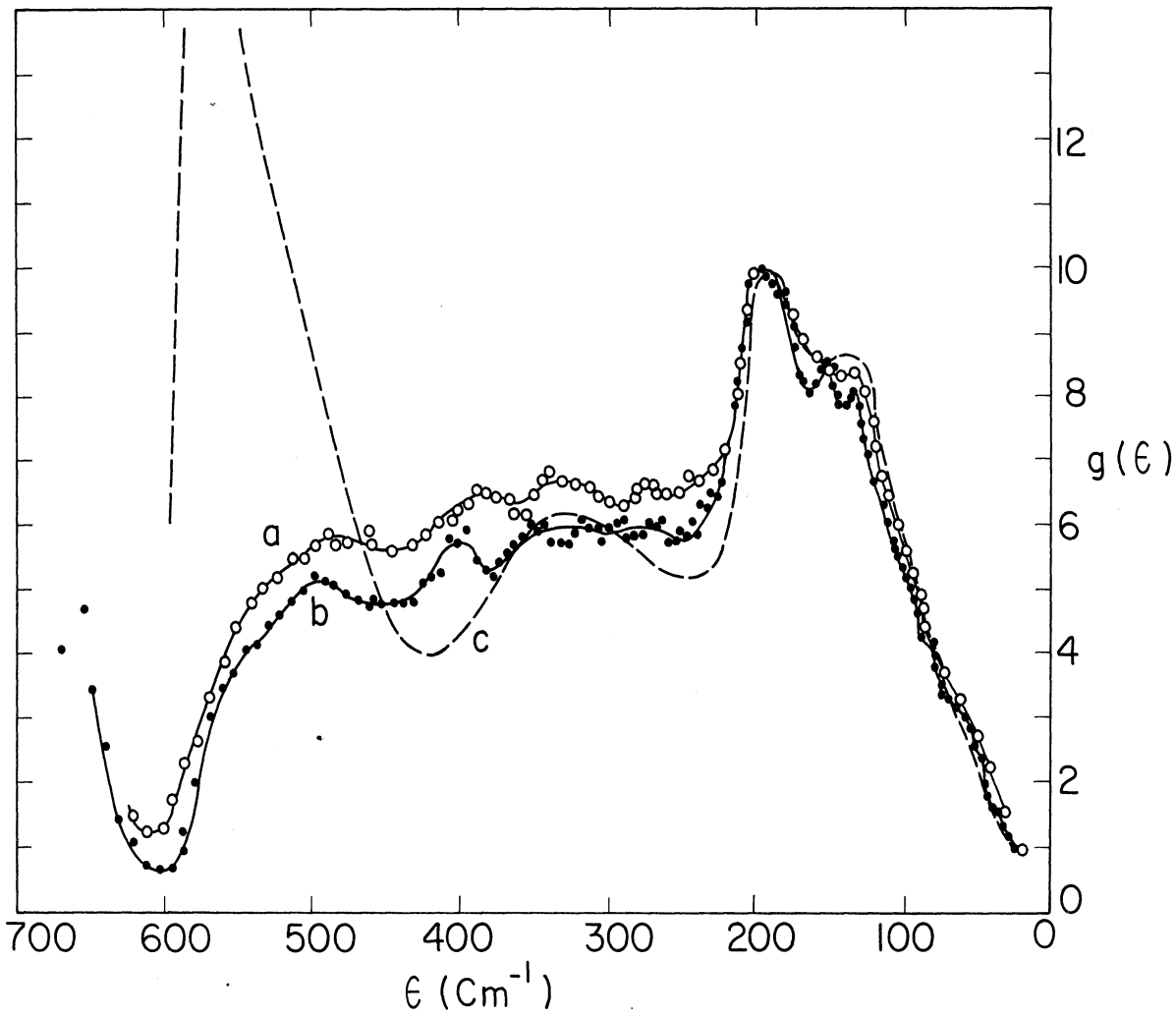

Figure 43. Comparison of frequency spectra for Marlex 6050 polyethylene. (a) "Warm" neutron results, 0.0295 inch thick target at 90°K. (b) "Warm" neutron results, 0.0161 inch thick target at 90°K. (c) "Cold" neutron results, 0.0295 inch thick target at 100°K.

(648 cm^{-1}). This difficulty can be overcome at a slight cost in system resolution by changing the analyzer system to a larger energy. For example, at an analyzer setting of 0.034 ev, the second order elastic peak corresponds to an energy transfer of 0.102 ev (816 cm^{-1}); the second order correction for the frequency range 500-720 cm^{-1} is now much less. Further experimental work to examine this frequency range with a higher analyzer energy setting is planned to confirm the results presented here.

Debye-Waller factor

The one phonon incoherent approximation used in the analysis of the measured cross section data to compute a frequency distribution contains the Debye-Waller factor (see equation II-15). This factor was set equal to unity in the calculation of all the frequency spectra presented above. However, an attempt was made to determine an approximate value of this factor by a comparison of the elastic scattering cross section as a function of temperature. The Debye-Waller factor is directly proportional to the elastic incoherent cross section (zero phonon cross section, equation II-10):

$$\frac{d^2\sigma}{d\Omega d\epsilon} = \frac{Nk'}{k}\,\delta(\epsilon)\sum_s \left|a^s_{inc}\right|^2 e^{-2W} \qquad \text{(IV-1)}$$

The first order elastic scattering amplitudes were determined by subtracting from the measured cross section an estimated inelastic component. The results are shown in Table 14. The ratio of the cross sections at 298° and 125°K to the cross

section at 90°K was used to compute estimated Debye-Waller factors for each temperature. The ratio of the elastic scattering intensity at two temperatures is related to the Debye-Waller factor by:

$$\frac{\left(\frac{d^2\sigma}{d\Omega dE}\right)_{T_1}}{\left(\frac{d^2\sigma}{d\Omega dE}\right)_{T_2}} = \frac{e^{-2W(T_1)}}{e^{-2W(T_2)}} = \frac{e^{-a(T_1)K^2}}{e^{-a(T_2)K^2}} = e^{-[a(T_1)-a(T_2)]K^2} \qquad \text{(IV-2)}$$

TABLE 14

RELATIVE POLYETHYLENE ELASTIC SCATTERING AMPLITUDES AT 90, 125 AND 298°K (E_f=0.027 ev)

Temp., °K	Total Amplitude	Inelastic	Elastic	Normalized Ratio
298	12.05	3.68	8.37	0.28
125	27.7	3.5	24.2	0.81
90	33.2	3.4	29.8	1.00

The absolute value of the Debye-Waller factor at 90°K can be obtained experimentally by measuring an elastic angular distribution at this temperature. These cross section measurements can be used with equation (IV-1) to determine the coefficient [a(90°)] for various values of K^2. Unfortunately, this experiment has not been done as yet. However, equation (IV-2) can be used with the values in Table 14 to demonstrate the change in the value of the coefficient with temperature. At 125°K the value of the coefficient is [3.9 + a (90°)]; the value at 298°K is [23.5 + s (90°)]. It should be noted that the Debye-Waller factor can also be calculated using the measured

frequency distribution and equation (II-13). An attempt (27) to calculate this factor using the dispersion curves of Tasumi, Shimanouchi and Miyazawa (9) failed because the low frequency region caused the integral to diverge. Further calculations using the measured frequency distribution are planned (13), both to determine the value at 90° and to investigate the temperature dependence of the Debye-Waller factor for polyethylene.

CHAPTER V

CONCLUSIONS AND DISCUSSIONS

Comparison of "cold" and "warm" neutron scattering results

The phonon frequency spectra for Marlex 6050 polyethylene at 90° (Figures 39 and 42) show good agreement with the cold neutron results reported by Danner et al. (1) for the frequency range below 200 cm^{-1}. The three spectra obtained at low temperature are shown together in Figure 43. In particular, the major events near 192 cm^{-1} and 135 cm^{-1} are clearly confirmed. A weaker event near 65 cm^{-1} is seen in both sets of experiments. The broad maximum centered about 330 cm^{-1} in the "cold" neutron data is evident in the "warm" neutron results, but is less pronounced. However, several additional frequencies are indicated below 200 cm^{-1} in the "warm" results; a peak is seen near 50 cm^{-1}, a very weak peak is suggested near 95 cm^{-1} and another near 165 cm^{-1}.

Above 330 cm^{-1} the low temperature spectra obtained by "cold" and "warm" techniques disagree markedly. The "cold" neutron data show only a giant peak near 570 cm^{-1}, whereas the "warm" neutron experiments consistently show a moderately strong broad peak near 500-540 cm^{-1}. This data apparently provides better agreement with the second acoustic mode which is predicted near 500 cm^{-1}. A second peak centered near 390 cm^{-1} shows only in the "warm" neutron results. The results

above about 450 cm^{-1} are less reliable in both sets of experiments. The "warm" results are influenced by the proximity of the second order peak, and the "cold" neutron results suffer apparently from poor statistics. In addition, in both experiments the energy resolution becomes worse with increasing energy transfer. In the frequency region between 200 and 500 cm^{-1} the amplitude of the frequency distribution is on the average about 10% greater for the "warm" neutron results, after the spectra are normalized at the 192 cm^{-1} peak. This greater amplitude suggests somewhat greater multiphonon effects might be present in "warm" neutron results.

The experiments with room temperature targets compare less favorably (see Figure 35). In both sets of data the structure is diffuse. The peak near 190 cm^{-1} in the "warm" data is seen near 170 cm^{-1} in the "cold" data. A new peak, near 370 cm^{-1}, is suggested and this may well be the room temperature appearance of the extra peak at 390° noted above. Changes in shape of the frequency distribution indicate other transfers which are much more easily seen in the low temperature experiments. At 298°K both internal rotation effects and multiphonon events are present and certainly complicate the frequency spectrum. The strong effect of temperature on the frequency distribution seen by the "cold" neutron technique is seen even more strongly in the "warm" neutron experiments, and this is consistent with the larger multiphonon correction expected for the "warm" neutron momentum range. It must

be concluded, therefore, that the present room temperature experiments on polyethylene are less easily interpretable and, therefore, probably less useful than the low temperature data.

The comparison of frequency spectra for two target thicknesses shown in Figure 43 indicates that the effect of multiple scattering is not large. The thin target data indicates sharper structure, but the spectral profile is about the same. Both targets are Marlex 6050 and approximately 90% crystalline; however, differences in the lattice structure are possible since they were not prepared from the same Marlex source. It would be desirable to repeat this experiment with multiple target layers prepared from the same polyethylene source.

Comparison of low temperature results with theoretical predictions

The two acoustic modes predicted by Tasumi, Shimanouchi, and Miyazawa (9) using a linear chain model for the polyethylene molecule have high frequency limits at 190 and 500 cm^{-1}. These values are in good agreement with two prominent peaks seen in the low temperature frequency spectra if the temperature dependence of these skeletal vibrations is small. The additional structure seen in the experimental data is not predicted by this model; a detailed intermolecular model is believed needed to predict these extra frequencies, and still provide satisfactory agreement with the specific heat data. At least

two such models have been attempted. The calculations of Tasumi (18), including an intermolecular potential for crystalline polyethylene, predict five low frequency values which are near frequencies seen in the low temperature spectra. The Tasumi calculations also predict a shift in the high frequency limit for the lower acoustic mode from 190 cm^{-1} to about 232 and 248 cm^{-1}. This shift was not seen in the neutron scattering measurements so that the model, by itself, cannot fully explain the present data.

A recent normal vibration calculation by Miyazawa and Kitagawa (33) includes the inter-and intrachain force field, but treats the CH_2 group as a rigid unit. The intrachain potential function used a Urey-Bradley force field with the force constants adjusted to give frequency limits near 500 cm^{-1} and 200 cm^{-1}. The interchain force constants were adjusted to give agreement with the specific heat data below 10°K. The calculated frequency spectrum includes two low frequency peaks, at 80 cm^{-1} and 100 cm^{-1}. The 80 cm^{-1} value is due to overall rotatory vibrations of the chains about the chain axis, and the 100 cm^{-1} value is primarily associated with anti-parallel translatory vibration (perpendicular to the chain axis). The calculated frequency distribution gave good agreement with the measured specific heat of polyethylene.

The measured low frequency values are compared to the predicted values in Table 15. The infrared measurement of Bertie and Whalley (6) at 300°K is also included.

TABLE 15

MEASURED AND CALCULATED LOW FREQUENCIES (cm^{-1}) FOR POLYETHYLENE

"Warm" Neutron Results, 95°K	Tasumi (18) Calculations, 290°K	Miyazawa (33) Calculations, 290°K	Infrared Measurement, 300°K
45	--	--	--
65	57	--	--
90	74	80	72.5
--	104	100	--
137	133	--	--
165	169	--	--

The temperature variation of the frequency values is unknown; however, the infrared measurements of Bertie and Whalley indicated a 9% increase for a temperature change from 300° to 100°K. The two neutron measurements at 65 and 90 cm^{-1} agree quite well with the Tasumi predictions if the 9% increase is applied to the predicted values; the 90 cm^{-1} value also agrees well with the Miyazawa and Kitahawa prediction if the 80 cm^{-1} value is increased by 9%.

The frequency spectrum calculated by Wunderlich (8) is not in agreement with either the "cold" or "warm" neutron scattering spectra at low temperature, particularly above 200 cm^{-1}. If the Wunderlich spectrum is assumed to be correct, the disagreement indicates that either multiphonon effects are large so that the one phonon incoherent approximation (II-11) is not good in this region, or that unknown instrumental problems influence the cross section measurement.

Recent calculations by Summerfield and Erickson (32) indicate that the multiphonon effect is much too small to account for the amplitude difference in the frequency region 250-450 cm^{-1}. Further analysis of the theoretical assumptions relating the cross section and frequency distribution (Equation II-11) is needed to demonstrate its validity for application to this problem; the assumptions that lead to (II-11) are currently being examined by Summerfield. If the disagreement is due to instrumental effects, the detection system must collect unwanted scattering into this frequency region. There is no information to indicate that this occurs. The difference between the neutron spectra and the specific heat spectrum is thus not fully understood at this time.

Evaluation of the triple axis spectrometer method

The experimental data obtained for this thesis represents the first use of a triple axis crystal spectrometer for inelastic, incoherent scattering measurements. All previously reported frequency distributions have been obtained by the "cold" neutron technique. For the spectra presented here, the downscatter of "warm" neutrons has been employed. With low temperature targets, this method offers a real intensity advantage over the "cold" neutron technique, mainly because of the statistical population factor in Equation (II-11). For example, with the analyzers set to 0.027 ev, the cross section is 17 times larger for a 25 millivolt energy transfer

with a target at 90°K; it is about 160 times as great for a 60 millivolt transfer. This advantage provides much better statistics for analysis of the scattering data. However, the use of a triple axis spectrometer for inelastic, incoherent scattering measurements puts a great demand on the purity of the monochromator and analyzer system response. The spectrometer must not introduce either spurious peaks into the data or a steady state background count. If a constant addition is included in the observed cross section, the frequency spectrum is skewed upwards with increasing energy transfer. The incident beam must contain less than 0.1% contamination; aluminum diffraction experiments demonstrate that any impurity is less than 1%. Further investigation is planned to obtain more information on this problem.

The effect of multiphonon interference on the measured scattering data apparently does not produce a major difference between the "cold" and warm neutron techniques for low temperature polyethylene. The "warm" downscatter experiments do entail a larger momentum transfer, but the difference is not large except at low energy transfers where the effect of multiphonon events is small. The two phonon correction term, Equation (II-17), can be minimized by using a low target temperature. Hence, it is concluded that, with proper choice of targets and target temperature, this interference need not be a fundamental drawback of the method.

Order contamination is a major problem with a triple axis crystal spectrometer. The second order correction to the data becomes large at large energy transfers near the second order elastic scattering peak. This problem can be minimized to some extent at the expense of system resolution by increasing the analyzer energy setting, thus shifting the second order energy to a larger value. However, the amount of energy shift is limited by the sharp decrease in available neutron intensity above 0.12 ev.[1] The use of crystals with no second order reflectivity (i.e., silicon or germanium) would offer a solution if large crystals of these materials were available. However, at present large crystals are not available, either because of excessive cost or difficulties in growing large single crystals.

The method for second order correction of the observed data which has been outlined in Chapter III is based on the assumption that the system resolution is constant in angle (equation III-9). This assumption implies that the width of the second order elastic scattering peak with the analyzer system set at E_f is the same as the width of the first order peak with the analyzer system set at $4\ E_f$. In the experiments reported here, this assumption is important because of the close proximity of the second acoustic peak to the second order elastic peak. A change in the width of one of the elastic peaks can produce a

[1]The reactor neutron spectrum as a function of energy is shown in Figure 20.

rather large change in shape and amplitude in the frequency spectrum in the region above 500 cm^{-1}. Experiments at a higher analyzer energy setting (i.e., 0.034 ev) are planned to minimize the second order correction in the frequency region above 500 cm^{-1}.

The agreement between the low temperature spectra obtained with the crystal spectrometer and associated neutron down-scattering technique and the spectrum obtained using "cold" neutrons is taken as evidence that the technique is sound. The important intensity advantage with low temperature targets is especially attractive. Second order contamination remains a major problem; more effort is needed to reduce this effect for high energy transfer.

LIST OF REFERENCES

1. H. R. Danner, G. H. Safford, H. Boutin and M. Berger, J. Chem. Phys., 40, 1417 (1964).

2. S. Krimm, Fortschr. Hochpolym.-Forsch., Bd. 2, 51 (1960).

3. J. R. Nielsen and A. H. Woollett, J. Chem. Phys., 26, 1391 (1957).

4. J. R. Nielsen and R. F. Holland, Symposium on Molecular Structure and Spectroscopy, Columbus, Ohio, 1959.

5. H. A. Willis, R. G. Miller, D. M. Adams, and H. A. Gebbie, Spectrochimica Acta, 19, 1457 (1963).

6. J. E. Bertie and E. Whalley, J. Chem. Phys., 41, 575 (1964).

7. S. Krimm, private communication, 1964.

8. B. Wunderlich, J. Chem. Phys., 37, 1203 (1962).

9. M. Tasumi, T. Shimanouchi, and T. Miyazawa, J. Mol. Spec., 9, 261 (1962).

10. M. G. Zemlyanov and N. A. Chernoplekov, BNL 719 (C-32), Vol. I, 66 (1962).

11. A. F. Zemach and R. Glauber, Phys. Rev., 101, 118 (1956).

12. A. Sjolander, Ark. Fys., 14, 315 (1958).

13. G. C. Summerfield, private communication, 1964.

14. J. G. Kirkwood, J. Chem. Phys., 7, 506 (1939).

15. C. J. Liang, S. Krimm, G. B. Sutherland, J. Chem. Phys., 25, 543 (1956).

16. T. Miyazawa, J. Chem. Phys., 35, 693 (1961).

17. C. W. Bunn, Trans. Faraday Soc., 35, 482 (1939).

18. M. Tasumi, Doctoral Thesis, University of Tokyo, 1964.

19. J. A. Sauer and A. E. Woodward, Revs. Modern Phys., 32, 88 (1960).

20. G. Bacon, Neutron Diffraction (Oxford Clarendon Press, London, 1962), p. 69.

21. University of Michigan Progress Report 03671-2-P, N.S.F. Contract No. G-12147 (1962).

22. W. Sturm, Phys. Rev., 71, 762 (1942).

23. A. H. Compton and S. K. Allison, X-Rays in Theory and Experiment (Van Nostrand, New York, 1946).

24. G. T. Clayton and L. Heaton, ANL-6112 (1961).

25. S. Cohen, Doctoral Thesis, University of Michigan (1964).

26. S. L. Aggarwal and G. P. Tilley, J. Polymer Sci., 18, 17 (1955).

27. J. Erickson, Private communication, 1964.

28. J. P. Plummer, Doctoral Thesis, University of Michigan (1964).

29. M. Born and K. Huang, Dynamical Theory of Crystal Lattices (Oxford, 1957).

30. S. Yip, R. Osborn and C. Kikuchi, Neutron Acoustodynamics (Phoenix Library, University of Michigan, 1962).

31. C. Y. Liang, S. Krimm and C. B. Sutherland, J. Chem. Phys. 25, 543 (1956).

32. G. C. Summerfield and J. D. Erickson, Bull, Am. Phys. Soc. Series 1, 9, 623 (1964).

33. T. Miyazawa and T. Kitagawa, J. Polymer Sci. Letters, 2, 395 (1964).